7-25-2017

Elucidating mechanisms of protein aggregation in Alzheimer's Disease using antibody-based strategies.

Benjamin A. Colvin
University of Missouri - St. Louis, bac4c3@umsl.edu

Elucidating mechanisms of protein aggregation in Alzheimer's Disease using antibody-based strategies.

A Dissertation

Submitted to the Faculty

of

University of Missouri – Saint Louis

by

Benjamin Alexander Colvin

In Partial Fulfillment of the

Requirements for the Degree

of

Doctor of Philosophy

in

CHEMISTRY

with an emphasis in Biochemistry

May 2017

University of Missouri – Saint Louis

Advisory Committee
Michael R. Nichols, PhD
Wesley Harris, PhD
James Bashkin, PhD
Keith Stine, PhD

Dedicated to the millions

who live with

Alzheimer's Disease.

ACKNOWLEDGEMENTS

My parents, Mr. Grant Colvin and Dr. Juanita Polito-Colvin. They encouraged my rampant inquisitiveness from an early age, and they were always there for me no matter what sort of trouble I got myself into.

The faculty at The Saint Louis Priory High School, especially the first great chemistry teacher I ever had, Mr. Gleich.

The QC group at GSK – Saint Louis, where I had my first real job as a scientist. From my experiences in the QC lab I developed an interest in chemical analysis which would ultimately lead to me returning to school for this degree.

Dr. Nichols has been a wonderful PI to study under. He has been a role model for me, especially his work ethic, determination and attention to detail – areas I know I still need to improve. My lab mates, current and former, especially Shana Terrill-Usery, for all the hours she spent training me and putting up with all my questions, and Elizabeth Hood, for *many* useful discussions. My committee, for their time and critical considerations.

The Graduate School, for the Dissertation Fellowship award. It's finally done!

TABLE OF CONTENTS

LIST OF TABLES

LIST OF FIGURES

LIST OF ABBREVIATIONS

(1X) PBS	Phosphate-buffered saline	ACH	Amyloid Cascade Hypothesis
ACSF	Artificial cerebro-spinal fluid	AD	Alzheimer's disease
AD P-tau	Hyperphosphorylated tau	AFM	Atomic force microscope
APOE	Apolipoprotein E	APP	Amyloid precursor protein
Aβ	Amyloid-β	Aβ40	Amyloid-β (1-40)
Aβ42	Amyloid-β (1-42)	BCA	Bicinchoninic acid
Bis-ANS	4,4'-dianilino-1,1'-binaphthyl-5,5'-disulfonic acid	BSA	Bovine serum albumin
CBD	Corticobasal degeneration	CD	Circular dichroism
DLB	Dementia with Lewy bodies	DMSO	Dimethyl sulfoxide
DNA	Deoxyribonucleic acid	DS	Down's syndrome
DSS	Disuccinimidyl suberate	DTT	Dithiothreitol
EDTA	Ethylenediaminetetraacetic acid	ELISA	Enzyme-linked immunosorbent assay
EM	Electron microscope	EOAD	Early-onset Alzheimer's disease
FAD	Familial Alzheimer's disease	FPLC	Fast performance liquid chromatography
FTDP-17	Chromosome 17-associated fronto-temporal dementia with Parkinsonism	GSK3	Glycogen synthase kinase 3β
GuHCl	Guanidinium hydrochloride	HD	Huntington's disease

HFIP	Hexafluoroisopropanol	HMW	High molecular weight
HrP	Horseradish peroxidase	IAPP	Islet amyloid polypeptide
LMW	Low molecular weight	MALS	Multi-angle light scattering
MAP	Microtubule-associated protein	MeOH	Methanol
MT	Microtubule	NFT	Neuro-fibrillary tangle
PAD	Phosphatase-activating domain	PD	Parkinson's disease
PHF	Paired helical filament	PiD	Pick's disease
PP1	Protein phosphatase 1	PSP	Progressive supranuclear palsy
SAD	Sporadic Alzheimer's disease	SDS-PAGE	Sodium dodecylsulfate polyacrylamide gel electrophoresis
SiRNA	Small interfering ribonucleic acid	TBS-T	Tris(hydroxymethyl) aminomethane-buffered saline with Tween 20
TEM	Transmission electron microscope	ThT	Thioflavin T
UV/Vis	Ultraviolet/visible	WR	Working reagent

*PBS or 1X PBS refer to phosphate-buffered saline. In the literature, the formulation this refers to is quite variable. In this manuscript, the PBS was prepared first as a 10X stock. The stock was 1.5 M (87.66 g/L) NaCl (MW 58.44 Da) and 100 mM (26.81 g/L) Na2HPO4 (MW 268.07) in water. When 1X PBS was desired, 100 mL of the 10X stock was mixed with 800 mL water, the pH was adjusted with dilute HCl and NaOH, and the volume was adjusted to 1000 mL with water.

ABSTRACT

This thesis was written by Colvin, Benjamin, A. in partial fulfillment of the requirements for a PhD. in Chemistry with an emphasis in Biochemistry, in December, 2017, at The University of Missouri – Saint Louis. The work described within was performed while under the mentorship of Michael R. Nichols, PhD. Historically, research in the Nichols Lab focuses on the fundamental biochemistry of Alzheimer's Disease (AD) and the involvement of amyloid protein aggregate pathology in neurodegeneration and dementia. Amyloid aggregates are protein polymers comprised of non-native-fold monomers with characteristic backbone-backbone cross-β-sheet secondary structures. The proteins known to undergo this pathological conformational change are collectively called amyloids, after the eponymous Amyloid- β protein, one of two amyloid proteins found in AD pathology, alongside the Tau protein.

One defining characteristic of Nichols Lab studies is thorough biophysical analysis. This is particularly difficult as amyloid protein aggregate solutions are inherently polydisperse, and highly sensitive to starting conditions. Sensitivity to starting conditions means that it is difficult to generate repeatable data; two aliquots taken from the same stock monomeric solution often have significantly different aggregate profiles after incubation. Polydispersity makes 3D structural determination by traditional methods such as X-ray crystallography difficult or impossible. Polydispersity also presents a challenge in deciphering pathology. Different aggregate isoforms are known to illicit different cellular responses. Therefore, in cellular and animal studies alike, purified,

well-characterized single isoform solutions often provide more meaningful results than bulk aggregate solutions.

As amyloid systems are refractory to many common research paradigms, the researcher must be clever and often apply uncommon methods to gain insight into their nature. The work herein takes this approach in studies of three different amyloid systems. First, oligomers are purified from bulk solution via SEC chromatography. In-line with this, MALS allows determination of absolute molecular weights for the isolated species. Then the isolated species are characterized via a number of methods, such as dye-binding assays, CD spectrophotometry, and conformation/isoform specific immunochemical assays.

I adapted the methods developed by the group of Rakez Kayed for generation of 2N4R tau oligomers from monomeric 2N4R tau via templating interaction with preformed oligomeric seeds. The method itself required modification due to the starting material, and significant preformed aggregates were present, which required additional steps to remove. I examined the extent of seeding when 2N3R is used as the monomeric pool, and analyzed the results with SEC-MALS and Western blot. Although the molecular weight profiles of the seeded and unseeded control were similar, I noted an elution volume shift in the seeded sample. This suggests a conformational change as a result of the seeding. Upon SDS-PAGE and Western blot analysis of the seeded and unseeded control with T22 antibody, which is specific for 2N4R oligomers, I detected no binding in either preparation. However, when the same preparations were probed with Tau-5 antibody, which recognizes both isoforms and has no conformational specificity, bands appeared corresponding to monomer, dimer/trimer and apparent tetramer in the

oligomer peak fractions of the seeded preparation, and to a lesser extent in the unseeded preparation. Taken together, the Western blot results suggest that the SDS-resistant 2N3R oligomer which was formed differs in conformation from the 2N4R oligomer used to generate the T22 antibody.

The second project described in this dissertation is a biophysical study of protofibril formation in two-isoform mixtures of Aβ42 and Aβ40 monomer. First, multiple incubation conditions were tested for generation of soluble HMW oligomers. Incubation at 37 ºC for 24 h in aCSF (pH 7.8) resulted in formation of insoluble fibril with very little soluble oligomer remaining. When the aggregation was performed in the same buffer at lower ionic strength under the same conditions (low-salt aCSF) the resulting solution was highly enriched with protofilaments. When Tris-HCl (pH 7.8) was used as the incubation buffer, the result was 91% fibril, with a 9% population of classic curvilinear protofibrils.

Selecting the low-salt aCSF method, 40 μM total Aβ monomer solutions were prepared which were all-Aβ42, all-Aβ40, or had Aβ42/Aβ40 ratios of 4:1, 1:1, or 1:4. Additionally all-Aβ42 monomer solutions were prepared at the same concentration Aβ42 as in the mixed solutions (32, 20, or 8 μM). After incubation, decreasing β-sheet content by ThT dye binding correlated with decreasing Aβ42 content, and the decrease was accentuated in the presence of Aβ40. Upon SEC purification, I noted a decreased protofibril % yield as Aβ40 concentration increases; in the all-Aβ42 preparations no trend was detected. There was no strong change in molecular weight between the all-Aβ42 preparations and the mixture preparations, as assessed by MALS in-line with SEC. I noted that protofibrils generated at lower Aβ42 concentrations had detectable α-helical

secondary structure as measured by CD, and this phenomenon was accentuated when Aβ40 was present.

Using a novel C-terminal selective ELISA, I probed the incorporation of each isoform into the protofibrils generated. The protofibrils were overwhelmingly Aβ42, suggesting very little Aβ40 is recruited during rapid protofibril formation. This held true even when the two isoforms were mixed at a 1:1 molar ratio.

Contrary to earlier results, when the Aβ42 concentration is held constant at 20 μM and only the Aβ40 concentration is varied, no trend is observed in protofibril % recovery. However, I did note a reduced protofibril β-sheet contribution when Aβ40 is present, and CD also revealed an increased α-helical characteristic.

The final project was characterization of a novel anti-serum, dubbed AbSL, generated against Aβ42 protofibrils. The tests demonstrated significant specificity for Aβ42 protofibrils over Aβ42 monomer or fibril, in both dot-blot and indirect ELISA formats. I also demonstrated AbSL indirect ELISA selectivity for Aβ42 protofibrils over Aβ40 protofibrils.

In order to probe the AbSL specificity epitope, a series of ELISA assays were performed with additional antibodies, Ab9 and Ab5, both N-terminal sequence-selective, and Ab2.1.3, which recognizes the C-terminal of Aβ42. The results indicated partial overlap between the AbSL conformational epitope and the N-terminal 16 amino acid sequence recognized by Ab9.

CHAPTER 1.

INTRODUCTION.

1.1 The cost of Alzheimer's disease dementia.

Alzheimer's disease (AD) is the most common form of dementia, and the sixth leading cause of death in the United States. One in three seniors dies with AD or another dementia. Not considering the emotional costs to the 5 million in this country living with the disease, and their families, AD and other dementias will cost the economy $236 billion this year (http://www.alz.org).

1.2 The classic Alzheimer's disease histopathology.

First described over a century ago (Alzheimer et al. 1995) AD is associated with two histopathological characteristics upon post-mortem examination of brain tissue: extracellular neuritic amyloid-β (Aβ) plaques (or senile plaques) and intracellular tau neurofibrillary tangles (NFTs) (Figure 1.1A) (Grundke-Iqbal et al. 1986, Selkoe 1991). Clinically, AD manifests as progressive dementia and neurodegeneration (Selkoe 2001). The plaques consist of deposits of Aβ peptide, aggregated to form the characteristic insoluble fibril structures. Diseases which involve Aβ aggregates such as these characteristic senile plaques found in Alzheimer's are referred to as amyloidoses. The term amyloid is a bit of a misnomer- from the greek root *amulon,* which means starch.

The amyloid quaternary structure, as a class, was defined >150 years previous by the Pathologist Virchow, relating his early observation of starch-like blue staining of the material when treated with iodine solution (Titford 2010). The modern gold-standard staining test for amyloid is Congo Red, which displays characteristic 'apple green' birefringence in cross-polarized light (Figure 1.1B) (Jin et al. 2003). NFTs are composed of paired helical filaments of aggregated tau protein, which is also considered an Amyloid protein. Current thinking suggests AD is a multiple-amyloid disorder, not only in terms of histopathology, of etiopathogenesis as well– that is, both Aβ and tau contribute to pathology in AD.

Figure 1.1 The quintessential Alzheimer's Disease histology.

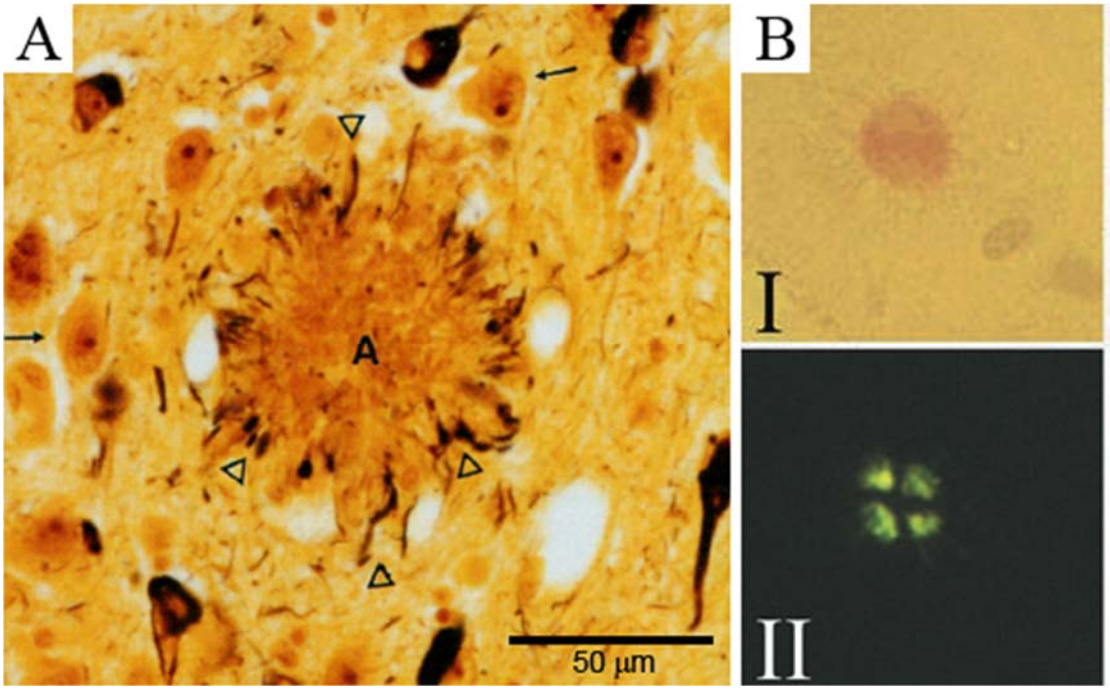

(A) In vivo there are characteristic histopathological hallmarks associated with AD. Silver stain (modified Bielschowsky) of a 6 µm paraffin embedded section of amygdala from an AD patient post-mortem. Dark staining areas are NFT. Senile plaque in the center noted with letter A. Indicated with △, Surrounding the plaque are "dystrophic" or structurally abnormal neurites. Normal neurons indicated with ↑ are present further from the inclusion. (B) Congo Red stain of a paraffin embedded 10 µm section from the midtemporal gyrus of an AD patient post-mortem. (I) Section stain under linearly polarized white light. (II) Section stain placed between crossed polarizers, revealing characteristic "apple green" birefringence. Panel A is from Selkoe 1991, and panel B is from Jin et al 2003.

1.3 Amyloid aggregation.

The amyloid aggregate state, inherently a consequence of interactions between protein backbones (cross β-sheet), has high thermodynamic stability and resistance. Theoretical and experimental evidence support the concept that proteins may form amyloid aggregates under conditions where they are partially or completely unfolded, and that the amyloid state is an alternative low energy state to a protein's native fold, common all protein (Arosio et al. 2015).

Amyloid aggregation is similar to the well-studied crystal growth and polymer gelation processes, possessing a pseudocrystalline growth pattern (Dobson 1999). A monomer solution will exist for some time, the lag phase, until nucleation occurs, initiating the elongation phase, which continues until the solution is sufficiently depleted of monomer. An aggregating solution of amyloid is polydisperse, containing monomers, insoluble fibrils (in suspension and deposited) and a range of oligomeric species. Low molecular weight (LMW) oligomer includes dimer, trimer, tetramer, up to dodecamer. HMW oligomer group certainly includes species such as large globular oligomers, protofibrils, protofilaments; these species are made up of dozens, if not hundreds, of monomers.

1.4 Genetic evidence for the involvement of Amyloid-β in AD pathology.

AD manifests clinically as progressive dementia and pathologically as neurodegeneration. There are two broad classes of the disease, based on the extent to which genetic predispositions are identified, and the age of disease on-set. Sporadic

(SAD), or late-onset AD is the most common form of the disease, and occurs after 60 years of age. There is no specific genetic link, although there are some risk factors which have been identified. The greatest known risk factor is the E4 allele of the gene which encodes the apolipoprotein APOE. Individuals who express the ApoE4 isoform have an increased risk for late-onset AD. Familial AD (FAD), also called early-onset AD (EOAD), is quite rare, and occurs due to multiple different mutations, usually identified do to the prevalence of the disorder within a small population of people. AD with onset between 30 and 60 years of age is characterized as EOAD (Selkoe 2001, Zlokovic 2013).

Genetic studies of EOAD cases strongly implicate the Aβ peptide as a primary effector of AD pathology (Hardy 1997). Aβ peptide is a product of sequential proteolytic cleavage of the amyloid precursor protein (APP), a 770 amino acid single-pass transmembrane protein (Kang et al. 1987), with a relatively short 30 minute half-life (Weidemann et al. 1989). APP is translocated to the cell membrane where it is oriented with its N-terminal domain extracellular, and C-terminal cytoplasmic. At this point, APP is proteolytically cleaved differentially along one of two pathways: the α-pathway or the β-pathway (Selkoe 2001, O'Brien et al. 2011). The α-pathway (or non-amyloidogenic pathway) is not associated with AD. This pathway involves sequential cleavage first by α-secretase in the extracellular region, then by γ-secretase, within the cell membrane. α-secretase cleaves within the Aβ peptide region of the APP protein, yielding the non-amyloidogenic p3 fragment (Hardy 1997, Selkoe 2001). In the amyloidogenic cleavage sequence, APP is first cleaved by β-secretase to form a membrane-associated 99 amino acid segment. Then imprecise cleavage by γ-secretase produces multiple isoforms of the Aβ peptide between 38 and 43 residues long (Selkoe 2001). The two most predominant

isoforms of Aβ are Aβ(1-40) (Aβ40) and Aβ(1-42) (Aβ42). Aβ40 is more abundant in CSF, however Aβ42 is more hydrophobic and more prone to aggregation than the 40 amino acid peptide and makes up the core of the plaques (Figure 1.2) (Axelsen et al. 2011).

All described genotypes leading to EOAD involve APP. Either the APP gene itself is affected, or APP processing via altered secretase function. The most straight-forward example is Down's syndrome (DS), or trisomy of chromosome 21 (trisomy-21). Individuals with DS possess an extra copy of chromosome 21, and the APP gene lies on this chromosome. This leads to the over-expression of APP (Rumble et al. 1989). By their 40th year, individuals with full trisomy-21 invariably develop AD neuropathology (Aβ plaques and tau tangles) sufficient for a histopathological diagnosis of AD (Wisniewski et al. 1985, Head et al. 2012), and suffer a drastically increased rate of AD-related clinical dementia (Head et al. 2012).

There are more than 20 APP mutations which have been identified in cases of EOAD. These mutations tend to do one of two things: either they enhance overall production of Aβ by causing a preference for the β-pathway of APP proteolysis, or they alter the γ-secretase cleavage site, leading to more Aβ42 production, over Aβ40 (Hardy 1997, Selkoe 2001). The final group of EOAD-associated mutations occur in one of the two presenilin genes, and alter the γ-secretase complex, again increasing Aβ42 production, over Aβ40.

Figure 1.2 Pathways of APP processing.

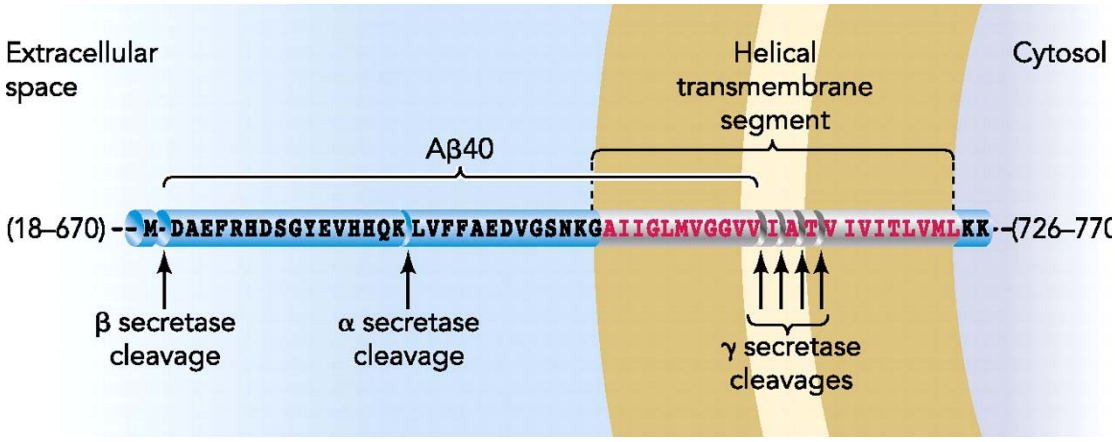

This cartoon represents the amyloidogenic pathway of APP processing. APP undergoes one of two pathways of proteolytic cleavage. One results in generation of the Aβ peptide, while the other does not. If APP is sequentially cleaved by α-secretase and γ-secretase, the non-amyloid p3 fragment does not readily undergo amyloid aggregation. However, if APP is cleaved first by β-secretase followed by γ-secretase, then an Aβ peptide isoform is the result. The figure is from Axelsen et al. 2011.

1.5 The Amyloid Cascade Hypothesis.

That the histopathological and genetic evidence both indicated the involvement of APP and its cleavage product Aβ in AD pathogenesis, and particularly the prevalence of histopathology and ageing-related dementia in cases of trisomy-21 (Selkoe 1991, Masters et al. 2012), was critical in the formation of early AD etiological theory (Hardy et al. 1992). Early in the 1990s, a number of articles presented similar viewpoints (Hardy et al. 1992), (Selkoe 1991), (Hardy et al. 1991), (Beyreuther et al. 1991) on the predominant role of Aβ in AD pathology. What came to be called the Amyloid Cascade Hypothesis (ACH) posited that Aβ deposition in plaques is the cause of all AD pathology, with NFT, vascular and neuronal damage, and clinical dementia resulting from this event (Hardy et al. 1992).

In the 25 years since it was first presented, the ACH has had significant challenges, multiple alternative hypotheses have been presented, and the ACH has been refined and expanded. 25 years of research has greatly expanded the AD literature, and current thinking is quite a bit more nuanced. The modern ACH (Figure 1.3) presents a view of AD pathology where tau protein and Aβ peptide can both mediate pathology, and interplay between the two ultimately leads to disease. Additionally, the role of pathologic oligomeric Aβ and tau has come to the fore. Furthermore, in light of the sustained neuroinflammatory response in AD, the role of glial-cell derived indirect neuropathology must also be considered (Karran et al. 2016).

Figure 1.3 A modern Amyloid Cascade Hypothesis.

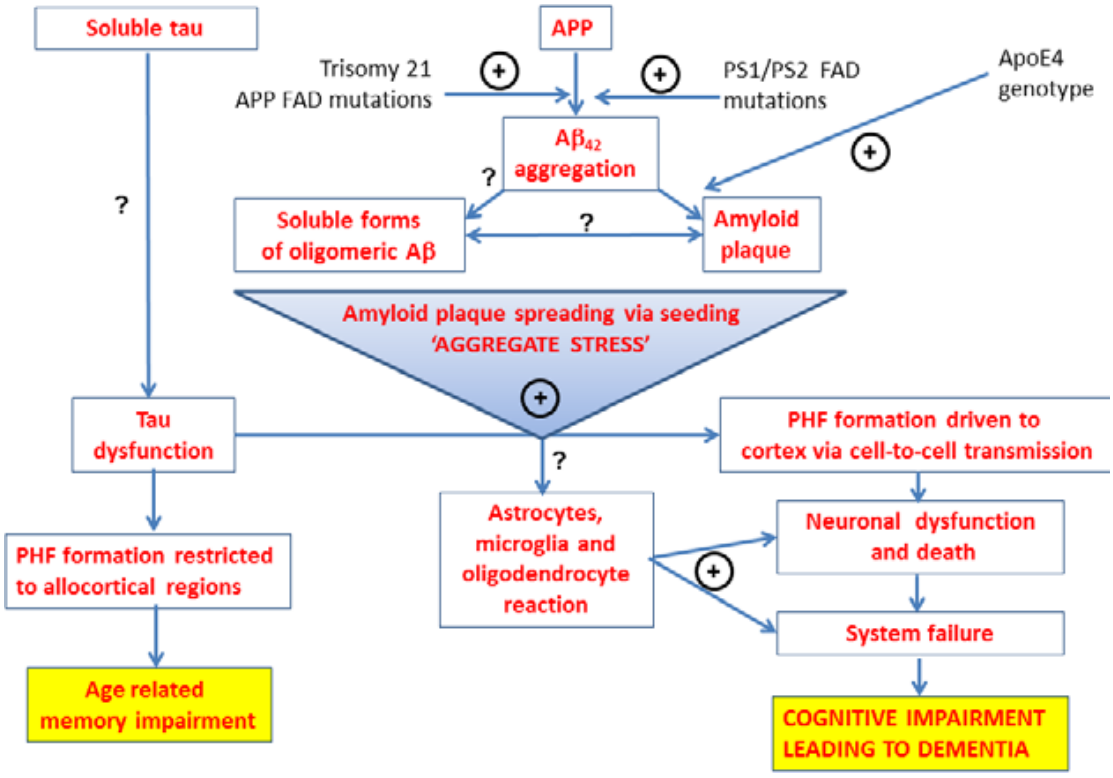

This diagram is an example of a modern recasting of the Amyloid Cascade Hypothesis. Aggregation of Aβ remains a primary event in pathology. In some cases, Aβ directly induces pathology, such as the neuroinflammatory response. In others, Aβ acts indirectly, inducing Tau mediated pathology. And in a third axis, Tau dysfunction may lead to pathology independent of Aβ. The figure is from Karran and De Strooper 2016.

1.6 Modeling AD progression.

The shift in perspectives is also reflected at the clinical level, in biomarker-based modeling of AD progression. Biomarkers are signs of pathology which can be measured *in vivo* in a human patient, and there is much interest in correlating changes in these signs with changes in disease symptoms and severity. One of the most widely known and accepted models of AD biomarker change and clinical progression was put forth by Dr. Clifford Jack and colleagues (Jack et al. 2013). The model is shown in Figure 1.4. There are multiple major AD biomarkers, and can be divided into two categories: measures of Aβ deposition, and measures of neurodegeneration. Aβ deposition is monitored by assay of the cerebro-spinal fluid (CSF) Aβ42, as well as amyloid imaging by positron emission tomography (PET). Neurodegeneration is monitored by CSF total tau and phosphorylated tau, hypometabolism via fluoroxyglucose PET, and brain atrophy via structural MRI. The most advanced model also incorporates histological findings, which would be below detection via biomarker assays. The model posits that tau, not Aβ, abnormalities arise first, then Aβ abnormalities act to accelerate the rate of tau pathology, and the two work in concert to bring about the neurodegeneration and increasing mental impairment associated with later stages in AD progression. This positions tau a1s a major player alongside Aβ in the biological mechanisms which underlie AD.

Figure 1.4 Integrated model of AD progression.

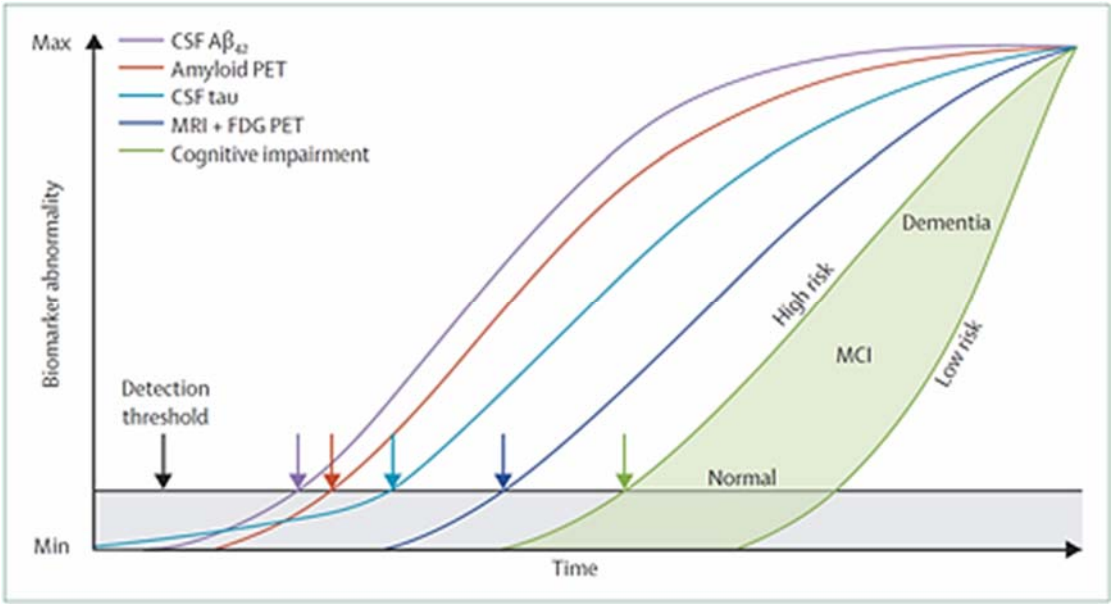

Below the detection threshold, biomarkers cannot detect pathological changes, however this model incorporates histological findings suggesting tauopathy precedes Aβ pathology. However, once Aβ pathology reaches a certain level, it begins to accelerate the rate of tauopathy increase. Once this process occurs, measures of cognitive impairment begin to increase. The figure is from Jack et al 2013.

1.7 Non-Aβ amyloid diseases.

In contrast to Aβ, the microtubule associated protein (MAP) tau is not linked with any EOAD genotypes. However, aggregated tau deposits have been identified in other non-Aβ neurodegenerative disorders, for example, Parkinson's disease (PD) (Galpern et al. 2006), dementia with Lewy bodies (DLB) (Galpern et al. 2006), frontotemporal dementia and parkinsonism linked to chromosome 17 (FTDP-17) (Buee et al. 1999), Pick's disease (PiD) (Feany et al. 1996, Buee et al. 1999, Zhukareva et al. 2002), progressive supranuclear palsy (PSP) (Feany et al. 1996, Buee et al. 1999), corticobasal degeneration (CBD) (Feany et al. 1996, Buee et al. 1999), and recently Huntington's disease (HD) (Fernandez-Nogales et al. 2014). PD and DLB belong to the synucleinopathy group of diseases. They both involve aggregates of α-synuclein, another amyloid protein, as well as tau (Galpern et al. 2006). FTDP-17, PiD, PSP and CBD are tauopathies, containing tau aggregates, and no other detected amyloid pathologies. FTDP-17 is of particular interest, as it is a strictly familial disorder; families with FTDP-17 have mutations in the gene which encodes tau protein (Buee et al. 1999).

1.8 Tau, a microtubule-associated protein.

Microtubules are one of the three structural systems, along with actin and intermediate filaments, which compose the eukaryotic cytoskeleton. Among other functions, dynamic networks of microtubules are essential for cell shape and intracellular trafficking. α-tubulin and β-tubulin (each ~50 kDa, with ~50% sequence identity) form heterodimeric subunits which polymerize non-covalently to form MTs (Weisenberg et al.

1968, Burns 1991, Desai et al. 1997). Microtubules are inherently polar with regards to polymerization rates, having a fast growing "plus" end and a slower growing "minus" end. αβ-subunits orient longitudinally to form protofilaments, and these are associated laterally to form a 25 nm diameter hollow cylinder (Desai et al. 1997).

The primary locations tau is expressed are the central and peripheral nervous system. It is also found in other tissues, to a lesser extent (Gu et al. 1996). In a healthy nervous system, tau is most often found associated with axons, but it is also detected in dendrocytes (Morris et al. 2011). Tau is a MAP involved in assembling and stabilizing microtubules in neuronal cells (Weingarten et al. 1975, Buee et al. 1999, Buee et al. 2000). In humans, there are 6 well-studied isoforms of the tau protein, generated by alternative splicing of mRNA transcripts of the MAPT gene located on chromosome 17 (Figure 1.4). The alternative splicing involves exons 2, 3, and 10. There is also alternative splicing of exons 6 (Wang et al. 2007), 4a, and 8, but these isoforms are not yet well-studied (Morris et al. 2011), and only expressed in peripheral tissue (Wang et al. 2016). Exons 2 and 3 code 29 (N1) and 58 (N2) residue N-terminal inserts, respectively. Exon 10 codes R2, a 31 amino-acid insert, the second in a series of four (R1-R4) microtubule-binding domain repeats (R1-R4), with R4 being the most C-terminal domain. Translation of alternatively spliced mRNA results in tau isoforms between 352 and 441 amino-acids in length, with no N-terminal inserts (0N), the 29 amino-acid N1 insert (1N), both N-terminal inserts (2N), and either three (3R) or four (4R) microtubule binding repeats (Goedert et al. 1989, Lee et al. 1989, Billingsley et al. 1997, Buee et al. 1999).

The tau protein can be divided into 3 regions: the N-terminal portion, the proline-rich portion, the microtubule-binding repeats (MTBRs) region (Kolarova et al. 2012).

The N-terminal comprises ~120 amino acids in the largest (2N) isoforms. This region is also referred to as the projection domain, as is projects from the surface of the microtubule into the cytoplasm. It may interact with the plasma membrane, or other cytoskeletal elements such as actin (Kolarova et al. 2012). The extreme N-terminal region, amino acids 2-18, comprise the recently discovered phosphatase-activating domain (PAD), which is important for early events in tau pathology (Kanaan et al. 2011). The next region is the proline-rich region, which contains seven PXXP motifs. These serve as binding sites for signaling proteins, such as the tyrosine kinase FYN, which contain SH3 domains (SRC family non-receptor tyrosine kinases) (Lee et al. 1998). The MTBR region contains the 3 (3R) to 4 (4R) repeat segments responsible for interaction with microtubules (Buee et al. 1999).

Figure 1.5 The tau protein

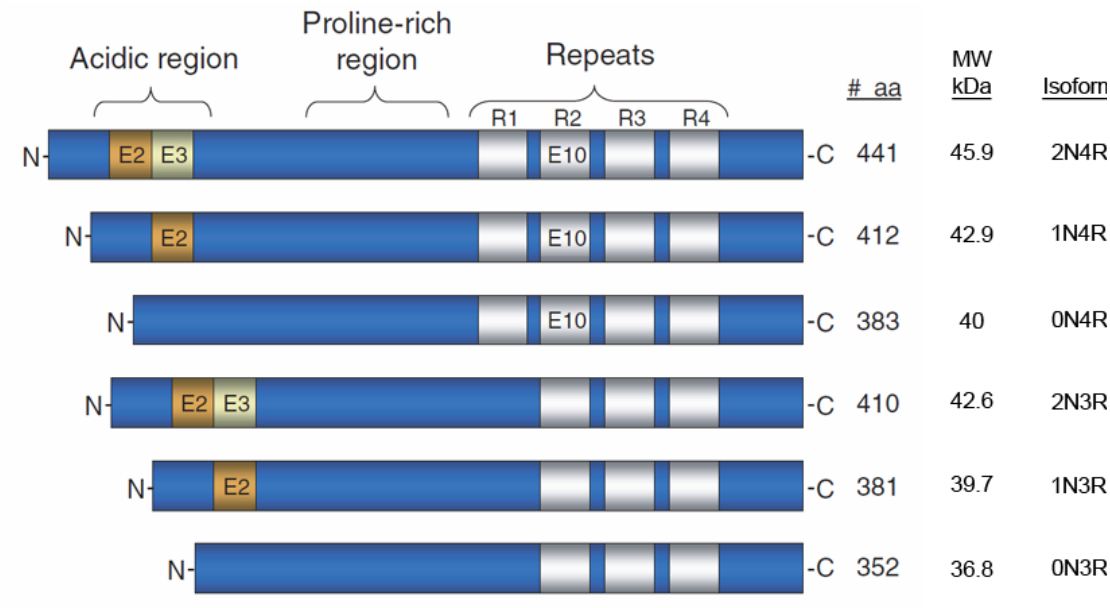

The MAPT gene codes for the 6 canonical splice variants of the Tau protein. The isoforms are distinguished by the presence of 0, 1, or 2 N-terminal repeats, coded by exons 2 and 3, and 3 or 4 microtubule binding repeat regions. Exon 10 codes for repeat region R2, which is present in the 4R isoforms and absent in the 3R. This dissertation is primarily concerned with the 2N3R and 2N4R isoforms, the most common found in adult human brain. The splice pattern coding convention will be used, which labels the isoforms by their number of N and R regions, providing more meaningful names. This differs from the NCBI ID numbering system, as well as the Uniprot system, which ascribes each isoform a letter. The figure is from Johnson and Stoothoff 2004.

1.9 Tau phosphorylation.

The longest tau isoform contains 79 potential Ser or Thr, and five Tyr phosphorylation sites, of which approximately 30 are phosphorylated under non-pathological conditions. In contrast to Aβ, whose native non-pathological function remains unclear, tau pathology involves loss-of-function effects, as well as putative gain-of-function toxic effects (Morris et al. 2011). It has long been known that tau is sufficient to promote microtubule (MT) nucleation and elongation *in vitro* (Weingarten et al. 1975), and this was the first function assigned to the tau protein. Microtubules are dynamically unstable, which means polymerization and depolymerization coexist at the ends of the microtubules, and the growth or shrinking of the microtubule is dependent on their relative rates. MAPs such as tau can associate with and control the dynamics of microtubules (Hirokawa et al. 2005). Tau associates directly with microtubules, enhancing polymerization, and reducing depolymerization *in vitro* (Drubin et al. 1986). The binding of tau to microtubules is controlled by the phosphorylation state of tau. Dephosphorylation of tau increases binding of tau to microtubules, and indeed increases microtubule polymerization (Lindwall et al. 1984). Normal neurons have approximately 10:1 tubulin to tau ratio; neuronal tau concentration is ~2 μM, and most tau is found associated with MTs (Butner et al. 1991, Khatoon et al. 1992).

Hyperphosphorylated tau (AD P-tau) the main component of the NFTs found in AD (Braak et al. 1991, Buee et al. 2000). AD P-tau has a much higher amount of phosphorylation. Compared to normal tau, which contains 2-3 mols phosphate per mol

tau, AD P-tau has mol ratio of 5-9 mol phosphate per mol tau (Kopke et al. 1993). Not only does AD P-tau have reduced MT binding capability, when AD P-tau is added to a mixture of normal tau and tubulin, MT assembly is inhibited. This suggests both a loss-of-function and a gain-of-function effect, in that AD P-tau cannot bind MT, yet gains the ability to interact with normal tau and prevent its microtubule-promoting activity (Alonso et al. 1994).

As alluded to above, mounting evidence suggests that native tau likely functions as more than just a MT stabilizing protein (Morris et al. 2011). In cell culture and *in vivo* in mouse hippocampus, tau co-localizes with the most unstable and highest turnover MTs (Kempf et al. 1996, Fanara et al. 2010), and siRNA knockdown of tau in primary culture is neither lethal nor does it modify MT number or polymerization (King et al. 2006, Qiang et al. 2006). This suggests that *in vivo* tau may not function primarily as a MT stabilizer. Furthermore, numerous binding partners have been identified for tau in the intervening years since the initial studies with tau and MT, and tau may have multiple functions, such as modulation of axonal transport, as well as cell signaling (Morris et al. 2011).

As I have hopefully demonstrated, both Aβ and tau are implicated in the etiopathogenesis of AD. These amyloid proteins have complex biochemistries. Unraveling the intricacies of their behaviors, both the morphological and kinetic aspects of their aggregation pathways, and how those aggregates can induce neuropathological changes, will be essential in building a full picture of AD at the cellular level, which will inform future therapeutic development endeavors. In the remaining chapters of this dissertation, I will first describe the methods used in the novel research presented in the

following results chapter. Each results chapter will be prefaced by an introduction which will describe the problem the research is targeting, as well as a summary of current knowledge and questions which makes the research important.

CHAPTER 2.

METHODS.

2.1 Preparation of tau oligomers.

The general protocol for preparing tau oligomers via seeding is described here. Some modifications were made, and those are described in the text as appropriate. Figure 3.2 provides a summary of the tau oligomer preparation. An aliquot pellet of purified recombinant tau, generated as described in (Margittai and Langen 2004) was dissolved in 30 µL 8 M Urea, freshly prepared. The sample was then diluted to 1 mL with 1X PBS (pH 7.4), vortexed briefly (3 s, medium speed), transferred to a 10 kDa molecular weight cut-off 3 mL Slide-a-lyzer dialysis cassette (Thermo Scientific), and dialyzed overnight at 4 ºC against 1X PBS (pH 7.4). After dialysis, the sample (~1 mL) was transferred to a new Eppendorf tube, and concentration was determined by BCA assay, and absorbance at 280 nm. The sample was then diluted to 1 mg/mL. Aliquots of the solution were stored at -20 ºC until use.

For oligomerization reaction experiments, 300 µL tau stock was diluted to 0.3 mg/mL with 1X PBS (pH 7.4), yielding a total volume of 1 mL. At this point, there was an optional step, which involved incubation of the aliquot at room temperature for 24-48 h with stirring. This was reported to improve reproducibility. Then, to initiate seeded

oligomerization, 7 µL of 0.3 mg/mL oligomer seed solution was added, and the solution mixed for 1 min by gentle pipetting. The mixture was incubated at 25 ºC with gentle shaking on an orbital shaker for 1 h to allow formation of oligomers.

2.2 Microplate BCA protein concentration assay.

The bicinchoninic acid (BCA) assay measures reduction of Cu^{2+} by the peptide bond between amino acid residues. The reduced Cu^{1+} product is chelated by two BCA molecules. The adduct appears violet in solution and absorbs in the green with an aborbance maximum of 562 nm. To measure tau sample protein content, a bovine serum albumin (BSA) standard curve was created, using stock BSA standard (Thermo Scientific) with a concentration of 2 mg/mL as the upper limit. BSA standard was serially diluted with 1X PBS (pH 7.4) to create standards with concentrations of 1500, 750, 375, 150, 75, and 15 µg/mL. The 0 mg/mL blank was 1X PBS (pH 7.4) alone. Samples and standards were added into wells of a 96-well-plate in the desired number of replicates. BCA working reageant (WR) was prepared by mixing BCA reagent A (Thermo Scientific) and BCA reagent B (Thermo Scientific) in a 50:1 ratio. 100 µL WR was added to each assay well. An adhesive plastic cover was placed on the plate, which was incubated at 37 ºC for 30 min in a water bath. The plate rested on a support submerged in the waterbath, and care was taken to ensure the water level of the bath was below the top of the assay plate. After incubation, the plate was allowed to cool for 30 min on the benchtop. Then absorbance measurements were performed at 562 nm in a SpectraMax 340 absorbance plate reader (Molecular Devices, Union City, CA). Readings were averaged and blank corrected for mean absorbance in the 1X PBS blank wells. A linear

regression curve was derived from the BSA standard absorbances, which was used to estimate protein content in the tau samples. In cases were the sample absorbances were below the standard curve range, the assay was repeated with a larger sample volume, and a dilution factor applied in the calculations.

2.3 Protein determination by 280 nm absorbance.

Absorbance readings were performed in a quartz cuvette with a pathlength of 1 cm. Spectra of samples in 1X PBS (pH 7.4) were recorded from 200 to 400 nm. A background spectrum was also recorded from 1X PBS. Baseline was subtracted, and the sample absorbances observed at 280 nm. Beer's Law,

$$\frac{A_{280}}{\varepsilon_{280} \times l} = c \tag{1}$$

was used to calculate concentrations from absorbance, pathlength and calculated molar absorptivities of 7500 M^{-1} cm^{-1} and 7375 M^{-1} cm^{-1} for 2N4R and 2N3R tau, respectively.

2.4 Aβ preparation.

2.4.1 Processing and aliquoting.

Synthetic, lyophilized Aβ (W. M. Keck Biotechnology Resource Laboratory, Yale School of Medicine, New Haven, CT) was received and stored at -20 ºC until use. Processing of the lyophilate began with dissolution in 100% hexafluoroisopropanol (HFIP) purchased from Sigma-Aldrich, Saint Louis, MO). HFIP is a fluorinated solvent commonly used to prevent aggregation, as it forces proteins into an α-helical conformation. The resulting 1 mM Aβ solution was divided into 1 mg (dry weight)

aliquots in sterile microcentrifuge tubes. The aliquots were placed in the fume hood uncovered at room temperature to allow overnight evaporation of the HFIP. The aliquots were then vacuum-centrifuged to complete the removal of any remaining residual HFIP. The result was a thin "peptide film" coating the bottom and lower portion of the tubes. The HFIP-processed aliquots were then stored at -20 ºC, over desiccant, until use.

2.4.2 Preparation of Aβ42/40 mixtures.

HFIP-processed aliquots of Aβ42 and Aβ40 were resuspended in 100% HFIP to concentrations of 1 mM, and allowed to incubate sealed for 1 h to ensure thorough dissolution. Amounts were combined which would yield the desired Aβ42/Aβ40 dry peptide ratios with total a Aβ concentration of 200 μM. For the 4:1 Aβ42/Aβ40 ratio, 160 μL 1 mM Aβ42 (0.72 mg) was combined with 40 μL 1 mM Aβ40 (0.17 mg). For the 1:1 Aβ42/Aβ40 ratio, 100 μL 1 mM Aβ42 (0.45 mg) was combined with 100 μL 1 mM Aβ40 (0.43 mg). For the 1:4 Aβ42/Aβ40 ratio, 40 μL 1 mM Aβ42 (0.18 mg) was combined with 160 μL 1 mM Aβ40 (0.69 mg). The mixed solutions were prepared in microcentrifuge tubes, and placed in the fume hood uncovered to allow evaporation of solvent overnight. The next day, the ratio mixtures were vacuum centrifuged to remove residual HFIP. The resulting HFIP-processed ratio preparations were stored over desiccant at -20 ºC until use.

For monitoring of aggregation in the SEC purified monomer fractions derived from these mixtures, mixed monomer fractions were diluted with aCSF to a total Aβ concentration of 40 μM, and supplemented with 0.05% sodium azide (NaN_3), a preservative commonly used in extended incubations to inhibit bacterial growth. The

mixtures were incubated at room temperature for multiple weeks, and provided material for numerous measurements over the course of the incubation.

2.4.3 Preparation of Aβ protofibrils.

Protofibrils were prepared as described previously (Paranjape et al. 2013). An HFIP-processed aliquot was dissolved in 50 mM NaOH, which yielded a 2.5 mM Aβ solution. NaOH is used to ensure the pH of the solution does not approach the isoelectric point of Aβ (calculated pI = 5.3), which would promote undesirable formation of aggregates (Teplow 2006). For spontaneous formation of protofibrils, the solution was then diluted with artificial cerebrospinal fluid (aCSF) to 250 μM Aβ. aCSF is a carbonate-phosphate buffer system designed by the Nichols lab, suitable for biophysical as well as cell culture work with Aβ (Paranjape et al. 2013). The aCSF consisted of 15 mM $NaHCO_3$, 1 mM Na_2HPO_4, 130 mM NaCl, and 3 mM KCl, adjusted to pH = 7.8 with HCl, and filtered (0.22 μm) through a bottle-top vaccum filter. For convenience, this buffer was often prepared as a pH-adjusted 10X stock. When needed the stock was diluted to the working concentration, and then final pH adjustment was performed, followed by filtration, before use. Immediately before analysis, the PF solution was centrifuged for 10 min at 18,000 x g to ensure no insoluble aggregates were present. Protofibrils were then purified by SEC.

2.4.4 Preparation of Aβ42 oligomers.

A slightly modified version of the method developed at the LaDu Lab (Stine et al. 2003) was used to prepare Aβ42 oligomers. HFIP-processed Aβ was dissolved in sufficient 100% dimethyl sulfoxide (DMSO) to yield a 5 mM solution of Aβ. DMSO is

another solvent commonly used in the field. It prevents aggregation at high concentrations, however at lower concentrations promotes it. The DMSO solution was then diluted to 100 μM in cold aCSF (pH 7.8). The buffered solution was then incubated at 4 ºC for 24 h. Immediately before analysis, the oligomer solution was centrifuged for 10 min at 18,000 x g to ensure no insoluble aggregates were present. Oligomer was then purified by SEC.

2.4.5 Preparation of purified Aβ42 monomers.

When higher concentration solutions of pure monomer were desired, HFIP-processed peptide was dissolved in a solution of 6 M guanidine hydrochloride (GuHCl) and 10 mM NH_4OH. Then centrifuged for 10 min at 18,000 x g, and purified via SEC as described below in section 2.5.

2.4.6 SEC-purified monomer Aβ42/40 aggregation reactions.

Aβ42 and Aβ40 fractions, freshly purified separately as described above, were combined at the desired amounts and diluted with aCSF to 40 μM total Aβ composed of the desired ratios of Aβ42 and Aβ40. Preparations were incubated at 37 ºC for 24 h without agitation. The preparations were then centrifuged for 10 min at 18,000 x g, and fractionated via SEC as described above.

2.5 Size-exclusion chromatography (SEC).

After final centrifugation, proteins prepared for fractionation via SEC were injected onto a Superdex 75 HR 10/30 (GE Healthcare) attached to an AKTA FPLC system (GE Healthcare). The column had been coated previously with 2 mg bovine serum albumin (BSA) in the selected running buffer, prepared from a 7.5% solution of

BSA fraction V (Sigma) to limit non-specific binding of the sample to the column matrix. Elution was performed at room temperature with a flow rate of 0.5 mL/min in the selected running buffer. When further analysis was to be performed after SEC separation, 0.5 mL fractions were collected and placed immediately on ice. Determinations of concentration were performed in-line by UV absorbance at 280 nm. The extinction coefficient used for Aβ was 1450 cm^{-1} M^{-1}. For 2N4R tau it was 7500 cm^{-1} M^{-1}, and for 2N3R it was 7375 cm^{-1} M^{-1}. When MALS determination of molecular weight was desired, the MALS instrument was connected in-line between the UV detector and the fraction collector.

2.6 Multi-angle light scattering (MALS).

Measurements were performed at room temperature and in-line with SEC, flow of 0.5 mL/min. Astra 4.90.08 (Wyatt Technology) software received data at the factory-set transmission rate from fixed angle detectors 4-16 at the read head of the DAWN DSP (Wyatt Technology). The instrument takes a K12 quartz flow cell and vertically polarized helium-neon laser. The Debye formalism of the Rayleigh-Debye-Gans approximation for large anisotropic particles was used to plot the data (Wyatt 1993, Ogendal 2013):

$$\frac{R_\theta}{Kc} = M_W P(\theta) \tag{2}$$

Here, the scattering intensity, or Rayleigh ratio (R_θ) is defined in terms of the molecular weight (M_W) of the scatterer and form factor $P(\theta)$. K is an optical constant:

$$K = 4\pi^2 \left(\frac{dn}{dc}\right)^2 n_0^2 \lambda_0^{-4} N_A^{-1} \tag{3}$$

Where *dn/dc* is the change in the refractive index of the solution, *n*, with change in solute concentration, *c*, with units: g/mL. The refractive index of the pure solvent is n_0, λ_0 is the wavelength of the incident light in a vacuum (632.8 nm for the laser), and N_A *is Avogadro's number*.

The form factor, $P(\theta)$,

$$P(\theta) = 1 - \left(\frac{16\pi^2}{3\lambda^2}\right) R_g^2 \sin^2\left(\frac{\theta}{2}\right) \quad (4)$$

relates to the size and shape of the light scattering particles, and accounts for scattering intensity changes with respect to scattering angle θ as a result of destructive interference of the scattered light across the surface of an anisotropic (non-spherical) scatterer. As θ goes to zero, $P(\theta)$ goes to 1. The form factor depends on the radius of gyration, R_g, which encodes the particle's shape. If equation 3 is substituted into equation 1 the result

$$\frac{R_\theta}{Kc} = M_W - M_W \left(\frac{16\pi^2}{3\lambda^2}\right) R_g^2 \sin^2\left(\frac{\theta}{2}\right) \quad (5)$$

is a linear equation with R_θ/Kc as a function of $\sin^2(\theta/2)$. Plotting the results for various detector angles θ yields a line with slope R_g, and y-intercept equal to M_W.

I regularly performed normalization of the MALS detector array using high-purity BSA monomer. A small enough molecule (generally 10 nm is considered the limit) such as BSA monomer has a light scattering form factor P(θ) = 1, and light scattering becomes angle independent; it is an isotropic scatterer. This is important for the normalization process. The signal received at each detector is measured, and correction factors are calculated to adjust for detector-detector differences. When determining the molecular

weight of an unknown, the correction factors are applied to the detected signal, to generate a Rayleigh ratio for each detector, which is required for calculation of molecular weight.

2.7 Care and maintenance of MALS instrumentation

The MALS detector normalization process should be performed regularly, since the condition of the flow cell will change with time, even when the most fastidious care and maintenance schedules are observed, such as storage in pure organic solvent, and frequent cleaning. Even with frequent flow-through of cleaning solutions such as dilute nitric acid, or detergents specifically designed for removal of protein from quartz optics, microscopic bubbles or even resistant deposits can arise which alter the scattering of light among the detectors. Detectors should *always* be normalized after the cell is removed for the most thorough available cleaning procedures. Though removing and cleaning the flow cell by hand is delicate, time consuming work, it occasionally becomes necessary. Even if the cell is removed and cleaned before each measurement (a risky proposition, as it contains multiple small, high-precision, i.e. expensive, components), there remains the possibility that slight changes in alignment of the cell with the incident light beam will alter scattering. Finally, changes in the sample buffer system should also always be accompanied by a new normalization, as different buffers will change the light scattering pattern as well. One recommendation arising from this project was regular normalization checks with an additional molecular weight standard. Such practices can also be informative when dealing with unknown, complex sample systems such as amyloid aggregates.

2.8 Dynamic light scattering.

Dynamic light scattering was used to determine hydrodynamic radii (R_H). A DynaPro Titan instrument (Wyatt Technology) was used. Measurements were taken at room temperature in a quartz cuvette. Data was collected at a 90º angle to the incident light, with a 5 s averaging time. Autocorrelated light intensity data (>25 acquisitions per sample) were used to calculate particle diffusion and converted to R_H with the Stokes-Einstein equation.

2.9 Thioflavin T (ThT) fluorescence.

Assessment of ThT binding by Aβ samples was performed as described in Nichols, *et al*. (Nichols et al. 2002). Aβ was diluted with aCSF (pH 7.8) containing ThT such that both Aβ and ThT arrived at a final concentration of 5 μM. Samples were transferred to a fluorescence cuvette, and measurements were made on a Cary Eclipse fluorescence spectrophotometer. The excitation wavelength was 450 nm. Fluorescence emission was scanned from 460 nm to 520 nm, and the intensity readings were integrated from 470 nm to 500 nm, and corrected against a buffer baseline.

2.10 Electron microscopy.

10 μL of SEC-purified Aβ or tau suspension was applied to a 200-mesh Formvar-coated copper grid (Ted Pella, Inc.), and held suspended above the benchtop with a pair of reverse tweezers for 10 min to allow for adsorption. Grid was washed three times by placing the sample side in contact with three droplets of water. The grid was then stained with a droplet of 2% uranyl acetate for 10 min. Excess stain solution was removed with a Kim wipe applied gently to the edge of the grid, and allowed to air dry. Visualization of

the deposited sample was performed on a JEOL JEM-2000 FX transmission electron microscope operated at 200K eV.

2.11 Circular dichroism.

CD spectra were acquired on a nitrogen purged JASCO J-1500 equipped with a Peltier heating system and coolant (water) circulation pump. A 1 mm path-length fused quartz cuvette (200 µL sample volume) was used to acquire the majority of the spectra. In some cases, a low volume Micro-sampling disc was used. This apparatus was able to suspend a small drop (12 µL) of solution between two fused quartz windows at a fixed distance. The path-length for the Micro-sampling disc was also 1 mm.

Most often spectra were acquired by averaging three to four successive wavelength scans from 260 nm to 190 nm, with a data pitch 1 nm, data integration time of 4 s, scan speed of 50 nm/min, and 2 mm band and slit widths. Raw spectral data was recorded in θ, deg, and converted to mean residue ellipticity [θ], deg cm^2 $dmol^{-1}$ with the equation

$$[\theta] = \theta \times \frac{MRW}{10 \times l \times c} \tag{6}$$

where MRW is the mean residue weight of Aβ42 (4514.1 g/mol)/42 residues, *l* is the path length in cm, and c is the concentration in g/cm^3.

2.12 Aβ C-terminal selective ELISA.

Aβ42/Aβ40 ratios in SEC fractions of mixed isoform preparations were determined by comparing the Aβ42 concentration as estimated against an Aβ42 standard curve, using an Aβ42-specific ELISA, with the Aβ40 concentration as estimated against

an Aβ40 standard curve, using an Aβ40-specific ELISA. Briefly, 96-well-plates were coated overnight at 25 ºC with 100 µL 5 µg/mL monoclonal Ab2.1.3 (Aβ42 specific) or Ab13.1.1 (Aβ40 specific) capture antibody (Mayo). Then the wells were washed three times with cold phosphate-buffered saline (PBS) containing 0.05% Tween-20 wash buffer, and blocked with 300 µL PBS with 1% BSA, 5% sucrose and 0.05% NaN_3 blocking buffer for 1 h at 25 ºC, followed by a single wash. 50 µL 20 mM Tris (pH 7.3) with 150 mM NaCl, 0.1% BSA, and 0.05% Tween 20 sample diluent was added. All Aβ samples and standards were diluted first to 10 µM in aCSF, then 1 µM in 8 M GuHCl to induce disaggregation or "relaxation" of highly fibril-like structures. Further dilutions were made as necessary in PBS containing 0.1% BSA. 50 µL amounts of diluted standard or sample were added to the wells, followed by incubation at 25 ºC for 2h. After three washes, 100 µL 0.123 µg/mL Ab5-HrP in 20 mM Tris with 150 mM NaCl and 0.1% BSA was added, and incubated at 25 ºC for 2 h. After a final three washes, detection was performed with 3,3',5,5'-tetramethylbenzidine (TMB) and H_2O_2. The peroxidase reaction was stopped by the addition of 1% H2SO4 solution. The optical density of each sample was analyzed at 450 nm with a reference reading at 630 nm using a SpectraMax 340 absorbance plate reader (Molecular Devices, Union City, CA). The concentration of Aβ40 and Aβ42 in the experimental samples was calculated from Aβ standard curves of 1000-10000 pM. When necessary, samples were diluted to fall within the standard curve.

I performed a significant amount of additional work to develop this method for our use. Important elements of that work, including detection antibody conjugation, antibody concentration selection, and tests to ensure no cross-reactivity between isoform-specific antibodies, are described in the subsections below.

2.12.1 Ab5-HrP conjugation.

Monoclonal Aβ antibody (gift from Mayo Clinic Jacksonville) Ab5 was conjugated to horseradish peroxidase (HrP), based on the method of G. B. Wisdom (Wisdom 2005). The reaction mechanism is described in Figure 2.1A, and the protocol is described here. Briefly, 2 mg HrP (Sigma) was dissolved in 400 µL water, then incubated at room temperature for 20 minutes with 100 µL of 0.1 M sodium periodate on an orbital shaker protected from light. The enzyme was then dialyzed at 4°C against 1 mM sodium acetate buffer, pH 4.4 overnight. Ab5 was received at a concentration of 1.77 mg/mL in PBS. A 200 µL aliquot was diluted with 300 µL of 10 mM sodium carbonate buffer, pH 9.5. A 190 µL aliquot (0.95 mg) of the dialyzed HrP solution was diluted with 10 µL of 200 µM sodium carbonate buffer, pH 9.5, and immediately added to the Ab5 solution. The mixture was incubated for 2 h at room temperature on an orbital shaker. 50 µL of 4 mg/mL sodium borohydride solution, freshly prepared, was added, and the mixture was incubated at 4°C for 2 h on an orbital shaker.

The conjugates were purified on a Tricorn Superdex 75 10/300 GL column (GE Healthcare) using an AKTA FPLC system (GE Healthcare) (Figure 2.1B). Prior to injection of the conjugate solution, the Superdex 75 column was coated with sterile bovine serum albumin (Sigma) to prevent any non-specific binding of antibody to the column matrix. The absorbance of each fraction was assessed at 280 nm (protein) and 403 nm (HrP heme groups) (Figure 2.1C) in a 1 cm quartz cuvette. This would allow us to quantify the Ab5 concentration in the void peak fraction, using some information provided by the HrP manufacturer. The math involved is described in the following subsection.

2.12.2 Ab5-HrP concentration determination.

The included peak maximum (fraction 18) 280 nm Absorbance, A_{280}, was 53.64 mAU, and the 408 nm Absorbance, A_{408}, was 93.37 mAU. It may be shown by rearranging Beer's Law that the ratio between these two, Z/R, is also the ratio of their extinction coefficients ε_{280} and ε_{480}.

$$\left(\frac{Z}{R}\right)_{18} = \frac{A_{280,HrP}}{A_{408,HrP}} = \frac{53.64\ mAU}{93.37\ mAU} = 0.57 = \frac{\varepsilon_{280,HrP}}{\varepsilon_{408,HrP}} \tag{7}$$

There are two assumptions which must be made: pure HrP and HrP conjugated to Ab5 do not have significantly different extinction coefficients, and Ab5 has a typical IgG extinction coefficient: 1.36 mL mg^{-1} cm^{-1}. Then the 408 nm absorbance in the void peak maximum (fraction 14) may be used to calculate the 280 nm absorbance due to HrP in that fraction. Then substituting and rearranging Beer's Law, to calculate the concentration of Ab5 in the void peak fraction:

$$c_{Ab5,F14} = \frac{A_{280,tot} - A_{403,F14} \cdot \left(\frac{Z}{R}\right)_{F18}}{\mathcal{E}_{280,Ab5} \cdot \ell}$$

$$\frac{404.9 - 123.9 \cdot 0.57}{1.36 \frac{mL}{mg \cdot cm} \cdot 1cm} = 0.247\ {}^{mg}/_{mL} \tag{8}$$

The Ab5 concentration of the void peak fraction was 0.247 mg/mL, with side fractions of 0.057, 0.146, and 0.035 mg/mL.

Figure 2.1 Ab5-HrP conjugation.

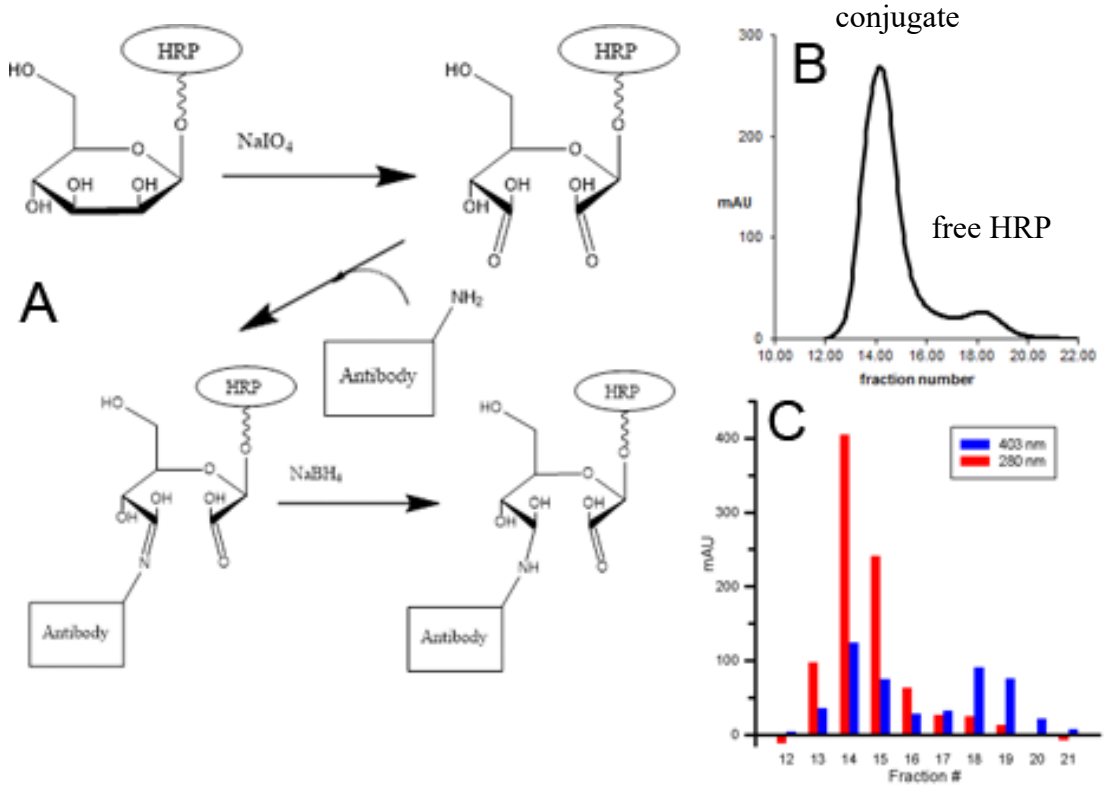

(A) Ab5-HrP conjugation mechanism. HrP Monosaccharides are oxidized with periodate to produce aldehydes, which react with amino groups on the antibody to form Schiff bases. These are reduced with borohydride to form stable linkages. (B) Purification of conjugate via SEC, monitored at 280 nm. Void peak is Ab5-HrP conjugate. Included peak is unconjugated HrP. (C) Fractions were collected and absorbance measured at 280 nm (protein, red) and 403 nm (HrP heme, blue).

2.12.3 Assay antibody concentration selection and validation.

I designed a series of experiments to determine appropriate capture and detection antibody dilutions for ELISA determination of isoform concentrations in mixtures of Aβ42/Aβ40. First I selected a standard curve range based on the total Aβ concentration range determined in-line with SEC via 280 nm absorbance, and considered what would be convenient for dilution, keeping in mind that linearity and sensitivity were both important. I settled on 2400 pM to 150 pM for the standard curves used in method development. Based on conversations with workers at Mayo Clinic, 5-10 µg/mL would be sufficient for the capture antibodies. Therefore, the next step was to determine a good working concentration for the Ab5-HrP conjugate detection antibody. I prepared five sets of wells with 10 µg/mL Ab2.1.3 capture antibody and Aβ42 standard curve dilutions. Then the Ab5-HrP peak fraction, with an Ab5 concentration of 2.47 mg/mL, was applied at dilutions of 1:500, 1:1000, 1:2000, 1:5000, and 1:10000. The results are shown in Figure 2.2A. Based on these results, it was decided that 1:2000 was an appropriate dilution. At this dilution, the Ab5 concentration was 0.123 µg/mL. When side fractions were used instead of the peak fraction, they were diluted to this concentration from the stock concentrations given above.

Next I confirmed the specificity of Ab2.1.3 for Aβ42, and Ab13.1.1 for Aβ40 (Figure 2.2B). For these experiments, Aβ42 standard curve dilutions were added to wells coated with either 100 µL 5 µg/mL Ab2.1.3 or Ab13.1.1, and the same for Aβ40 standard curve dilutions. Detection was performed with 100 µL 0.123 µg/mL Ab5-HrP conjugate and TMB substrate as usual. The results are compared in Figure 2.2B.

During my initial development work and investigation, I noted a significant reduction in standard curve response which seemed to correlate with time from monomer standard purification. To address this issue, which would seriously complicate my future attempts to measure isoform content in aggregated unknown samples, I considered strategies to induce disaggregation of aged monomer. I found that if the standard and sample preparations included an intermediate dilution step into the chaotropic agent GuHCl, I could rescue the signal response in aged monomer samples.

Figure 2.2. C-terminal Aβ ELISA method development.

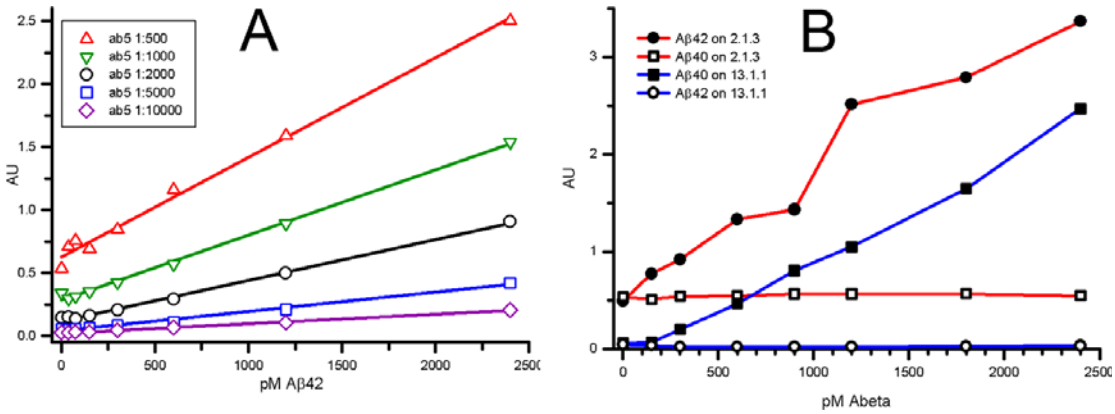

(A) Assay dilution selection for ab5-HrP detection antibody conjugate. Wells were prepared using 100 µL 10 µg/mL ab2.1.3, Aβ42 standard curves (150 to 2400 pM) were prepared as described in section 2.10. Aβ C-terminal selective ELISA. Ab5 was prepared in the same diluent as described in section 2.10, was prepared across a range of dilutions. (B) Test for cross-reactivity was performed using the assay protocol described in section 2.10, except for combinations where the antigens were plated on the non-specific antibody, as indicated in the legend.

2.13 Aβ indirect ELISA.

Except where noted in the text, this was the method we followed to perform indirect ELISA of Aβ samples with the novel AbSL anti-serum. Aβ (previously diluted to 2 μM in eluent) samples and standards were diluted into 0.05 M sodium bicarbonate (pH 9.6) coating buffer. 50 μL volumes were added to wells of a 96-well immunoplate in the desired number of replicates. The plate was sealed and incubated overnight at 25 ºC. coating solution was removed, and wells were washed once with >150 μL 1X PBS (pH 7.4) and 0.2% (v/v) Tween 20 wash buffer. 150 μL 1X PBS (pH 7.4), 0.2% (v/v) Tween 20 and 10% (w/v) dry milk blocking buffer was added to each well, plate was sealed, and incubated at 25 ºC for 1 h. Wells were washed three times as described above, then 100 μL dilute primary antibody in 1X PBS (pH 7.4), 0.2% (v/v) Tween 20 and 5% (w/v) dry milk antibody diluent was added, plate was sealed, and incubated at 25 ºC for 1 h. Wells were washed four times as described above, and 100 μL dilute secondary antibody in antibody diluent was added, plate was sealed, and incubated at 25 ºC for 2 h. Wells were washed four times as described above. 100 μL active TMB substrate solution was added in each well. After 3 minutes TMB reaction was stopped by addition of 100 μL 1 M H_2SO_4. The absorbance at 450 nm was measured in a platereader, with an additional measurement at 630 nm subtracted to correct for well-well differences in the plate material.

2.14 Aβ dot blot.

Nitrocellulose membrane (Hybond-P, Amersham Biosciences) was soaked in milliQ water for 2 min, then removed and allowed to dry in air for 20 min. 2 μL of

sample was allowed to adsorb for 20 min. Membrane was placed in an appropriately-sized dish with 5 mL 1X PBS (pH 7.4), 0.01% (v/v) Tween 20, and 10% (w/v) dry milk blocking buffer, and incubated with gentle shaking for 1 h. Blocking buffer was decanted, and replaced with 5 mL dilute primary antibody in 1X PBS (pH 7.4) 0.2% (v/v) Tween 20, and 5% (w/v) dry milk antibody diluent, and membrane was incubated with gentle shaking for 1 h. Antibody was decanted, and membrane was washed three times with 5 mL portions of 1X PBS (pH 7.4) and 0.2% (v/v) Tween 20 wash buffer, with gentle shaking for 5 min each wash cycle, replacing the wash buffer after each 5 min cycle. Final wash was decanted and replaced with 5 mL dilute secondary antibody in antibody diluent described above, and membrane was incubated for 1 h with gentle shaking. Dilute secondary antibody was decanted, and membrane was washed three more times as described above. Final wash was decanted and replaced with 6 mL ECL substrate (Pierce), and membrane was incubated for 1 min with vigorous shaking. Membrane was removed from dish and pressed lightly between two sheets of filter paper to remove excess solution, then placed between to protective sheets of transparent plastic. Chemiluminescence was visualized on X-ray film. All steps were performed at 25 ºC.

CHAPTER 3.

CHARACTERIZATION OF SEEDED TAU OLIGOMERS.

3.1 Introduction.

3.1.1 The basics of tau protein aggregation.

Several neurodegenerative diseases, including AD, present characteristic tau aggregation pathology (Wang et al. 2016). Native tau is primarily a disordered protein, with only small regions of significant secondary structure (Mukrasch et al. 2009). The microtubule binding region (MTBR) is essential for native microtubule binding functionality, *and* pathologically-linked paired helical filaments (PHF) which make up the characteristic tau inclusions (NFT) found in AD brain (Wischik et al. 1988). Two hexapeptide sequences, ^{275}VQIINK^{280} and ^{306}VQIVYK^{311} at the beginning of the R2 and R3 repeat inserts are necessary and sufficient to initiate PHF aggregation. The hexapeptides readily undergo amyloid aggregation to form β-sheet structures in solution, and their aggregates efficiently seed aggregation of full-length tau into PHF (von Bergen et al. 2000).

3.1.2 Tau pathology in AD.

Insoluble tau appears to be relatively inert, and not directly toxic; switching off tau expression in mouse model of tauopathy rescues cognitive deficits, even though NFTs remain (Santacruz et al. 2005, Sydow et al. 2011, Van der Jeugd et al. 2012). Indeed, insoluble aggregated tau may exert a neuro-protective effect, by sequestering soluble tau oligomers (Alonso Adel et al. 2006). Nonetheless, and despite partial compensation by other microtubule associated proteins (MAP) such as MAP1A, normal tau function is required to avoid pathology. Tau knockout mice also have cognitive deficits; reduction of available tau via incorporation into NFTs is a clear loss-of-function in AD (Lei et al. 2014).

Because all pathologies associated with tau cannot be ascribed to NFTs, much interest has been turned to oligomeric tau as the primary active species in tauopathies. The role of oligomeric tau in AD pathology remains an area of debate and active research, but it has been implicated in multiple AD neuropathological processes. These involve loss-of-function effects, but certainly involve toxic gain-of-function effects (Guerrero-Munoz et al. 2015). Tau oligomers have been found at very early stages of AD, prior to clinical symptom onset (Maeda, Sahara et al. 2007, Lasagna-Reeves, Castillo-Carranza et al. 2012). AD brain is greatly enriched for tau oligomers, compared to control (Himmelstein, Ward et al. 2012). Oligomeric tau, applied extracellularly, is taken up into cells causing increased calcium levels. When oligomeric tau is injected into mice, mitochondrial and synaptic dysfunctions occur (Berger, Roder et al. 2007,

Lasagna-Reeves, Castillo-Carranza et al. 2011). In addition, improper localization of tau from the axon to dendrites may promote synaptic dysfunction in an oligomeric tau-dependent manner (Guerrero-Munoz et al. 2015).

Various pathogenic forms of tau have been shown to inhibit anterograde kinesin-mediated fast-axonal transport (Combs et al. 2016). This inhibition appears mediated by conformational changes associated with oligomerization (Cox et al. 2016). An N-terminal phosphatase-activating domain (PAD) becomes exposed upon aggregation, which activates protein phosphatase 1 (PP1), which in turn activates glycogen synthase kinase 3β (GSK3). Active GSK3 phosphorylation of kinesin mediates release of cargo, disrupting transport. The 4R tau isoforms demonstrate more extensive exposure of the PAD region upon oligomerization than the 3R isoforms, however both types can mediate this transport inhibition. The authors used arachidonic acid to induce oligomerization. The 4R isoforms formed a range of filaments up to around 600 nm in length, as well as globular oligomeric species. On the other hand, induced oligomerization of the 3R isoforms with arachidonic acid resulted in an oligomer population primarily comprised of the globular species, with filamentous species occurring rarely.

3.1.3 Prion-like spreading of tau pathology.

An important aspect of tau pathology in AD is the stereotypical pattern of tau pathology "spreading" along neuronal connections as the disease proceeds (Clavaguera et al. 2009, Frost et al. 2009, Guo et al. 2011, Goedert et al. 2014, Polanco et al. 2015) (Figure 3.1). This concept of tau spreading was originally conceived as a post-mortem tool for diagnosis to describe the extent of the disease. It has since gained much support

from studies on the cellular scale. Today, tau spreading via intercellular transfer is backed-up significant experimental evidence (prion-like propagation). According to this model, tau aggregate "seeds" formed intracellularly, are released into the extracellular space, are taken up into nearby, synaptically connected cells, and induce additional aggregate formation via templated conformational change.

The Kayed Lab (Lasagna-Reeves et al. 2012) immunoprecipitated tau oligomers from AD brain, then injected them into the hippocampus of WT transgenic human tau mice. After a year, tau positive inclusions were found both at the injection and distal regions of the brain. This property has also been demonstrated in a transgenic mouse model (Clavaguera et al. 2009). The authors developed a transgenic mouse line which expresses the P301S tau mutant form, which causes familial frontotemporal dementia in humans (Spillantini et al. 2000). They took brain extracts from these mice, and injected them into the hippocampi of transgenic WT human tau mice, and observed insoluble tau inclusions both at the site of injection and at distant areas which were connected synaptically to the injection site. A later study (Liu et al. 2012) in another mouse model lends further support to this concept.

On a cellular level, the mechanisms of tau exit from and uptake into, as well as translocation within, neuronal cells have been studied. In one work (Saman et al. 2012) cerebrospinal fluid (CSF) from mild-AD patients was analyzed, as well as conditioned media from neuron-like cells with inducible tau expression. AD CSF and the media were enriched for phosphotau-positive exosomes. The pattern of phosphorylation was consistent with that found in early AD, and both monomeric and oligomeric (but not insoluble fibrillar) tau was present. This suggests a secretory pathway for release of

pathological tau into the extracellular space. Interestingly the same pathway has been implicated for propagation of misfolded prion protein (PrP^{Sc}) (Vella et al. 2007). Wu and co-workers (Wu et al. 2013) showed that LMW tau oligomers and small fibrils (but not monomer or long fibrils) are endocytosized at the somatodrendritic and axon compartments of neurons, and can be transported in anterograde and retrograde fashions. Another study (Holmes et al. 2013) further refined the model for uptake, showing that small fibrillary tau seeds, at least, are taken up in a heparin sulfate proteoglycan (HSPG) binding-dependent manner. Escape from macropinosomes and endosomes may occur via direct interaction of tau with the cell membrane; pore formation by other amyloid aggregates has been proposed (Kayed et al. 2004, Relini et al. 2004), and oligomeric tau can permeabilize artificial membrane liposomes (Flach et al. 2012). Finally, in a recent study, the same group explored further the size dependence of tau aggregate uptake and seeding (Mirbaha et al. 2015). All aggregate sizes between n=1 and n=100 (n=100 were largest they characterized) bound the cell surface in a HSPG dependent manner. However, only trimer and larger aggregates, up to n=100 were taken up into the cell. Furthermore, only the oligomers which were taken up into the cell could seed further aggregation intracellularly. These results, carried out using recombinant tau constructs, were verified further using AD brain-derived aggregates.

Despite this well-structured model, much debate remains concerning the spread of tau pathology. Kim, *et al*. (Kim et al. 2015) demonstrated tau pathology spreading dependent on a dimeric conformation of the P301L mutant form of tau, found in some familial FTD. This seems to contradict the conclusion of the previously cited study, where trimeric tau was the minimal oligomer. Michel, *et al*. (Michel et al. 2014) showed

that the presence of extracellular monomeric tau alone was sufficient to induce spreading of tau pathology, placing release of tau from the cell upstream of tau oligomerization. Compare this to various other studies, such as (Tepper et al. 2014) who demonstrated phosphorylation-dependent aggregation, or (Hu et al. 2014) where intracellular tau aggregation was induced via treatment with Aβ42.

Figure 3.1 Braak staging of tauopathies.

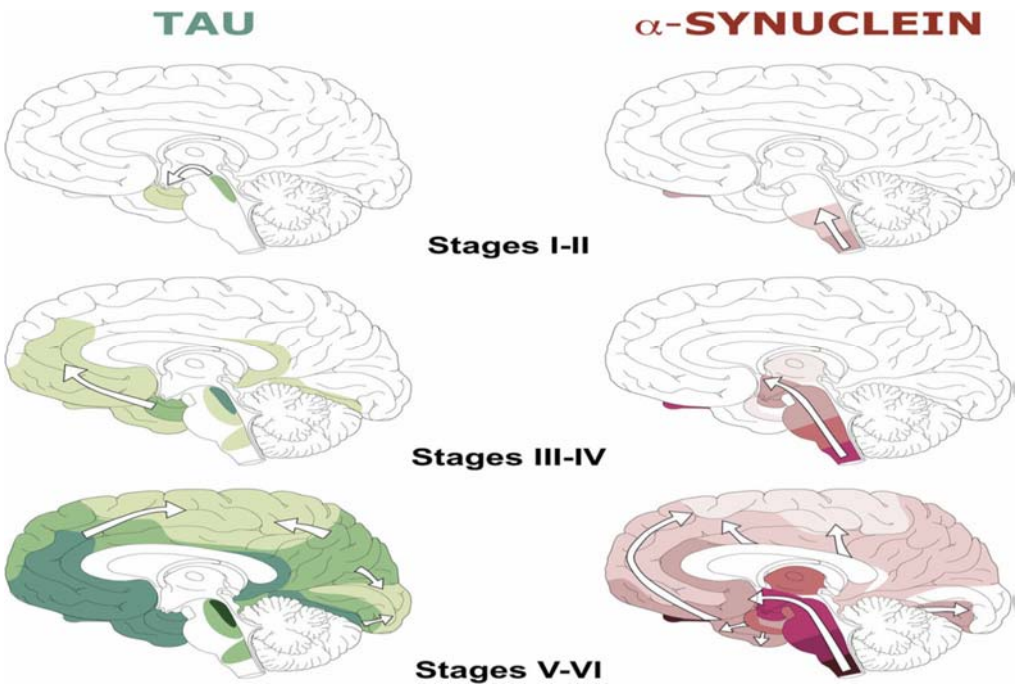

Spreading of tau inclusions as AD progresses. First described by Heiko Braak in 1991, based on a large sample set of post-mortem human AD and control brains. Later Braak described similar phenomenon in PD with α-synuclein spreading. In AD, NFT histology is present mainly in the transentorhinal region during Braak stage I and II. In stage III and IV NFTs appear in the limbic regions such as hippocampus. By Braak V and VI, the NFTs are present in a large portion of the neocortex. The figure is from Goedert et al. 2014.

3.1.4 Identified tau oligomers *in vivo* and *in vitro*.

The Kayed Lab developed a novel method for generation of neurotoxic tau oligomer (Lasagna-Reeves et al. 2010, Lasagna-Reeves et al. 2011). They used preformed Aβ or α-synuclein seeds to form tau oligomers in tau monomer solution, paralleling work by other groups (Hu et al. 2014) on the spreading of tau pathology. Isolated tau oligomers generated in this fashion were capable of seeding oligomerization when added to fresh monomer solutions, and this capability is retained through multiple seeding-purification cycles. The oligomers were identified as apparent trimers based on SDS-PAGE and SEC. The oligomers generated were neurotoxic in cell culture, and *in vivo* cause synaptic and mitochondrial dysfunction, when injected into WT mice.

However, a large number of other soluble tau oligomer species have been identified, and it is sometimes difficult, based on the techniques used, to determine if two different species are actually just subtle variations on one conformation (Cowan et al. 2013).

Wille and co-workers. (Wille et al. 1992) generated dimeric, rod-like species *in vitro* from recombinant tau constructs. Inspection with EM gave an estimated length of 22-25 nm, which is consistent with the repeat region of PHF. The Takashima group (Sahara et al. 2007) described two different apparent dimers. They differed in that one depended on inter-molecular disulfide bridges between microtubule binding regions. Both forms were identified *in vitro* as well as in a transgenic mouse model, and described as 140 kDa small soluble oligomers. Apparent dimeric/trimeric species have been generated and characterized *in vitro* in addition to those described above. Dimers have been reported with molecular weights of 180 kDa (Patterson et al. 2011), and 130 kDa

(Makrides et al. 2003), while trimers have been described with molecular weights of 120 kDa (Lasagna-Reeves et al. 2010). Small oligomers of apparent dimer/trimer size have also been isolated from human AD brain (Henkins et al. 2012). The size estimations in the above studies were done based on electrophoretic mobility, SEC, or at best interrogation with EM or AFM. To our knowledge, no one has made size measurements on small tau oligomers using light scattering techniques.

3.1.5 Templated oligomerization.

The 120 kDa apparent trimers described by the Kayed Lab (Lasagna-Reeves et al. 2010) are particularly interesting. SEC-purified recombinant Full-length human tau isoform 2N4R monomer (Margittai et al. 2004, Margittai et al. 2006) was seeded with small amounts of A11-positive (indicating spherical oligomeric amyloid conformation) Aβ or α-synuclein oligomers. The resulting tau oligomers could also be used to seed tau monomer in the same manner as the Aβ or α-synuclein oligomers, even after multiple successive seeding cycles. (Figure 3.2). The initial ratio of seed to monomer was 1:140, which agrees with other amyloid seeding experiments from the literature, including other heterogenous seeding reactions (Jarrett et al. 1993, Kelly 2000, O'Nuallain et al. 2004).

SEC elution of the 2N4R tau oligomer yielded an estimated molecular weight of 150-190 kDa, while SDS-PAGE gave an estimated molecular weight of ~120 kDa. Both indirect measures of molecular weight were consistent with a trimeric species. Bis-ANS binding assays revealed a large increase in hydrophobicity at the oligomer surface, compared to monomeric and fibrillar tau. In addition, circular dichroism measurements indicated high β-sheet content when compared to monomeric tau, which is

characteristically random-coil. Despite their high β-sheet content, the tau oligomers did not bind Congo red or thioflavin T, two common probes known to bind amyloid filament-like structural motifs. Others (Sahara et al. 2007) have noted that LMW tau oligomers do not bind these dyes. However, in that case the oligomers were formed via heparin induction, and the authors described them as dimeric; the Kayed lab identifies their oligomers as trimeric. The oligomer populations also appeared to have some degree of polydispersion, and this was borne out in TEM and AFM imaging. This polydispersion can be explained by the stochastic nature of amyloid aggregation; it is well known that replicate aggregation reactions often will aggregate at quite different rates, and it is challenging to generate time dependent aggregation data with low standard error measures (Teplow 2006). Finally, if the seeding incubation time is extended beyond what is stated in the methods, the oligomers will continue to aggregate and form filamentous structures.

Figure 3.2 Generation of tau oligomer via seeding.

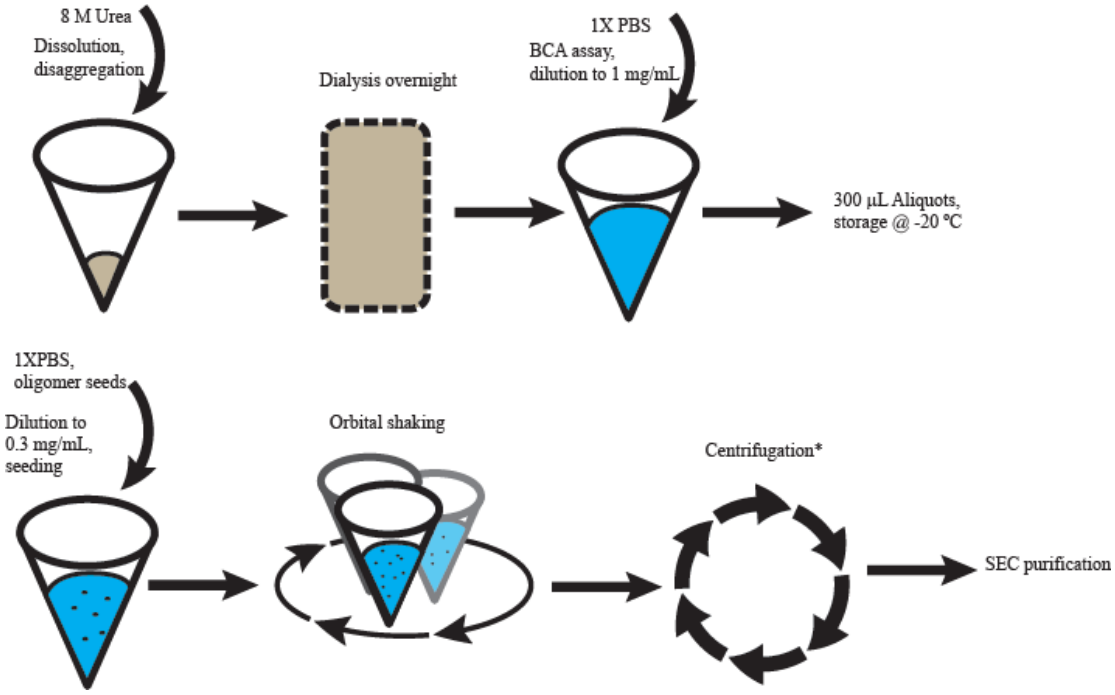

Recombinant Tau pellet was reconstituted in fresh 8 M Urea followed by overnight dialysis. Concentration was determined via BCA and normalized to 1 mg/mL. 300 µL aliquots were taken and stored at -20 ºC. For seeding, an aliquot was thawed, diluted to 0.3 mg/mL (1 mL), and seeds added. The aliquot was then shaken on an orbital shaker for 2 h. This was followed by centrifugation (in some cases; not included in method as published), and SEC elution.

3.1.6 Challenges in the study of tau oligomer.

Much of the challenge in determining the specifics of oligomeric tau-related pathology stems from experimental methodology. Many different preparations are used, and different tau isoforms, and characterization of generated species is often not thorough. The methods used to assay toxicity suffer from similar problems; results in cell culture may differ from primary neuron, or in vivo (Wang and Mandelkow 2016), making it difficult to draw complete conclusions.

For the identification of therapeutic targets, as well as understanding amyloid disease processes at the molecular level, it is vital that researchers strive to develop material preparations which yield well defined, homogeneous (or at least well characterized) aggregate species. There are numerous examples of why this is so important. When studying the biophysics or kinetics of aggregation in vitro in monomeric amyloid solutions, it is very important to begin with pure monomer starting solution. Pre-existing aggregates alter the aggregation profile by acting as seeds, which can shorten or eliminate the lag phase. Additionally, the templating phenomenon noted in some amyloid systems creates the possibility of different conformational trajectories in the aggregated solution. These can interact in different ways with signaling, and other cellular mechanisms, therefore thorough characterization becomes critical for cell and in vivo studies as well.

To extend the biophysical analysis of tau oligomers generated via their novel seeding model, a collaboration was initiated with the Kayed Lab. The first objective was to replicate their original published results (summarized in section 3.1.5) and expand them with the additional analytical options we have at our disposal. Then the scope of the analysis would be broadened to include alternate tau isoforms and seed types, in an attempt to determine any differences between oligomer morphology, and/or seeding potential. An important component of the analysis, which distinguishes the Nichols Lab from many others in the field, is experience with molecular weight determination via MALS in-line with SEC (SEC-MALS). DLS can probe hydrodynamic radius, and yield another complementary measure of molecular size. Tau dimers and trimers are well reported in the literature, with overlapping size ranges. It is currently unclear if these two species truly represent different oligomerization states, or more subtle conformational changes within a single aggregate structure (Cowan et al. 2013). The hope is this work will help clarify these important questions about the biophysics of tau.

3.3 Results.

3.3.1 Instrument and sample preparation validations.

Valid methods are required for valid data. Importantly, the SEC-MALS system must be able to resolve monomeric and oligomeric tau species, and yield accurate molecular weight data. To confirm that the normalization procedures generated proper correction factors, and assess the column for appropriateness, I employed another protein standard, yeast Alcohol Dehydrogenase (yADh) (SigmaAldrich), a highly structured, anisotropic scatterer. This well-characterized oxidoreductase enzyme plays an indispensable role in the production of Beer, a substance which is highly prized by many graduate students. yADh is a homotetramer, and each subunit is 347 amino acids long. The deposited structure (4W6Z) of the asymmetric unit has a calculated molecular weight of 149.5 kDa, within the estimated molecular weight range of the tau oligomers generated at the Kayed Lab (Lasagna-Reeves et al. 2010). When subjected to SEC-MALS analysis (Figure 3.3), the resulting molecular weight profile across the yADh peak appeared bimodal. Measured molecular weight was 168 kDa when the entire elution peak was considered. However, if only the tailing side was considered, the measured molecular weight was 162 kDa. This second value may be more accurate. Since functional yADh is a tetramer, it is reasonable to ascribe the leading-edge increase to a limited amount of supramolecular assembly. Although the theoretical and experimental molecular weights differ by an appreciable amount, I considered the two close enough to accept the validity of my molecular weight measurements. I did so on grounds that the

difference was sufficiently small compared to the molecular weight of a 2N4R or 2N3R tau monomer that it would not hamper resolution of differing tau oligomer states. Molecular weights are summarized in Table 3.1.

Next, there is evidence in the literature of a cysteine-dependent tau dimer, and it has been observed both in vitro and in vivo in mouse models (Sahara et al. 2007). Cysteine-dependent apparent tau dimers might be relevant to our in vitro system, either as preformed species in the monomer pool, or forming spontaneously in parallel to the seeded oligomerization reaction, either of which could alter aggregation outcomes. Dithiothreitol (DTT), a well-known reducing agent, was used in the preparation of my recombinant tau protein, and might induce this change in aggregation profile. To test this hypothesis, I added an excess of DTT to a reconstituted monomer aliquot prior tocould perturb their activity in a manner detectable by SEC-MALS. To investigate this possibility, 300 μM aliquots of monomeric 2N3R tau were treated with either DTT (2 mM) or buffer, and allowed to incubate at room temperature with shaking for 2 h prior to SEC injection. The results are summarized in Figure 3.4. Both tau peaks were centered on fraction 18. The (+)DTT preparation peak had a MALS determined molecular weight of 55 kDa, while the molecular weight of the (-)DTT preparation was 59 kDa. The late eluting putative DTT peak of the (-)DTT preparation eluted at the same fraction as a much larger peak in the (+)DTT preparation, further confirming it is indeed DTT which remains after dialysis. Molecular weights are summarized in Table 3.1.

Figure 3.3 Validation of MALS detector normalization with yeast alcohol dehydrogenase.

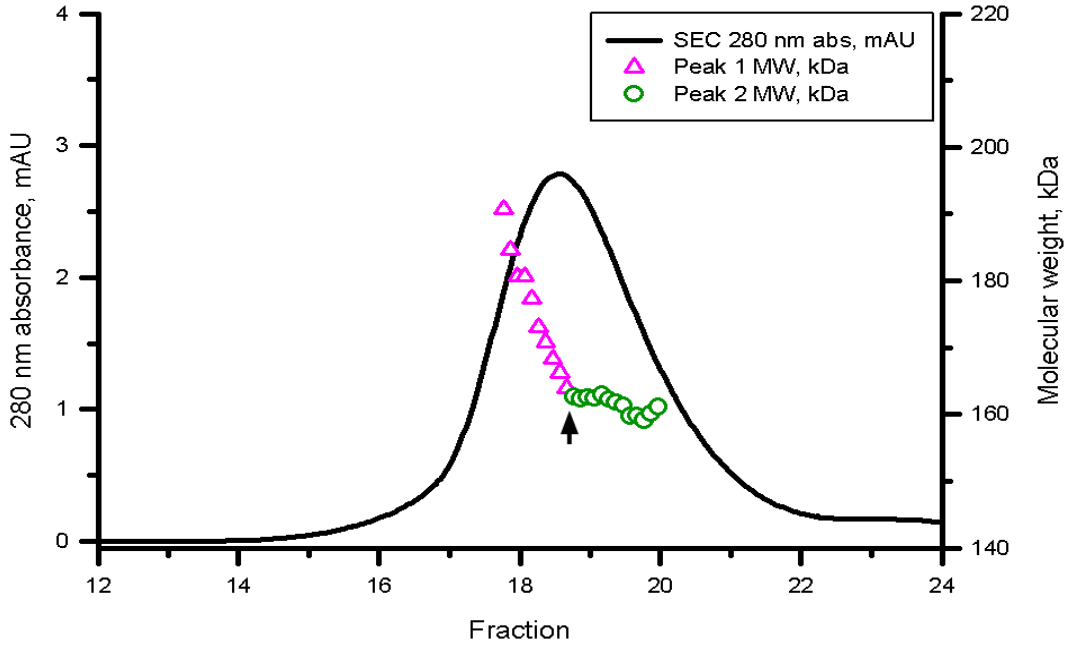

1 mg yADh was dissolved in 1 mL 1X PBS (pH 7.4). After 10 min centrifugation at 18,000 x g, the sample was immediately injected onto the column. SEC-MALS was performed as described in the methods. For clarity, only every third molecular weight data point is displayed. The point of inflection at approximately fraction 18.7 (arrow) was taken to indicate the divide between monomeric and aggregating yADh. Only the monomeric portion, identified as Peak 2, was included in molecular weight calculations. The calculated molecular weight was 162 kDa. The theoretical molecular weight, derived from the best deposited structure available on pdb (4W6Z) was 150 kDa. The 12 kDa error, approximately one fourth the molecular weight of a 2N4R monomer (45.9 kDa) was deemed acceptable for detection of different tau oligomer states.

Figure 3.4 2N3R tau sample preparation with DTT.

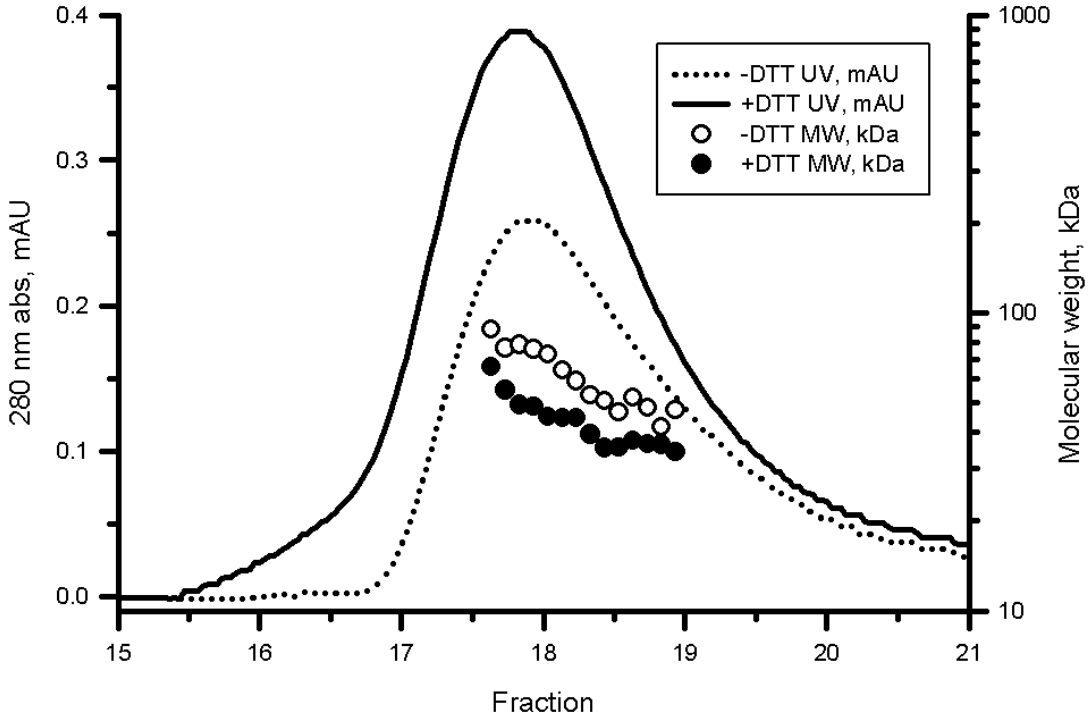

A 300 µL aliquot of 1 mg/mL 2N3R tau was diluted with 700 µL 1X PBS (pH 7.4). The aliquot was stirred overnight, then sub-aliquoted into fresh tubes. To one half was added 10 µL of 100 mM DTT in buffer, while to the other was added buffer alone. At room temperature they were autoswirled for 2 h then centrifuged for 10 min at 18,000 x g, and the supernatants subjected to SEC-MALS analysis as described in the methods.

Table 3.1 Validation experiments molecular weight summary.

The molecular weight data from yADh and 2N3R tau (+/-) DTT validation experiments are summarized below.

Preparation	Molecular weight (kDa)
yADH (theoretical)	149.5
yADH (measured – full peak)	168
yADH (measured – tailing half)	162
(+)DTT	55
(-)DTT	59

3.3.2 2N4R tau seeded with cross-linked oligomer.

Although DTT was shown not to cause detectable changes in aggregation, it did nonetheless lead to complications in the earliest attempts at biophysical characterization. Oligomeric seeds, previously crosslinked with disuccinimidyl suberate (DSS), were used to initate a 2N4R tau oligomerization reaction. The 2N4R tau sample was prepared and seeded as described in the methods, then injected onto the column for SEC-MALS purification and analysis. The resulting SEC profile was unexpected (Figure 3.5A). There were two included peaks. The first peak eluted around fraction 18. The calculated injected mass, based on UV absorbance, was 342 μg. Whereas if the calculations were made using the results of a bicinchonic acid (BCA) protein assay, the injected mass was much lower, 95 μg. The second peak eluted late, around fraction 40, essentially an entire column volume, indicating a very small species. Residual DTT would explain both the protein assay differences, and this large second peak, as DTT absorbs UV strongly at 280 nm. Further details are related in below in section 3.5 Technical discussion. This included peak was also very large, indicating either a highly absorbing species or high concentration in the injected sample.

Further analysis of the purified tau was limited by the low concentration in the void fraction. ThT and bis-ANS dye binding (Figure 3.5B and 3.5C) were elevated above the baseline, indicating presence of β-sheet content, and hydrophobic surface exposure.

Figure 3.5 Purification of 2N4R seeded with 2N4R cross-linked seeds.

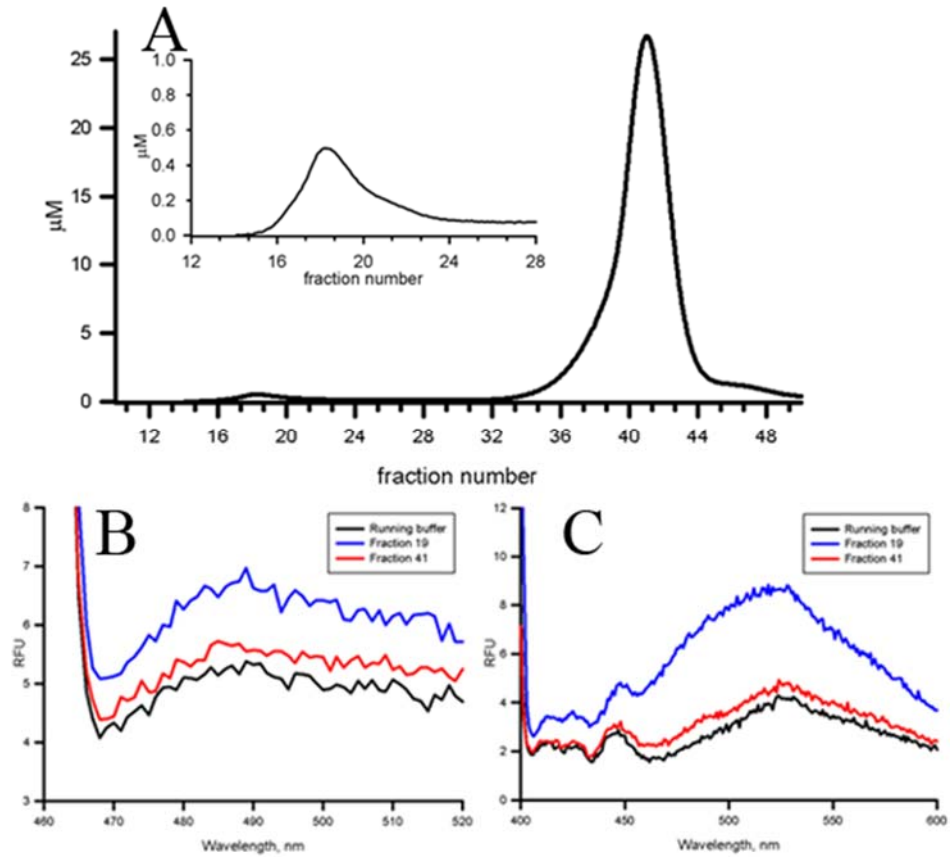

(A) 7 µL of 0.3 mg/mL 2N4R crosslinked seeds was added to 1 mL previously dialyzed recombinant 2N4R Tau monomer. The solution was pipetted to mix for 1 min, then incubated at 25 ºC on an orbital shaker for 1 h, and subjected to SEC analysis. Inset: an expansion of the Tau peak. (B) ThT and (C) bis-ANS fluorescence spectra of Tau peak fraction 19 (blue), DTT fraction 41 (red), and 1X PBS (pH 7.4) running buffer (black). For ThT measurements, 4 uL 0.1 mM ThT was added to 66 µL of sample. Bis-ANS spectra were acquired from mixture of 7 µL 0.1 mM bis-ANS and 63 µL of sample.

3.3.3 Reconstitution and characterization of a 2N3R tau pellet.

My experiments with 2N4R were intended to replicate the Kayed Lab results described above. However, the amount of 2N4R material available hampered those initial efforts. Therefore, I turned my attention to the recombinant 2N3R tau material we received. In addition, some differences between 2N3R and 2N4R aggregation have been noted in the literature (described above) yet only 2N4R has been studied in the current paradigm of templated oligomerization.

The recombinant 2N3R monomer was prepared as described in the methods, with some modifications due to the findings described in the previous section. The solubilizing Urea volume was increased from 30 µL to 75 µL, and incubated at room temperature overnight to ensure maximal denaturation of the material, and the dialysis period was extended, and included an additional buffer change.

In this case, the BCA protein concentration assay result was 1.22 mg/ml, within the expected range of 1-3 mg/mL, as reported to us by the Kayed Lab at UTMB. The UV absorbance measurement, however, was again much higher, at 4.32 mg/mL, despite the extended dialysis. Taking the BCA result to be correct, I normalized the sample concentration to 1 mg/mL. The resulting sample volume was sufficient for 3.5 aliquots of 300 µL each. A 300 µL aliquot was taken, and I performed the seeding procedure as described in the methods, using non-crosslinked 2N4R seeds.

The SEC profile this time was more in-line with the expected results (Figure 3.6A). The void peak eluted at fraction 18. The total eluted protein was 187 µg. Given the injected mass was 300 µg, the recovery was 62%, in good agreement with past experiences using the Superdex 75 column. The late eluting peak appeared in this

preparation as well, however it was greatly reduced. Fractions through the void peak were collected, and UV absorbance and BCA assays were performed to determine if their results would still diverge post-SEC. In this case, they were in relatively good agreement (Figure 3.6A).

The peak fraction (#18) did bind bis-ANS to some extent (Figure 3.6B), indicating some hydrophobic surface exposure, but it did not bind ThT (not shown), indicating no β-sheet content. CD measurements agreed (Figure 3.6C); no classic β-sheet or α-helix structure was detected. For this preparation, Dr. Nichols performed DLS analysis to determine the hydrodynamic radius (R_H) of the peak fractions (Figure 3-6D). The main peak fraction 18 had R_H ~90 nm, while fraction 19 was markedly decreased, R_H ~40 nm.

These R_H values were larger that might be expected; for comparison, Aβ PF have R_H ~6-8 nm (Walsh et al. 1997). There is no satisfying explanation for this, note however, a drastic reduction in both light scattering intensity and R_H from fraction 19 to 18 (Figure 3-6C). DLS measurement of fractions 20-22 may have indicated a continuing downward trend. This is also hinted at upon comparison of the BCA and U/V assay data presented in Figure 3.6A. There is a greater disagreement between the two methods in fractions 18 and 19 than the following fractions, which can be attributed to increasingly large molecule light scattering in the leading fractions.

Figure 3.6 Characterization of 2N3R Tau seeded with uncross-linked 2N4R oligomer.

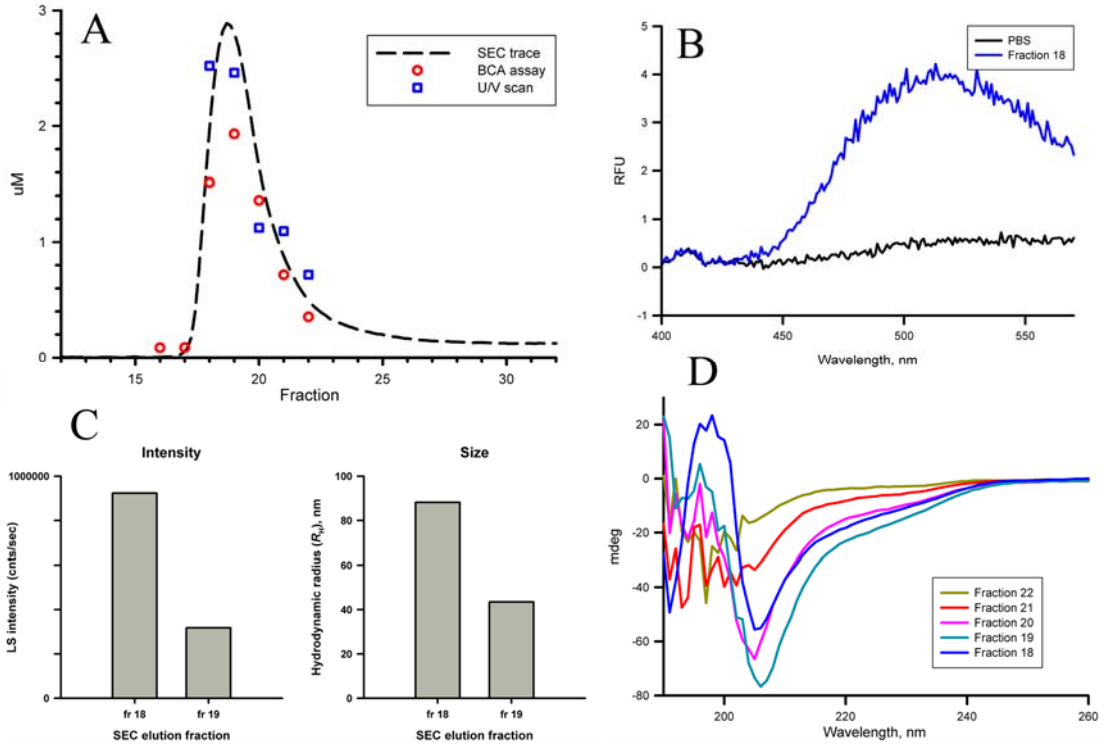

(A) 7 µL of 0.3 mg/mL 2N4R seeds was added to 1 mL 0.3 mg/mL previously dialyzed recombinant 2N3R Tau monomer. The solution was incubated at 25 ºC on an orbital shaker for 1 h before SEC analysis. Concentration determination of collected fractions was performed via 280 nm absorbance in a 1 cm quartz cuvette, and BCA assay, as described in the methods. Results of in-line UV trace and fraction UV absorbances were converted to µM using a path-length of 0.5 cm and a calculated 2N3R Tau extinction coefficient of 7375 M^{-1} cm^{-1}. In-line concentration trace was overlaid with fraction determinations, and their volumes were adjusted graphically until all were aligned. (B) bis-ANS fluorescence spectra of Tau peak fraction 19 (blue) and 1X PBS (pH 7.4) running buffer (black). Bis-ANS spectra were acquired from a mixture of 7 µL 0.1 mM bis-ANS and 63 µL of sample. (C) DLS measurements were taken at 25 ºC in a quartz cuvette. Data was collected at a 90º angle to the incident light, with a 5 s averaging time. (D) CD spectra were collected between 400 and 190 nm, with a data integration time of 2 s and a scan speed of 200 nm/min in a 1 mm quartz cuvette. Each sample was scanned twice and the spectra averaged.

3.3.4 SEC-MALS comparison of seeded 2N4R and unseeded 2N4R.

In my previous trials, including those described above, I was surprised that I had not yet detected more than a single peak I could ascribe to tau. The Kayed Lab (Lasagna-Reeves et al. 2010) reported two fully resolved peaks, one at an estimated molecular weight consistent with trimer, the other monomer. They utilized a TSK-GEL G3000 SWXL (30 cm x 7.8 mm) column for their elutions, which is a HMW-designed column suitable for fractionation up to 500 kDa. On the other hand, I used a GE Superdex 75 10/300 GL. The upper limit of this column is much lower; material larger than 70 kDa will elute in the void peak. However, 2N4R tau, the largest isoform, had a calculated molecular weight of 45.9 kDa, while the other target isoform, 2N3R tau, had a molecular weight of 42.6 kDa. Because of this, I conjectured that the Superdex 75 column should provide sufficient separation of monomer from oligomer (trimer) to be detectable at the minimum as a shoulder on the trailing edge of the void peak, if not fully resolved. Therefore I set out to replicate precisely the preparation described they described (Lasagna-Reeves et al. 2010), and compare the results directly with unseeded monomer (Figure 3.7).

Figure 3.7A displays the results of one unseeded 2N4R tau preparation compared directly with 2N4R tau seeded with uncrosslinked 2N4R tau oligomer. The two preparations were subjected to SEC-MALS in tandem, with the injection of the second preparation following that of the first by less than 1.5 h. Multiple unexpected outcomes are evident in these results. No monomer peak resolved in either preparation. For the

seeded preparation, the three "peaks" identified in the legend had mean molecular weights of approximately 10,710 kDa (peak 1), 340 kDa (peak 2), and 92 kDa (peak 3). For the unseeded preparation, those peaks had mean molecular weights of 10,280 kDa, 1,062 kDa, and 212 kDa, respectively (molecular weight data is summarized in Table 3.2). The monomeric preparation displayed higher molecular weights throughout the included peak, unexpectedly even higher than the seeded preparation. Also evident is a high molecular weight "void shoulder" on the included peaks of both preparations. The molecular weights of the species present in this peak are far too large to represent trimeric tau, as assessed by MALS. Figure 3.7B is an overlay of the same SEC elution UV absorbance data as presented in 3.7A, as well as the raw data from the 90º (right-angle) light scattering detector of the MALS instrument. This data is presented as qualitative evidence for the large size and small amount of this large aggregate present in the preparations. Larger particles scatter light much more efficiently than smaller ones, thus much less is necessary to result in a strong light scattering signal. Figure 3.7C is a TEM image which was generated from a 2N3R monomer preparation which presented a SEC-MALS profile very similar to Figure 3.7A. That 2N3R monomer preparation also had a high molecular weight void shoulder. The void shoulders appear to be composed of large, amorphous, likely insoluble aggregates, possibly consisting of many smaller aggregates.

The void shoulders do not completely resolve from the included peak, confounding molecular weight determinations of smaller species with partially overlapping elutions. To eliminate this issue, future preparations would include an additional centrifugation step prior to injection onto the SEC column.

Table 3.2 SEC-MALS comparison of seeded and unseeded 2N4R Tau.

The molecular weight data presented in Figure 3.7 (below). 2N4R tau was prepared with or without non-crosslinked 2N4R tau oligomer seeds.

Preparation	Molecular weight (kDa)
2N4R (+)seed - peak 1	10,710
2N4R (+)seed - peak 2	340
2N4R (+)seed - peak 3	92
2N4R (+)seed - peak 1	10,280
2N4R (+)seed - peak 2	1,062
2N4R (+)seed - peak 3	212

Figure 3.7 SEC-MALS comparison of 2N4R seeded and unseeded preparations.

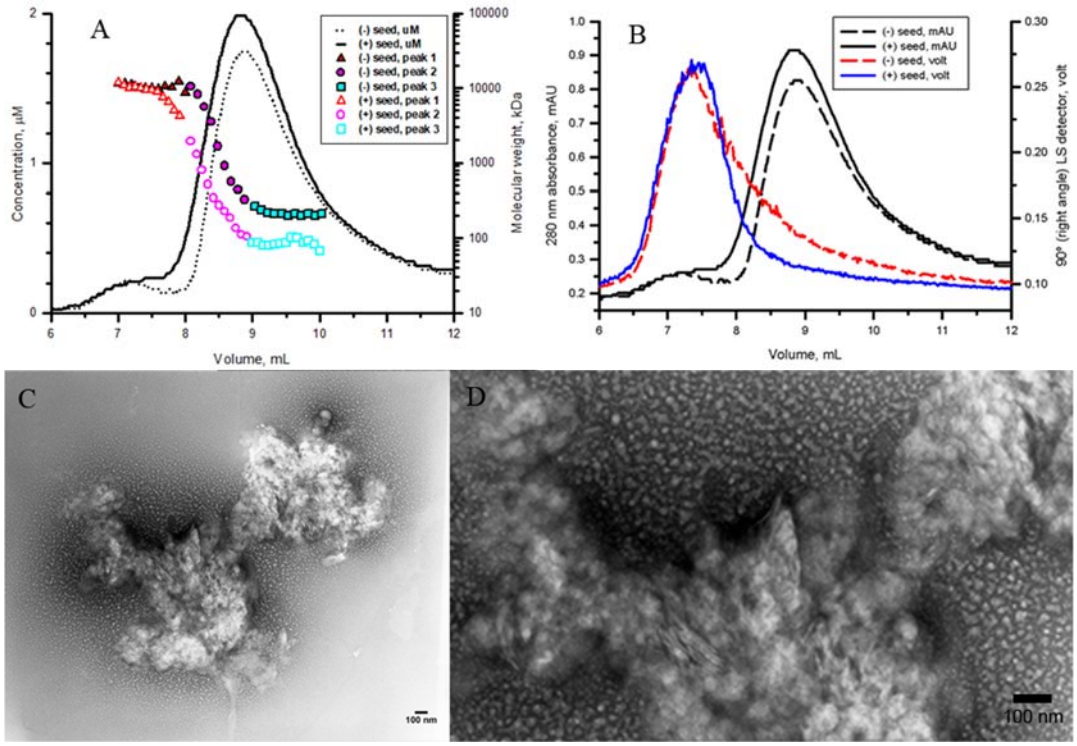

(A) Post-dialysis recombinant 2N4R Tau monomer aliquots (0.3 mg/mL), one seeded with 7 µL uncrosslinked 2N4R Tau seed, the other not, were prepared as described in the methods and analyzed via SEC-MALS within 1.5 h of each other. (B) The same experiment is presented as in panel A, with the SEC in-line 280 absorbance overlaid with the 90º (right angle) detector voltage readings. (C) 2N3R monomeric preparation which displayed similar high molecular weight void shoulder. EM image of void peak fraction. (D) Digitally embiggened view of the same EM. May be suggestive of clumped LMW oligomers.

3.3.5 Detection of 2N3R oligomers and intriguing elutions.

Although no separate monomer and oligomer peaks could be detected, prior data hinted that tau oligomers were formed. These hints included the large difference in RH seen between fractions in Figure 3.6C, subtle differences in secondary structure seen in 3.6D, and divergent elution rates for species of the same molecular weight seen in 3.7A. These observations led me to refine my methods and analysis, to detect subtle differences which might indicate seeding-dependent changes in solutions of monomeric tau. This time I focused on the 2N3R tau isoform. I performed several experiments which not only allowed me to validate my procedures, but improve them. With these results in hand I returned to the generation and characterization of seeded tau oligomers. The 2N3R isoform was more appealing, for reasons which are touched upon in the discussion section which completes this chapter.

The yADh-MALS validation test described above (Section 3.3.1) was precipitated in large part by the strange results of a previous seeding experiment (Figure 3.8) shown below. The objective was nucleation of 2N3R oligomer formation via seeding with oligomers of the 2N4R isoform. 2N3R tau samples with or without uncrosslinked 2N4R seeding were compared via SEC-MALS and SDS-PAGE.

The unseeded preparation peak absorbance maximum was shifted back from the seeded peak (Figure 3.8A). The low molecular weight peak was elevated above monomer in both preparations, indicating that the MALS molecular weights may not be accurate in this case. However, the molecular weight profiles (summarized in Table 3.3) were essentially the same across the peaks, despite their differing elution rates.

I performed SDS-PAGE western blot analysis on these preparations as described in the methods. Staining was performed using two primary antibodies: T22 (Figure 3-8B), generated against the 2N4R oligomers described above and in previous work (Lasagna-Reeves et al. 2010, Lasagna-Reeves et al. 2012), and Tau-5, a common general antibody for tau, which is neither conformation nor isoform specific. The T22 antibody did not bind any visible bands, except a very low molecular weight species close to the loading dye in unseeded fractions 17 and 18. The Tau-5 antibody, on the other hand, bound multiple species in both preparations. There was no staining in the lanes for fraction 15 or 16. The low molecular weight band seen in unseeded preparation fractions 17 and 18 using T22 was also faintly detected by Tau-5. In addition, bands were detected at 50, 150 and 200 kDa. These approximate molecular weights correspond to monomer, dimer/trimer, and tetrameric tau, respectively. The same bands were detected in the seeded preparation, including lighter bands in the higher molecular size fractions 15 and 16.

The disparity between the peak maximum elution rates and molecular weight profiles was intriguing, and relevant to our interest in differences in seeding between tau isoforms. MALS makes absolute measures of molecular weight based on First Principles. SEC elution, however, probes molecular size, which is a related but different measurement influenced by protein folding; SEC determined molecular weights cited in the literature are estimates generated by comparison with ‘well-behaved’ standard proteins. A difference between the two may therefore indicate conformational change, if one conformation is more extended, or the surface exposure significantly different.

As a follow-up to this experiment, I performed another seeding preparation with 2N3R and un-crosslinked 2N4R seeds. I made additional method modifications, this time to clarify any differences between the seeded and unseeded preparations. This involved additional steps to remove pre-existing material, and inhibit spontaneous aggregation over the time course of the protocol. The differences between the new protocol and the protocol used in Figure 3.8 are highlighted in Table 3.6.

The results are reported in Figure 3.9, and molecular weight summaries are given in Table 3.5. The modified protocol succeeded in enhancing the peak fraction elution rate difference between seeded and unseeded samples (Figure 3.9A). 280 nm absorbance maxima were separated by approximately a full fraction volume (0.5 mL). Importantly, the molecular weight profiles were similar. I performed Western blot analysis on these preparations as well. The T22 antibody stain (Figure 3.9B) again did not detect any oligomeric species. When Tau-5 (Figure 3.9C) was used to probe the membrane, tau was only detected in fractions 17 and 18 of the seeded preparation. In those fractions, monomer, dimer/trimer and tetramer were detected. This replicated the results of the previous 2N3R seeding experiment (Figure 3.8). It should be noted that the Western blots displayed in Figures 3.10 and 3.11 both suffered from missing fraction 19. Later we performed an alignment experiment to determine a volume correction, applied to align the reported volume at the MALS flow cell with the volume at the fraction collector. In future experiments using the same instrument setup, the following calculations will allow conversion between volumes at the SEC in-line 280 nm absorbance detector, $V_{SEC,}$ the corrected volume at the MALS detector $V_{MALS,\ norm}$, and the correct fraction, F_{norm}.

$$V_{SEC} + \Delta V_{MALS} = V_{MALS,norm}$$

The MALS delay volume, ΔV_{MALS}, is established during detector normalization by aligning the BSA peak volume at the in-line 280 nm absorbance detector with the light scattering peak volume at the in-line MALS detector array. In practice, it is necessary that these two detection points are separated by some length of chromatography tubing. This results in an inherent amount of uncertainty in ΔV_{MALS}. The volume is always recorded by the DAWN DSP MALS instrument as volume slice increments due to the digital-analog conversion required to interface with the AKTA FPLC.

Table 3.3 SEC-MALS comparison of seeded and unseeded 2N3R Tau.

The molecular weight data of 2N3R Tau prepared with or without non-crosslinked 2N4R Tau oligomer seeds, data from Figure 3.7.

Preparation	Molecular weight (kDa)
2N3R (+)seed - HMW	280
2N3R (+)seed - LMW	135
2N3R (-)seed - HMW	272
2N3R (-)seed - LMW	142

Figure 3.7 Characterization of 2N3R Tau monomer seeded with 2N4R Tau oligomer.

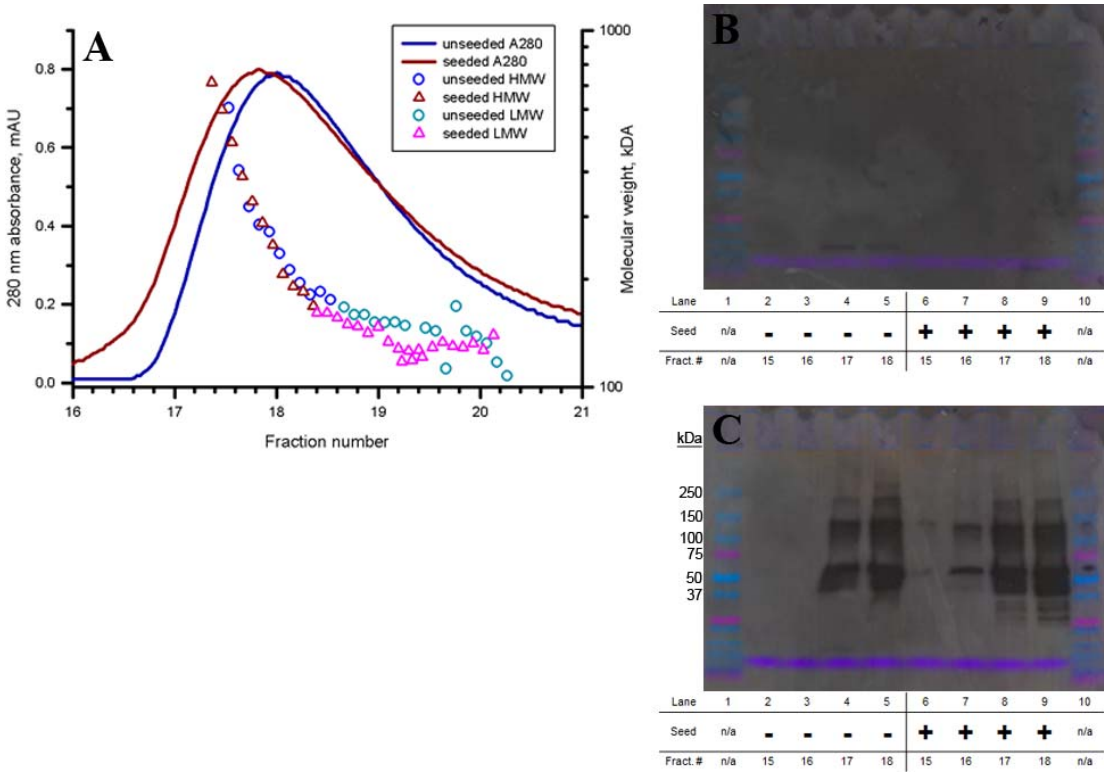

(A) Unseeded 2N3R vs Seeded 2N3R SEC-MALS analysis. The aliquot to be seeded was pre-stirred at 25 ºC for 24 h, prior to addition of 7 µL 2N4R Tau seed. Then both seeded and unseeded preparations were incubated at 25 ºC with orbital shaking. The unseeded preparation was centrifuged at 18,000 x g for 10 min and immediately analyzed with SEC-MALS. The seeded preparation remained on the bench-top at 25 ºC for approximately 1 h until elution of the unseeded preparation had completed, then it too was centrifuged at 18,000 x g for 10 min and immediately analyzed with SEC-MALS. (B) T22 and (C) Tau-5 antibody stained Western blots of fractions collected from the elutions in panel A. Membrane was first probed with T22 antibody, then chemically stripped, and re-probed with Tau-5 antibody. The gel and developed film were scanned at the same resolution then overlaid in Adobe Photoshop. The gel layer was placed on top with the *color* blend mode selected, and a +50 saturation adjustment layer applied. This allowed visualization of the molecular weight marker bands without modification of the luminosity values of the film layer.

Table 3.4 SEC-MALS comparison of seeded and unseeded 2N3R Tau.

The molecular weight data of 2N3R Tau prepared with or without non-crosslinked 2N4R Tau oligomer seeds, data from Figure 3.8 (below).

Preparation	Molecular weight (kDa)
2N3R (+)seed - HMW	117
2N3R (+)seed - LMW	62
2N3R (-)seed - HMW	93
2N3R (-)seed - LMW	62

Figure 3.8 Characterization of 2N3R Tau monomer seeded with 2N4R Tau oligomer.

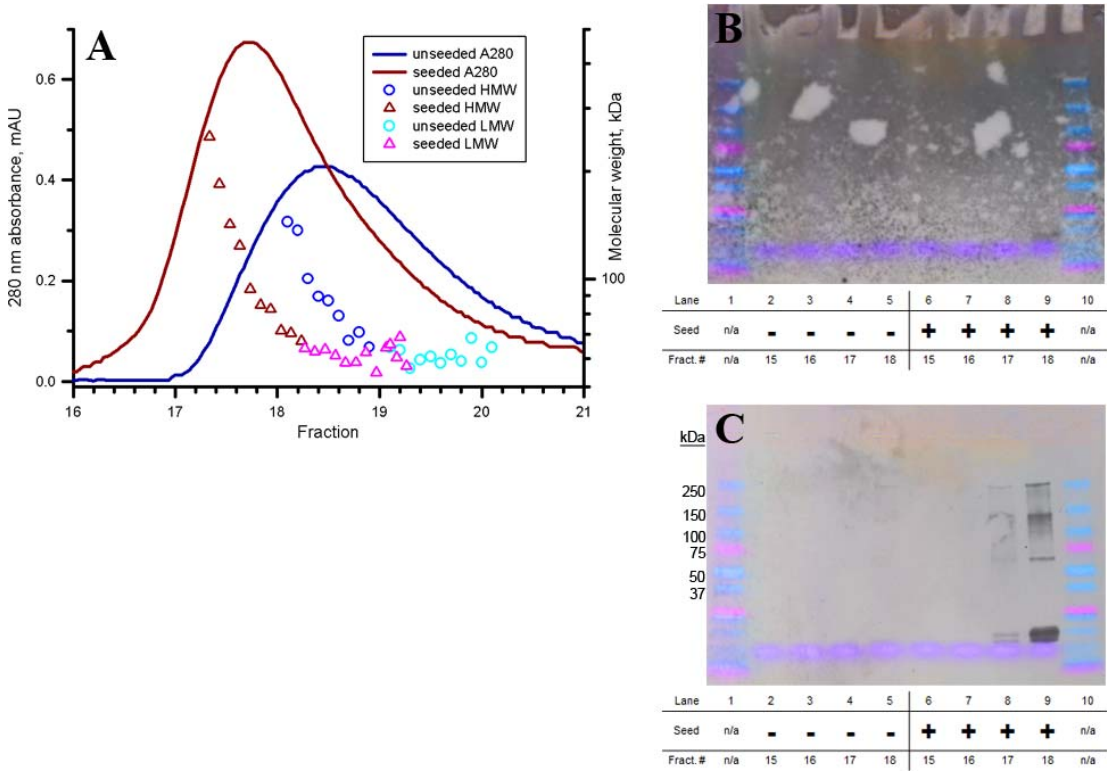

(A) Unseeded 2N3R vs Seeded 2N3R SEC-MALS analysis. A single 1 mL aliquot was centrifuged at 17,000 x g for 10 min. The supernatant was removed and split into two 500 µL half-aliquots prior to addition of 7 µL 2N4R Tau seed. Seed or vehicle was added, and both halves were incubated at 4 ºC overnight. The seeded half was incubated at 25 ºC with orbital shaking for 2h, then centrifuged at 18,000 x g for 10 min and immediately analyzed with SEC-MALS. The unseeded half was maintained at 4 ºC for approximately 1 h until elution of the unseeded preparation had completed, then it to was centrifuged at 18,000 x g for 10 min and immediately analyzed with SEC-MALS. (B) T22 and (C) Tau-5 antibody stained Western blots of fractions collected from the elutions in panel A. Membrane was first probed with Tau-5 antibody, then chemically stripped, and re-probed with T22 antibody. The gel and developed film were scanned at the same resolution then overlaid in Adobe Photoshop. The gel layer was placed on top with the *color* blend mode selected, and a +50 saturation adjustment layer applied. This allowed visualization of the molecular weight marker bands without modification of the luminosity values of the film layer.

Table 3.5 2N3R seeded oligomerization reactions preparation protocol comparison.

The 2N3R seeded vs unseeded comparisons displayed in Figures 3.7 and 3.8 were prepared in a similar fashion, but there were key differences. The preparation methods are summarized below stepwise with key differences noted.

Figure 3.7	Step	Figure 3.8
Thawed	-1	--
Pre-stirred for 24 h.	0	Thawed
No centrifugation after pre-stir.	1	Centrifuged – visible pellet.
Began with two aliquots.	2	Split single aliquot.
Added seed or vehicle.	2a	Added seed or vehicle.
Did not incubate overnight.	3	Incubated overnight at 4C.
Both aliquots were shaken on orbital shaker for 2 h.	4	Only seeded aliquot was shaken; unseeded remained at 4 ºC.
Centrifuged unseeded, injected.	5	Centrifuged seeded, injected.
Waited 1 h.	6	Waited 1 h.
Centrifuged seeded, injected.	7	Centrifuged unseeded, injected.

3.4 Results discussion.

Over the course of the project, we began to turn more attention to seeded 2N3R oligomerizations. There were multiple reasons. 2N3R is known to be less fibrillogenic than 2N4R, which provides both challenges and opportunities. Our collaborators had not yet explored seeded oligomerization of 2N3R isoform, and there is a lot of room for novel research. Challenging in that the slower kinetics may preclude detection of the expected endpoint without adjusting the experiment timescale, or the reaction system could be dominated by different pathways which were eclipsed by the rapid kinetics of 2N4R seeded oligomerization. Indeed, the 2N3R isoform may not physically be a valid target for templating by the specific seeds we applied. Finally, practical considerations played a significant role. The 2N3R aliquots we received were larger, and therefore we had more flexibility in our experimental approach.

A large amount of the time and resources dedicated to this project went to method transfer and development. Eventually refined my experimental approach enough to detect some interesting phenomena. It appears that 2N4R tau oligomeric seeds may induce a conformational change in 2N3R tau. The evidence for this is the different rates of SEC elution for species with the same molecular weight, as determined via inline MALS measurement. Another important observation was the lack of binding detected between the tau oligomer-specific antibody T22 and low molecular weight 2N3R tau oligomers. In our hands, T22 could not bind 2N3R oligomers to an extent detectable with Western blotting. T22 is a polyclonal antibody raised in mouse against aggregates generated from 2N4R. There are two possible explanations for the lack of binding. 2N3R oligomers could have a fundamentally different fold unrecognized by T22, or the conformational

epitope recognized by T22 involves the second repeat region of the tau protein, which is not present in the 2N3R isoform.

In all, I overcame multiple technical hurdles, and generated what I believe to be 2N3R oligomers via templated seeding with 2N4R preformed seeds. SDS-PAGE revealed a significant band of SDS-resistant oligomer at approximately 120 kDa, consistent with the 2N4R oligomers reported by the Kayed Lab. I also noted differences between seeded and unseeded elution rates which, when combined with MALS, may indicate conformational changes.

This project is by no means complete, but the work described above should provide an excellent groundwork for rapid progress in the future. The first objective should be transfer of the SEC purification to a column better suited to resolve molecular weights of 50 kDa and above. Felicitously, the Nichols Lab has recently acquired a column with a much greater molecular weight range, which is quite suitable for this task. The seeded 2N3R tau experiment described in Figure 3.8 should be repeated on the new column, to confirm or reject the apparent conformational change detected. The experiments should be performed with full volume samples; another issue encountered in this project was the low purification yield. This often led to difficulties for additional analysis of the purified fractions. A conformational change may be detectable by dye binding such as bis-ANS for hydrophobic surface exposure, or ThT for β-sheet structure. Circular dichroism can also provide secondary structural information.

3.5 Technical discussion.

3.5.1 Protein concentration determination.

A 2N4R pellet, generated as described in (Margittai et al. 2004) was dissolved in 30 µL 8 M Urea, diluted with 1X PBS (pH 7.4), and dialyzed overnight at 4 ºC against 1X PBS (pH 7.4). After dialysis, the sample concentration was determined by BCA assay and absorbance at 280 nm (concentration determinations are summarized in Table 3.1), and then stored at -20 ºC. There was a large difference between the results of the two assays used to assess concentration: 0.316 mg/mL per the BCA assay, and 1.27 mg/mL per the 280 nm absorbance assay.

For seeding, the sample was thawed, and centrifuged for 10 min at 18,000 x g, which yielded a small pellet. Therefore, the concentration determinations were then performed again. Both assays were repeated. This time, the BCA result was 0.316 mg/mL, and the UV absorbance was 1.14 mg/ml. This confirmed my earlier results, and because the values were slightly lower, indicated the presence of some amount of Urea-resistant material in the pellet. Ultimately, since the UV absorbance reading was within the literature range of 1-3 mg tau per pellet (Margittai et al. 2004), I used the post-spin value 1.14 mg/mL for further dilution calculations.

The BCA assay is a colorimetric method involving two reactions: first, Cu^{2+} provided by copper sulfate is reduced to Cu^{+} by protein in the sample, then Bicinchoninic acid chelates the Cu^{+} at a 2:1 ratio. This chelation complex is purple in color and has a strong absorption at 562 nm. The analyte is measured along-side a standard curve of known concentrations, to calculate a close approximation of the analyte concentration. The standard most commonly used in this procedure is BSA, a globular protein

comprised of 607 amino acids, weighing 66.5 kDa. The primary effector of Cu^{2+} reduction is the peptide bond itself. This has implications for the importance of amino acid composition of the analyte compared to the standard.

The peptide bond density for 1 mg of each protein can be calculated from the amino acid count and molecular weight. For BSA this is 5.49×10^{18} peptide bonds per mg, while for 2N4R tau, it is 5.78×10^{18} peptide bonds per mg, a ~5% higher density. All other things being equal, this would lead to an overestimation of tau concentration. Since dissolving the pellets as described in the literature source into 1 mL buffer would yield a solution with ≥ 1 mg/mL tau protein, this could not explain the low BCA assay result of 0.316 mg.

The peptide bond is not the only part of protein involved in Cu^{2+} reduction. Certain amino acid side-chains are also capable of performing this chemistry. Those include cysteine, tyrosine and tryptophan (Pierce Protein Assay Handbook). ProtParam (www.expasy.org) was used to rapidly tally their content in BSA and 2N4R tau. BSA has a total of 69 of these residues; 2N4R tau has only 7. This difference could lead to underestimation of the sample protein concentration. However, because the question now required considerations of the kinetics of reactions at each of the different residues, as well as their solvent accessibility, which was not information readily available to me, this line of investigation was left incomplete.

Another potential source of variation is incompatible components in the buffer system, particularly reducing agents, which can also interact with Cu^{2+}. The recombinant tau protein pellets were stored in a 5 mM DTT solution (see methods). However, while DTT is a potent reducing agent, the amount in the storage solution should be low enough

that there is not significant interference ((Pierce protein assay handbook)Pierce protein assay handbook). Furthermore, the dialysis step is performed specifically to obviate these issues.

Next I turned our attention to the UV/Vis concentration determination. I noted that in its oxidized form, DTT absorbs strongly in the UV, with a local absorbance maximum around 280 nm (Cleland 1964). Others have noted that high enough concentrations of DTT will interfere with UV absorbance determinations of protein concentration (Stoscheck 1990), but again, due to the dialysis step, this was not a concern.

My investigation into possible confounding factors related to the methods left me without a conclusive explanation for the differences in their outcomes. I noted possible sources of variation in the BCA assay, relating to differences between the sample and standard proteins, but could not draw conclusions without significantly more inquiry on that subject. The UV absorbance measurement did not appear influenced by the presence of DTT. Because the UV absorbance measurement of 1.27 mg/mL agreed with the expected concentration range from the literature, 1-3 mg/mL (Margittai et al. 2004), I decided to use that value in planning our next steps. It appears now that I selected the wrong assay.

In the case of the first 2N4R pellet, if instead of using the UV absorbance concentration determination, I used the BCA result, the injected mass onto the SEC column becomes 95 µg, and the recovery rises to 43%, which is comparable to the recoveries often seen when purifying Aβ with the same column and settings.

3.5.2 Sample preparation.

I drew some conclusions about the sample preparations and methods from these earliest studies of tau. Some of the pellet material did not go into solution, even after overnight incubation in 8M Urea. This could be due to the presence of insoluble, resistant fibrillar species, or simpler sources, such as insufficient denaturant, insufficient incubation time or lack of agitation during incubation. Future experiments would incorporate this knowledge to maximize the amount of material for seeding in the monomer pool.

The major problem encountered in the first experiment with 2N4R, and confirmed in following experiments, was the large discrepancy between the two assays we used to assess protein concentration. I decided to rely on the BCA assay for that determination in the future, since the concentration measured by that method made sense based on the SEC protein recovery. It now appears plausible that the preparation of the 2N4R tau pellets deviated in some fashion from the published method (Margittai et al. 2004). The published method called for precipitation of recombinant tau from the running buffer used in the final purification step- elution on a SEC column. It appears the pellets received were aliquoted at that point, prior to precipitation, so that reconstitution of a pellet in 1 mL sample buffer would yield a tau concentration near 300 μg/mL, convenient for addition of seed to initiate the oligomerization reaction. However, I consider this to be a limitation, as it would be preferable to compare seeded preparations with unseeded preparations taken from the same reconstituted pellet solution. This would eliminate the any potential error due to variations in the reconstitution procedure, or indeed the pellet source.

The cause of the misleading UV absorbance-based concentration determination, it seems, was DTT remaining in the sample solution post-dialysis. In the future, I would increase the duration of dialysis, and add a buffer change step, however DTT would consistently still elute at detectable levels. Eventually I therefore ran a control experiment which provided evidence that it was not interfering to a detectable extent with our aggregation reactions (Figure 3.3B).

3.5.3 Preformed aggregates.

Another pernicious issue I encountered was the repeated presence of "void shoulder" peaks such as those described in Figure 3.8. And more broadly, the presence of pre-formed, Urea resistant aggregates in the monomer solutions. Preformed aggregates are present even in commercially available synthetic protein, and are of special concern in the study of amyloid aggregation (Stine et al. 2003). I have experienced this issue previously in the Nichols Lab. Chapter 4 of this dissertation describes the characterization of protofibrils formed from Aβ42/Aβ40 mixtures. Concerns over preformed aggregates led to a significant amount of additional work. As part of that process, I found that even when I eluted synthetic Aβ42 under denaturing conditions, a sizable amount of resistant aggregated material remained. For the project described in this chapter, pre-formed aggregates were obviously a large concern. My goal was to observe seeded oligomerization under controlled conditions. Without monomer solutions highly purified of existing aggregates, oligomerization initiated due to added seeds could be obscured by seeding initiated due to template-competent species already present. It was not until very late in the project that I devised methods which removed enough

aggregate from the unseeded preparations to detect differences between seeded and unseeded solutions.

3.5.4 Care and maintenance of MALS instrumentation

The MALS detector normalization process should be performed regularly, since the condition of the flow cell will change with time, even when the most fastidious care and maintenance schedules are observed, such as storage in pure organic solvent, and frequent cleaning. Even with frequent flow-through of cleaning solutions such as dilute nitric acid, or detergents specifically designed for removal of protein from quartz optics, microscopic bubbles or even resistant deposits can arise which alter the scattering of light among the detectors. Detectors should *always* be normalized after the cell is removed for the most thorough available cleaning procedures. Though removing and cleaning the flow cell by hand is delicate, time consuming work, it occasionally becomes necessary. Even if the cell is removed and cleaned before each measurement (a risky proposition, as it contains multiple small, high-precision, i.e. expensive, components), there remains the possibility that slight changes in alignment of the cell with the incident light beam will alter scattering. Finally, changes in the sample buffer system should also always be accompanied by a new normalization, as different buffers will change the light scattering pattern as well. One recommendation arising from this project was regular normalization checks with an additional molecular weight standard. Such practices can also be informative when dealing with unknown, complex sample systems such as amyloid aggregates.

CHAPTER 4. LARGE SOLUBLE Aβ OLIGOMERS.

4.1 Introduction.

4.1.1 Aβ aggregation, and aggregate pathologies.

The classic Amyloid Cascade Hypothesis, which focused on insoluble Aβ deposits, could not explain many aspects of AD pathogenesis. Yet, despite this failing, over the years a large and difficult to refute body of evidence still identified Aβ with AD pathology. For example, consider again trisomy 21, or Down's Syndrome. Individuals with trisomy 21 have three copies of chromosome 21, and they invariably develop AD. This is thought to be the result of an extra copy of the APP gene, which resides on chromosome 21. In 1998 Prasher, *et al*. (Prasher et al. 1998) related the case study of a 78-year-old woman with a rare variant of Down's Syndrome with only partial trisomy-21. The break was positioned such that the third chromosome 21 copy lacked the APP gene. Thus, the woman possessed the normal gene dosage for APP, yet still presented much of the Down's Syndrome phenotype. The reader will no doubt immediately recognize that this woman represents, in some sense, a negative-control for AD dependence on APP gene dosage in humans. Indeed, for the five years prior to her death at age 78, neuropsychological evaluations of this incredible individual reported no signs

of decline in memory, attentiveness, language, cognition or adaptive skills. MRI six months before her death revealed no evidence of AD-related cerebral or lobar atrophy of the brain. Upon her death, post-mortem investigation concluded that AD neuropathology was *absent*. No AD-related damage was apparent in her brain, and histological staining revealed no presence of Aβ or tau deposits. Because of this and numerous other lines of evidence, Aβ remains the target of a large amount of research. Many have turned to exploration of the behaviors of soluble oligomeric assemblies *in vivo* and *in vitro*.

Excluding the insoluble fibril, Aβ exists as polydisperse soluble aggregates, including monomer; a number of oligomers; protofibrils which could be characterized as HMW oligomers, but possess characteristic fibril-like properties; and protofilaments, which are still soluble, but possess yet more fibril-like properties (Mizuno 2012, Nichols et al. 2015). Aβ aggregation, like all amyloid aggregation, proceeds via a nucleated, crystallization-like process. Initially during the lag phase, the population is primarily monomeric. Eventually the unstructured or weakly α-helical (Bartolini et al. 2007) monomers undergo spontaneous conformational change and non-covalent interactions occur between monomers (Jarrett et al. 1993), forming oligomeric seeds. Some studies have linked this stage with a transient increase in α-helical structure detectable by circular dichroism (Walsh et al. 1997, Kirkitadze et al. 2001). This marks the beginning of the elongation phase, during which β-sheet content increases as aggregates grow larger. At the plateau phase, when the monomer is sufficiently depleted, β-sheet dominates the secondary structural content.

The pathology of Alzheimer's disease (AD) is complex. Activities vary by aggregation state, and pathogenesis likely includes a direct neuronal toxicity axis, as well

as an indirect axis of neuronal toxicity mediated by neuroinflammation. Oddly enough, wild-type monomeric Aβ42 may function in a neuroprotective capacity, supporting developing neurons under nutritional deprivation conditions, and protecting mature neurons from excitotoxic stress (Giuffrida et al. 2009). LMW oligomeric Aβ species (dimers or trimers) localize at, and insert into, the neuronal lysosomal membrane, possibly inducing membrane labilization and related cytotoxicity (Liu et al. 2010). Dimeric Aβ directly induces hyperphosphorylation of tau protein resulting in cytoskeletal microtubule degradation and neuritic dystrophy (Jin et al. 2011). A 56 kDa dodecamer (Aβ*56) is detectable in human AD brain. In a mouse model of AD, extracellular accumulation of Aβ*56 in aged animals, or injection into young animals, causes memory deficits in a cell-death independent fashion (Lesne et al. 2006). Interaction between the plasma membrane and extracellular spherical oligomeric species (diameter 2-5 nm, MW ≈ 90 kDa, ~24 monomer subunits), but not LMW oligomers or fibrils, causes an increase in ion permeability (Kayed et al. 2004). Neuronal cell studies have demonstrated disruption of Ca^{2+} homeostasis in this manner (Demuro et al. 2005), which is a well-characterized apoptotic trigger (Berridge et al. 1998), and induces increased *cellular production* of additional Aβ42 (Pierrot et al. 2004). These very same spherical oligomers, but not LMW oligomers or fibrils, also cross-seed aggregation of tau into a neurotoxic tau oligomer (trimer) capable of seeding additional tau oligomerization (Lasagna-Reeves et al. 2010). Protofibrils are essentially non-toxic to microglia (Paranjape et al. 2012) and neuronal cells (Nichols, M. R. and Colvin, B. A., unpublished data), however they elicit large inflammatory responses from glial cells (Paranjape et al. 2012). In summary,

soluble Aβ species mediate a range of deleterious effects including disruption of homeostasis, cell trafficking, and inflammation.

Synthetic Aβ peptides have been an indispensable tool for *in vitro* studies establishing the kinetics and biophysics of amyloid aggregation. Allowing researchers to recapitulate Aβ fibrillogenesis in controlled conditions, *in vitro* studies have led to the development of the crystal-like nucleated three phase model of amyloid aggregation described above. Control of nucleation, rate of elongation, and formation of specific oligomers can be ascribed to multiple factors, including pH, ionic strength, temperature and agitation (Lambert et al. 1998, Harper et al. 1999, Nichols et al. 2002, Chromy et al. 2003, Stine et al. 2003), not to mention seeding with pre-formed aggregates, such as what is described above for tau protein (Wu et al. 2010).

It is well established that Aβ is generated by sequential cleavage of APP by β-secretase followed by γ-secretase (De Strooper et al. 2010) resulting in isoforms 37 to 43 amino acids in length (Selkoe 2004). The two most common isoforms are Aβ42 and Aβ40, with Aβ40 the most common (Selkoe 2000). Both of these are found in circulation as well as in the cerebrospinal fluid (Hansson et al. 2010). The sequence difference between the two is small, with Aβ42 possessing a pair of C-terminal hydrophobic residues absent in Aβ40, yet there are profound biophysical properties between the two. Aβ42 is well established as far more prone to aggregation into fibrils (Jarrett et al. 1993). These differences seem linked to AD pathology. As stated previously, all mutations leading to EOAD do one of two things: they either increase overall Aβ production, or enhance production of Aβ42 over Aβ40 (Hardy 1997, Selkoe 2001). Furthermore, although Aβ40 is more common in circulation, it is Aβ42 which primarily comprises the

core of the senile plaques found in AD brain (Gravina et al. 1995). Further mouse model and cell culture studies support the idea that the Aβ42/Aβ40 ratio, and not overall Aβ level, drives AD pathology (Scheuner et al. 1996, Bentahir et al. 2006, Deng et al. 2006, Kim et al. 2007).

Despite the likely importance of the Aβ42/Aβ40 ratio in AD etiopathogenesis, surprisingly little work has been done in the field of amyloid aggregation which utilized mixtures of the two isoforms. Jan, *et al.* (Jan et al. 2008) reported that monomeric Aβ40 inhibited fibril formation from Aβ42 monomers and protofibrils. Shorter lag times/faster aggregation rates have also been reported as the Aβ42/Aβ40 ratio increases (Yan et al. 2007, Kuperstein et al. 2010). Two mechanisms have been posited to mediate this effect. Aβ40 may act as "caps" on Aβ42 aggregates, preventing elongation (Yan et al. 2007). Alternatively, Aβ40 may slow the rate of Aβ42 aggregation by so-called "non-productive" interactions (Pauwels et al. 2012).

Understanding the kinetics of amyloid aggregation, as well as the effects that solution conditions have on aggregation pathways will grant researchers greater control over *in vitro* studies, and enhance interpretation of *in vivo* findings. This is one of the major research goals of the Nichols Lab. The studies described below resulted in contributions to a pair of published journal articles (Nichols et al. 2015, Terrill-Usery et al. 2016). In Nichols et al. 2015, the subject of interest was a comparison of different HMW soluble aggregates of Aβ42. Terrill-Usery et al. 2016, on the other hand, was focused on co-aggregation of the Aβ42 and Aβ40 isoforms. What both projects had in common was the need to develop a new experimental paradigm. amyloids are well known for their ability to undergo templated conformational change mediated by pre-

formed seeds. It became apparent that projects would greatly benefit if the starting solutions were pure monomeric solutions, something rarely done in the field due to the increased costs and complexity of experimental design.

The work began with development of new methods for generating populations of high molecular weight soluble oligomers from SEC-purified monomer. Using the new methods, buffer- and temperature- dependence of aggregation was investigated. This groundwork was then leveraged to improve the analysis of protofibril formation in Aβ42/Aβ40 mixed solutions. Throughout both projects I made heavy use of multiple classic techniques for the study of amyloid aggregation, including SEC-MALS, CD spectrophotometry, dye binding and TEM imaging.

4.2 Results.

4.2.1 Influence of buffer on purified Aβ42 monomer aggregation.

The monomer fraction enrichment preparation was used to generate stock solutions for these studies (see methods). Synthetic Aβ42 was reconstituted with 10 mM NH_4OH in 6 M GuHCl, an alkaline, chaotropic solution which restricts the extent of rapid aggregation, thus increasing the monomer yield upon SEC purification. After centrifugation at 18,000 x g for 10 min and purification, monomer fractions were placed on ice. Purified monomer was then diluted to 40 μM for the aggregation reactions. Amyloid aggregation is well known for sensitivity to solution conditions such as ionic strength, or pH, therefore elutions and aggregation reactions were performed under multiple buffer conditions to examine their varying effects. Reactions were performed in siliconized tubes to prevent adsorption, at 37 ºC in a water bath with a flotation pad. At certain time points aliquots were removed from the reactions for ThT measurement. This would allow estimates of lag phase duration. Purified monomer did not bind ThT (Figure 4.1A), and upon immediate repurification under the same conditions there was no material in the void volume (Figure 4.1B). Figure 4.1A gives the endpoint total ThT fluorescence and supernatant ThT fluorescence after centrifugation for 10 min at 18,000 x g for three buffer conditions. Figure 4.1B is the corresponding repurification SEC profiles of the supernatants. Two conditions demonstrated significant void volume peaks upon post-incubation repurification. In-line MALS analysis of those samples is presented

in Figure 4.1C and 4.1D. Their peak void volume contents were also visualized with TEM, and representative images are shown in Figure 4.3E and 4.3F.

The aggregation reaction carried out in aCSF (pH 7.8) at 37 ºC had a lag phase > 4 h, but aggregated rapidly upon longer incubation (21 h). The endpoint ThT fluorescence was absent in the supernatant post-centrifugation (Figure 4.1A). Minimal material was found in the void or included peaks after SEC repurification of the supernatant. This indicates that between 4 and 21 h aggregation proceeded rapidly to insoluble fibril formation under the applied reaction conditions.

Increased ionic strength enhances aggregation and fibrillization (Nichols et al. 2002), therefore an aCSF (pH 7.8) with NaCl concentration reduced from 130 mM to 30 mM (low salt aCSF) was prepared and used to perform another aggregation reaction as described above. In this case the lag phase was likely longer (> 8 h). After 25 h incubation, there was significant ThT fluorescence, and ~90% remained in the supernatant after centrifugation, indicating soluble aggregates with significant β-sheet structure (Figure 4.1A). There was a large SEC void volume upon SEC repurification (Figure 4.1B).

A commonly utilized buffer for Aβ studies is Tris-HCl (Walsh et al. 1997, Walsh et al. 1999, Nichols et al. 2002), which was used here to compare with aggregation in aCSF-based buffers. After overnight incubation at 37 ºC, only 9% of the ThT fluorescence remained in the supernatant (Figure 4.1A), and both SEC void and included peak sizes were reduced compared to the low salt aCSF preparation (Figure 4.1B), however enough material remained for comparison with the in-line MALS results of the low salt aCSF sample (Figure 4.1C and 4.1D).

The low salt aCSF-formed aggregates had a molecular weight range between 3394 and 2961 kDa, with a mean of 3044 kDa, or approximately 674 Aβ42 monomers. The Tris-HCl-formed aggregates had a significantly lower molecular weight, which ranged from 2133 to 1386 kDa, with a mean of 1533 kDa, or approximately 340 monomers. The lower molecular weight measured in the Tris-HCl sample was not expected, considering the larger amount of insoluble fibril material, based on pre-/post-centrifugation ThT fluorescence measurements (Figure 4.1A). Measured R_g values agreed with M_w values. The low salt aCSF aggregates had R_g ranging from 59 to 58 nm, with a mean of 59 nm, while the Tris-HCl aggregates had R_g ranging from 43 to 37 nm, with a mean of 39 nm.

The two preparations described above presented intriguing morphologies when imaged via TEM. The low salt aCSF preparation resulted in thin, extended (> 1 μm in length) protofilament structures (Figure 4.1E) while the Tris-HCl aggregates were classic curvilinear protofibrils, between 50 and 100 nm in length (Figure 4.1F).

Figure 4.1 Monomer aggregation reactions in varied buffer conditions.

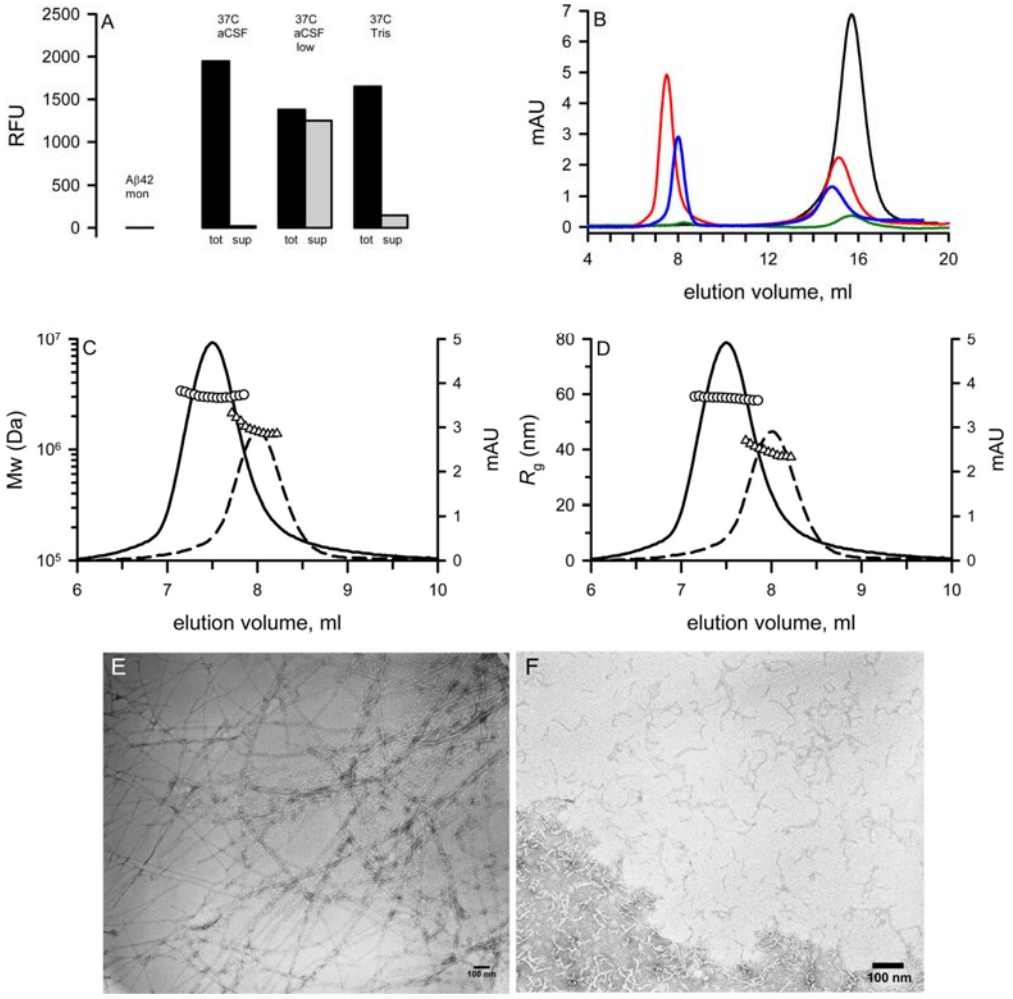

(A) Aβ42 monomers purified by SEC in different buffers were diluted to 40 μM. ThT measurements were taken of the monomer before (Aβ mon) incubation at 37 ºC. Endpoint fluorescence measurements were made at 21 h for aCSF (pH 7.8) monomers, 25 h for low salt aCSF (pH 7.8) monomers and 32 h for 50 mM Tris-HCl (pH 7.8) monomers. Total ThT measurements were made before centrifugation at 18,000 x g for 10 min, followed by supernatant ThT measurements. Results are baseline-corrected for buffer plus ThT in absence of Aβ. (B) 0.5 mL supernatants from the reactions were repurified by SEC with in-line 280 nm absorbance (mAU) quantitation. The black trace is re-injected freshly purified Aβ42 monomer in aCSF. Green is the aCSF reaction, red is the low salt aCSF reaction, and blue is the Tris-HCl reaction. (C) and (D) M_w and R_g, respectively, determined by in-line SEC-MALS of low salt aCSF (—, mAU; ○, M_w or R_g) and Tris-HCl (---, mAU; △, M_w or R_g) reactions. Every fourth MALS data point shown, for clarity. (E) TEM of low salt aCSF peak fraction at 35,000× (F) TEM of Tris-HCl peak fraction at 59,000×.

4.2.2 Influence of temperature in low ionic strength aggregations.

The low salt aCSF preparation described above was repeatable; I performed a second preparation which also generated protofilaments with characteristic long, slender morphologies and similar M_w and R_g. However, the rapid kinetics of formation obfuscated to some extent the ability to observe the smaller protofibrillar or oligomeric species which were the study target.

Therefore, additional 40 μM reactions of purified Aβ42 monomer were performed in low salt aCSF, this time at temperatures of 4 ºC and 20 ºC, to compare with the 37 ºC reaction (Figure 4.2). These aggregation reactions both proceeded much more slowly than the higher temperature, with the 20 ºC falling in-between, as expected. The reactions were monitored by ThT fluorescence through the nucleation step and into elongation (Figure 4.2A). Then the samples were centrifuged for 10 min at 18,000 x g, a final ThT measurement was performed on the supernatants, and they were subjected to analysis by SEC-MALS (Figure 4.2B and 4.2C). At both 20 ºC and 4 ºC, the majority of the ThT-positive material remained soluble (92% and 68%, respectively). The 20 ºC SEC void volume M_w and R_g profiles were 2478 to 2281 kDA (mean of 2357 kDa, estimated 522 monomer subunits), and 59 to 58 nm (mean of 59 nm). The 4 ºC SEC void volume M_w profile was 6779 to 3140 kDA (mean of 4324 kDa, estimated 958 monomer subunits), and and the R_g profile was 59 to 58 nm (mean of 58 nm). ThT fluorescence of the peak fractions (fraction 16) from the three different temperatures were very similar, and the differences correlated with the different Aβ42 concentrations of 7 μM for 37 ºC, 6 μM for 20 ºC, and 5 μM for 4 ºC (Figure 4.2D).

I utilized CD spectrometry to probe secondary structure in the regular aCSF insoluble fibrils, compared to the soluble aggregates formed in the low salt aCSF at various temperatures (Figure 4.2E). The acquired CD spectra allowed estimations of secondary structure with the CONTINLL module of the well-known CDPro software package. As expected, the Fibrils formed in full aCSF were β-sheet enriched: 8% helix, 63% sheet/turn, and 29% random coil. Interestingly, the estimated secondary structures of the low salt aCSF-formed protofilaments had significant increases in α-helix content. The 37 ºC preparation was 45% helix, 25% sheet/turn, and 30% random coil. The 20 ºC preparation was 34% helix, 34% sheet/turn, and 32% random coil. The slowest forming 4 ºC preparation was 24% helix, 54% sheet/turn, and 22% random coil. The trend appears to be decreasing helical content with decreasing temperature. However, even formed at 4º C, the low salt aCSF protofilaments contained more helical content than the 37 ºC full aCSF fibrils.

Figure 4.2 Temperature-dependent kinetics, but similar secondary structures.

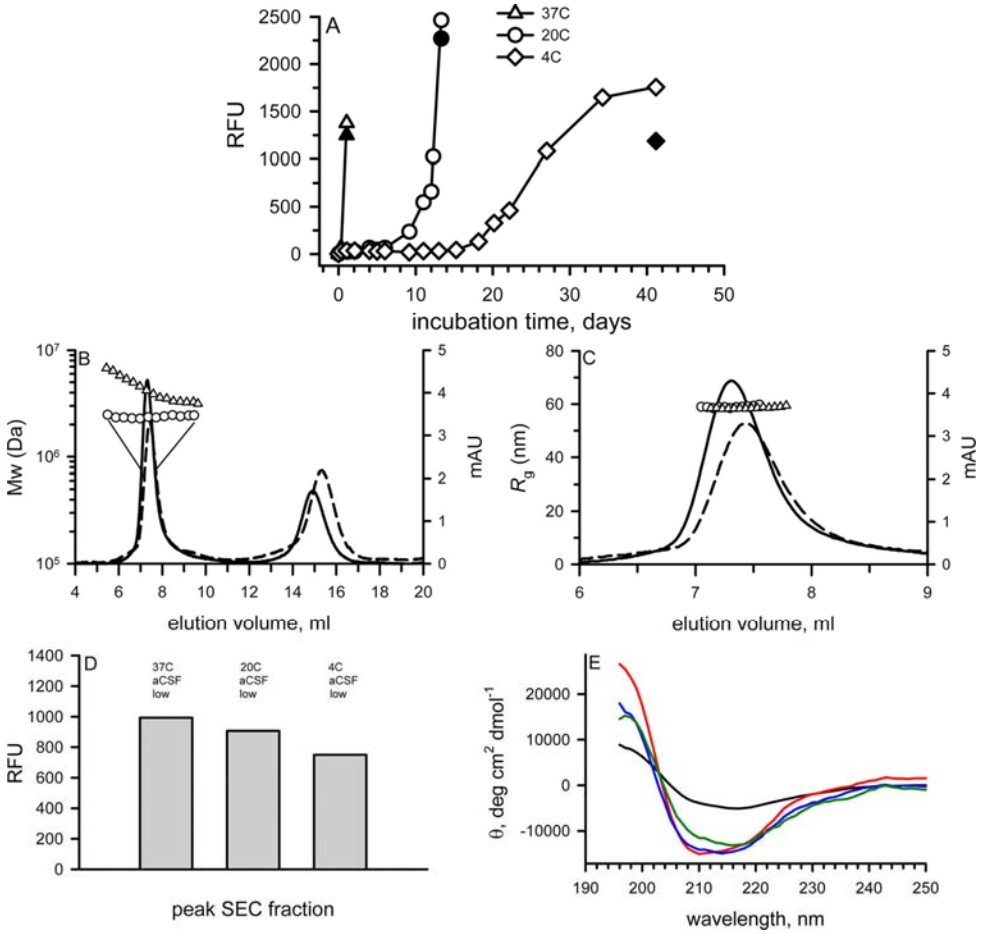

(A) ThT measurements made over time on 40 µM low salt aCSF solutions of SEC-purified Aβ42 monomers incubated at 37 ºC (△), 20 ºC (○), and 4 ºC (◇). Closed symbols mark ThT measurement of supernatant at final time point, after 10 min centrifugation at 18,000 x g. Remaining panels refer to void peak of the SEC elutions generated from these supernatants. (B) M_w and (C) R_g were determined from data collected in 0.167 mL slices from the full width at half-maximum void peak volumes of the 20 ºC (—, ○) and 4 ºC (---, ◇) reactions. (D) ThT measurements of void peaks at 7, 6, and 5 µM, for 37 ºC, 20 ºC, and 4 ºC conditions, respectively. Since concentrations were low, 10 µM ThT was mixed 1:1 with sample to enhance fluorescence. (E) CD spectra acquired from void peaks of 37 ºC (red), 20 ºC (blue), and 4 ºC (green) conditions; 7, 6, and 5 µM concentrations, respectively, were used for the mean residue ellipticity (MRE) calculations. The CD spectrum of the 37 ºC full aCSF preparation described in Figure 3.1 (black) was acquired prior to centrifugation, and 40 µM was used for MRE calculation.

4.2.3 The Aβ42/Aβ40 ratio influences rapid protofibril formation.

The new methods described above provide means to generate defined soluble aggregates from strictly monomeric starting material. This is an important new method because it avoids any effects which preformed aggregates may have upon the aggregation reaction. I used these methods to advance an earlier project initiated by Shana Terrill-Usery (Terrill-Usery et al. 2016) examining aggregation outcomes in mixed-isoform (Aβ42/Aβ40) solutions. As the Aβ42 content in the mixtures was replaced with an equimolar amount of Aβ40, the relative PF yield decreased and the monomer yield increased. An isoform-specific ELISA indicated that isoform content in the PF fractions tracked with isoform content in the starting mixtures. Equimolar (5 μM) dilutions of protofibrils formed at each Aβ42/Aβ40 ratio were tested for ability to bind ThT. The analysis revealed decreasing ThT binding fluorescence as the Aβ42/Aβ40 ratio decreased. This suggested a conformational change in the ThT binding site which either had reduced affinity for, or altered the interaction with, ThT. Below 100/100 Aβ42/Aβ40 ratio, the extent of ThT fluorescence was essentially baseline. These results imply that isoform ratio influences the extent of aggregation, aggregate secondary structure, and isoform content. As interesting as this earlier work was, a serious weakness was the use of isoform mixtures generated in HFIP **(see Methods 2.4.1 to 2.4.3)**.

As part of this project, I performed several purifications where HFIP-treated Aβ peptide was reconstituted in 6 M GuHCl with 10 mM NH4OH, to enhance monomer

yields and suppress rapid PF formation. It is well known that this monomer purification protocol does not result in complete elution of the aliquot as monomer. It simply shifts the balance, compared to the protofibril preparation, which is useful when larger monomer pools are desired for various cellular or biophysical studies. Even in the case of pure Aβ40, a much less aggregative isoform than Aβ42, material is always recovered in the void volume- approximately 7% of the overall recovery. For Aβ42 the void volume recovery is more variable, and larger, though always less than about 50%. This phenomenon was suggested as a possible confounding element in the experimental design, because these aggregates could possibly be present in the peptide film, as opposed to rapidly formed upon resuspension. An objective of this project was to probe isoform content in formed protofibrils using an Aβ C-terminal specific ELISA assay I developed specifically for this purpose. In the context of the isoform mixtures, which were originally created by mixing HFIP solutions of pure Aβ42 and pure Aβ40, if more aggregates were already present in the Aβ42 HFIP solution, then the ELISA would over-estimate the Aβ42 contribution to protofibrils formed in the mixture.

4.2.4 Aβ40 as a potential inhibitor of Aβ42 aggregation.

To investigate the possibility that Aβ40 may modulate Aβ42 aggregation, I performed additional studies where the mixtures were generated from freshly SEC-purified Aβ42 and Aβ40 monomer. HFIP-processed Aβ42 and Aβ40 dry peptide films were resuspended in 6 M GuHCl with 10 mM NH_4OH, and purified on Superdex 75 SEC column as described in the methods. Collected fractions were immediately placed on ice. Calculated contributions of Aβ42 and Aβ40 were designed so that the total Aβ concentration was 40 μM. The Aβ42 and Aβ40 monomers were purified in and diluted with the same low salt aCSF buffer (pH 7.8) described previously (30 mM NaCl as opposed to 130 mM NaCl for the full aCSF). As shown above, this preparation inhibits fibril formation, and enhances formation of protofilaments. The low salt aCSF preparation was chosen, instead of the Tris-HCl preparation also described in previous work. While the Tris-HCl preparation resulted in a population of soluble aggregates with bona-fide protofibril morphology by TEM, that population was not large; 91% of the material was insoluble fibril. This made it impractical or impossible to generate high enough concentrations at large enough volumes to be of use for comparative aggregaton studies.

The ThT binding fluorescence of these mixed SEC-monomer solutions was assessed after incubation for 24 h at 37 ºC (Figure 4.3A). Increased fluorescence correlated with increased Aβ42/Aβ40 ratio. The all Aβ42 solution exhibited the most fluorescence. The mixtures fell in line by Aβ42/Aβ40 ratio, and the all-Aβ40 solution

exhibited the least fluorescence. The relative reduction in ThT fluorescence was greatest between the all-Aβ42 solution and the 4:1 Aβ42/Aβ40 mixture. This suggested that it was the presence of the Aβ40, not the reduction in Aβ42 content, which limited the aggregation.

To test this hypothesis, I prepared a second set of SEC-purified monomer, this time using only Aβ42, at the same concentrations of Aβ42 as in the 40 μM total Aβ mixtures, but omitted the Aβ40 portion. This all-Aβ42 set had Aβ42 concentrations of 40, 32, 20, and 8 μM. The measured ThT fluorescence results from this set are shown in Figure 4.3B. The overall trend remained the same, with ThT fluorescence decreasing with decreasing Aβ42 concentrations. Importantly, however, there was a much smaller difference in the decrease between 40 and 32 μM Aβ42 preparations in the all-Aβ set the analogous preparations in the mixtures set (Figure 4.3A).

After 24 h incubation at 37 ºC and measurement of ThT fluorescence, the Aβ42/Aβ40 set preparations and the all-Aβ42 set preparations were each centrifuged at 17,000 x g for 10 min and the supernatants analyzed by SEC-MALS. Because amyloid aggregation is particularly susceptible to variability, special care was taken to create an experimental design with minimal temporal differences between the preparations. Incubations of the preparations in each set were begun on the same day, and they were analyzed the next day in the same staggered order at scheduled times to minimize the effects of instrumental and environmental changes within each set. The results of the post-incubation SEC analyses are displayed in figure 4.4.

Protofibril formation decreases with decreasing Aβ42/Aβ40 ratio. The all-Aβ40 preparation of the mixtures set was essentially monomeric; the void volume in-line 280

nm absorbance signal was at baseline, unless I squinted really-hard (Figure 4.4A). The remaining preparations show a clear trend in void volume peak size. When integrated peak recoveries are compared, this trend is amplified (Figure 4.4B). By contrast, the all-Aβ42 set follows no such clear trend, with relative PF recoveries greater even in the low concentration 8 μM preparation (Figure 4.4C and 4.4D).

Figure 4.3 ThT fluorescence in Aβ monomer solutions is influenced by Aβ40 content.

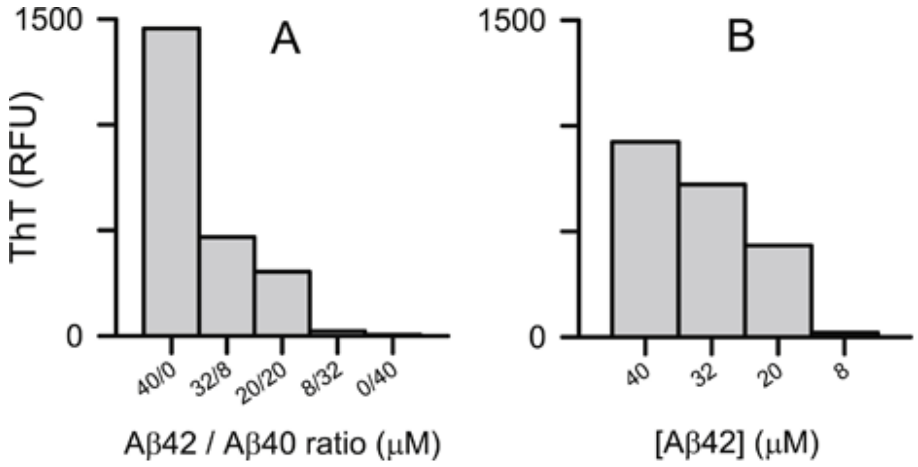

Solutions of Aβ42 with (A) or without (B) Aβ40 were incubated for 24 h at 37 ºC. Aliquots taken from the samples were diluted 1:10 in 5 μM ThT, and fluorescence measurements were made.

Figure 4.4 Effect of Aβ42 concentration when Aβ40 is absent.

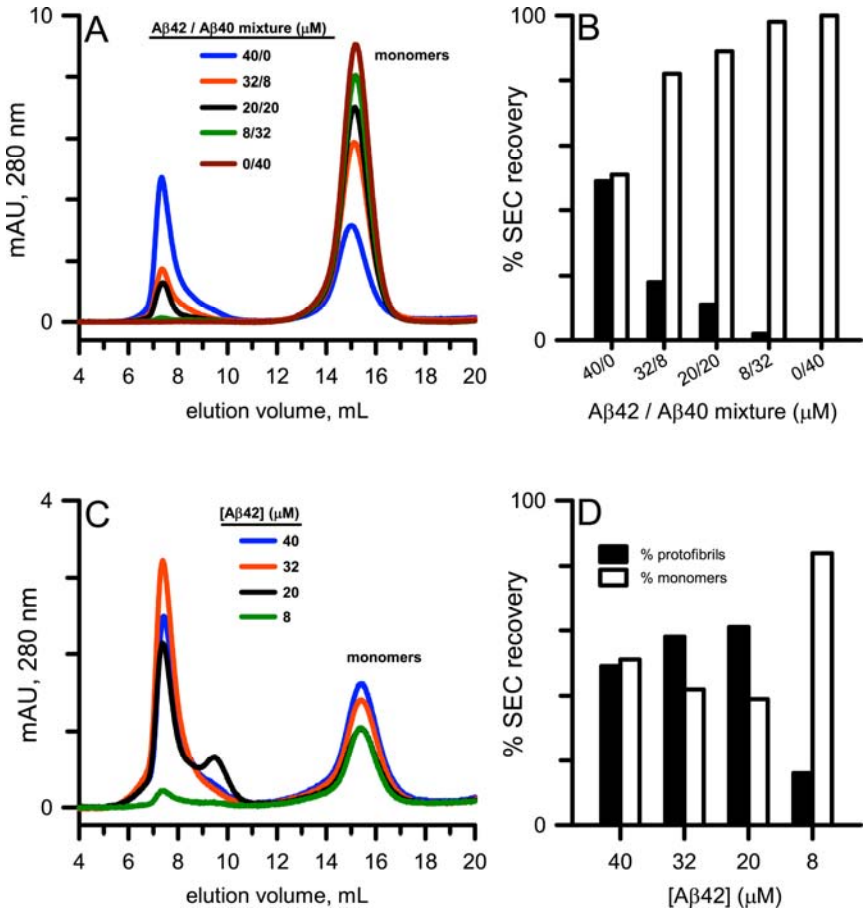

(A) SEC-purified monomer solutions of Aβ42 and Aβ40 were combined to a total of 40 μM Aβ. Mixtures were incubated at 37 ºC for 24 h, then centrifuged for 10 min at 18,000 x g and supernatants fractionated by SEC. (B) Amount of recovered material in protofibril and monomer peaks from panel A, as a percentage of total recovery. (C) SEC-purified monomer solutions of Aβ42 prepared at the same Aβ42 concentrations as in panel A, but without any Aβ40. Incubation and analysis was the same as in panel A. (D) Analogous to panel B, for panel C.

4.2.5 Subtle inhibitory effect of Aβ40 on Aβ42 conversion to protofibril.

Light scattering data from all preparations was recorded in-line with SEC fractionation. Detection of scatterers in the void volume was possible for ≥ 20 μM Aβ42 preparations. For the remaining preparations, the signals were insufficient for reliable determination of molecular weight. Results from the ≥ 20 μM Aβ42 preparations are given in Figure 4.5A. The all-Aβ42 preparations demonstrated some degree of increased polydispersity across their void volume peaks, and the molecular weights were slightly increased, compared to the Aβ42/Aβ40 mixture set (Table 4.1). The differences may be evidence that the all-Aβ preparations experienced faster aggregation, since the process is inherently a stochastic one. However, the small number of samples in this case limits the usefulness of such interpretations.

A small perturbative effect associated with the presence of Aβ40 was more clearly revealed when we probed ensemble secondary structural content in the preparations with ≥ 20μM Aβ42 preparations by CD spectrophotometry (Figure 4.5B). The mixtures (32/8 and 20/20) have significant α-helical characteristic compared to the 40/0 preparation, suggesting β-sheet formation is not as extensive. This effect is also present in the all-Aβ42 32 and 20 μM preparations. Furthermore, the α-helical contribution is not as large in the absence of Aβ40, which suggests that both reduction of Aβ42 content, *and* the presence of Aβ40 both reduce the extent of aggregation.

Figure 4.5 Subtle Aβ40 effects on protofibril polydispersity and conformation.

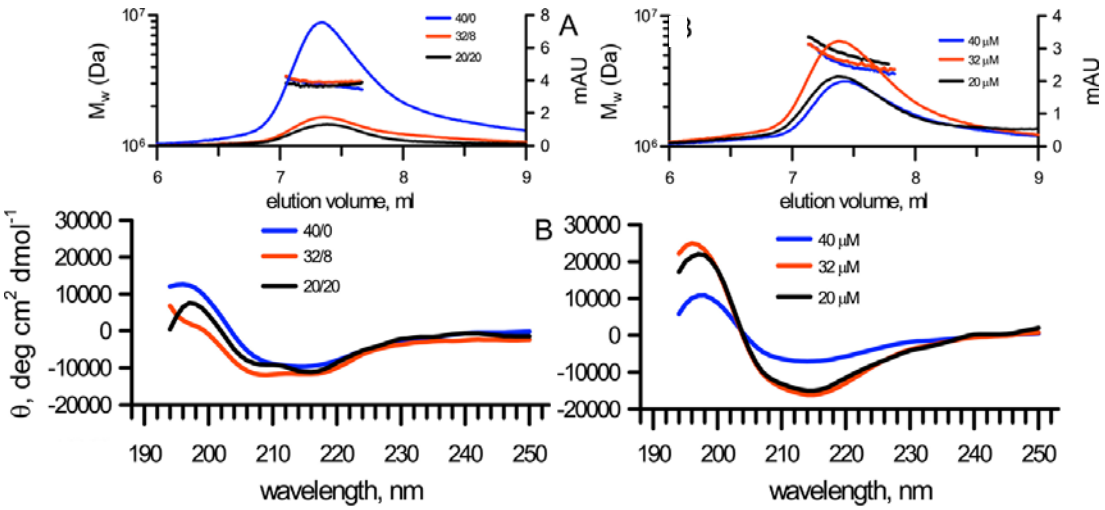

MALS (panel A) and circular dichroism (B) analysis associated with mixture sets in Figure 4.4A (left panels) and 4.4C (right panels). (A) MALS analysis of protofibril peaks performed in-line with SEC fractionation in Figure 4.4, performed as described in the methods. MALS-determined weight-averaged molecular weights (full width half max) are summarized in table 5-1. (B) Circular dichroism spectra acquired from the protofibril peak fractions collected in Figure 5-5. Reported in units of mean residue ellipticity.

Table 4.1 Summary of molecular weight data from Figure 4.5.

Results of the MALS determined molecular weight measurements in Figure 4.5 are summarized below.

Aβ42 (μM)	Aβ42 (μM)	M_w(Da)	Aβ42 (μM)	Aβ42 (μM)	M_w(Da)
40	0	2.95×10^6	40	--	4.21×10^6
32	8	3.13×10^6	32	--	4.64×10^6
20	20	2.92×10^6	20	--	5.25×10^6

4.2.6 Protofibrils formed from Aβ42/Aβ40 solution mixtures are primarily Aβ42.

A direct probe of Aβ40 content in protofibrils formed in Aβ42/Aβ40 mixtures would certainly be helpful in clarifying the interactions between the two isoforms in mixed solutions. Therefore, I developed a novel C-terminal selective ELISA assay for isoform content in protofibrils. The assay relies on capture with Ab13.1.1, which is selective for the C-terminal of Aβ40, or Ab2.1.3, which selects for Aβ42. Detection is made with HrP-conjugated Ab5, which recognizes the first 16 N-terminal amino acids on Aβ. In this experimental paradigm, a sample generated in a mixed isoform monomer solution was applied to an Ab2.1.3-coated well, and to an Ab13.1.1 coated well. The relative extent of binding was quantified via detection with Ab5; being N-terminal specific, Ab5 has equal affinity for both isoforms. The isoform-specific binding for the sample was compared to standard curves generated with single-isoform monomer solutions to regularize for differences between Ab13.1.1/Aβ40 and Ab2.1.3/Aβ42 binding affinities. I used the ELISA to directly compare Aβ42/Aβ40 content of the initial aggregation solutions and resulting protofibril peaks of the Aβ42/Aβ40 mixture set in Figure 4.5A. The results are related in Table 4.2.

The ELISA data strongly suggests that Aβ42 was strongly favored for incorporation into protofibrils. This was especially evident in the 20/20 mixture, which ELISA confirmed was near 1:1 for the two isoforms. In that case, only trace amounts of Aβ40 were detected in the protofibril peak.

Table 4.2 ELISA-determined Aβ42/Aβ40 molar ratios.

Results of the C-terminal selective ELISA determination of isoform incorporation into protofibrils formed in Aβ42/Aβ40 monomer mixtures, as described in the methods.

Aβ42/Aβ40 mixture (μM)	Aggregation solution	Protofibril peak
40/0	>10	>10
32/8	3.0 ± 0.62	>10
20/20	1.4 ± 0.19	>10
8/32	0.8 ± 0.06	ND
0/40	<0.01	ND

4.2.7 When Aβ42 concentration remains fixed, increasing Aβ40 does not strongly affect protofibril formation.

That Aβ40 incorporation into protofibrils is minimal limits the mechanisms by which it can exert an influence on the rate of protofibril formation. To examine the Aβ40-related effects while controlling for effects due to Aβ42 concentration, mixed solutions were prepared where Aβ42 was held at a constant 20 μM, and only Aβ40 was varied. The lowest Aβ42/Aβ40 ratio we could generate was 20/56. This was limited by the volume of monomeric material recoverable at a high enough concentration to make mixtures of sufficient volume for subsequent SEC-MALS analysis. Ratios of 20/40, 20/20, 20/10, and 20/0 were also examined. The mixtures were prepared and analyzed under the same protocols and with the same care as described in Section 4.3.3. The results are shown in Figure 4.6.

The monomer recovery increased with increasing Aβ40 as expected, as Aβ40 is less aggregation-prone than Aβ42 (Figure 4.6A), and this in turn affected the percent recovery ratio (Figure 4.6C). At the studied Aβ42 concentration, the effect of increasing Aβ40 concentration on the protofibril peak was minimal (Figure 4.6A and 4.6D). However, a noticeable decrease in ThT fluorescence occurred in the protofibril peak with addition of Aβ40, suggesting reduced β-sheet content (Figure 4.6E). This was corroborated with CD (Figure 4.6F), which also revealed the presence of α-helical characteristics in the protofibril peaks generated in high-Aβ40 mixtures (20/56 shown).

Figure 4.6 Weak concentration dependence of Aβ40 effects at constant Aβ42.

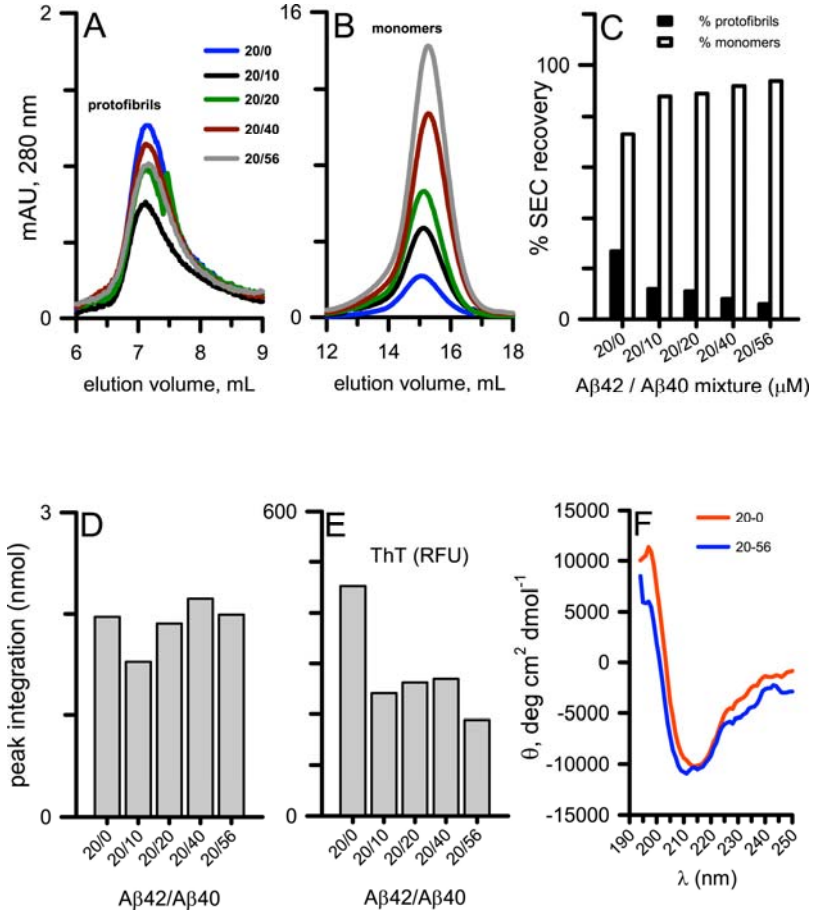

(A) and (B) Void and included peak 280 nm absorbance traces, respectively, from Aβ42/Aβ40 monomer mixtures prepared and handled in the same manner as described in Section 4.3.3, at fixed Aβ42 concentration with varying Aβ40 concentration. The legend identifies the preparations by μM Aβ42/Aβ40. (C) The relative recoveries from void and included peaks, on a molar basis. (D) Integrated peak areas from panel A. (E) ThT fluorescence of the protofibril peaks in panel A, measured as described in the methods. (F) Circular dichroism spectra, in units mean residue ellipticity, generated from the protofibril peaks of the 20/0 and 20/56 preparations.

4.3 Discussion.

The tau project related in the previous chapter and both projects described in this one are similar in the eventual need to come to terms with the problem of imperfect starting material. In each case, concerns over preformed aggregates lead to additional experimental work. The results of that work may validate, or even improve upon or expand the prior analysis, but that does not mitigate the challenge posed to the researcher, and the questions they must ask even before beginning an experiment. That these issues arose so frequently in this dissertation (2 out of 3 projects) is not happenstance. It is a fundamental challenge pervasive within the field of study (Teplow 2006). Many workers side-step the issue, using aggregate preparations designed to be highly polydisperse. But that is not a choice when exploring the biophysics of specific aggregates, or the interactions of specific aggregates with living systems, which is crucial information for development of therapeutic strategies to combat AD.

Precautions taken against the influence of preformed aggregates on experimental preparations commonly include HFIP pre-treatment, high-alkaline conditions, and denaturing conditions. Even so, resistant aggregates may remain even after the most strident treatments, and these aggregates can form at times when intervention is out of the researcher's hands, such as during synthesis or lyophilization. Therefore, beginning with freshly purified monomer is the only way to demonstrably be certain to avoid the issue of preformed aggregates.

My studies of purified Aβ42 monomer aggregration reactions revealed that low concentration reactions proceeded through an extended lag phase before nucleation. After nucleation, elongation was rapid and the material quickly converted to fibril. However, the aggregation rate could be modulated by altering the buffer solution, the ionic strength, and temperature. At low ionic strengths, the same material which proceeded to fibril instead converted to protofilaments with molecular weights of around 3000 kDa, the equivalent of 665 monomers, and R_g values of 60 nm. These protofilaments had significantly different secondary structure compared to fibrils: enhanced α-helix content, and reduced β-sheet. Changing the buffer system entirely led to a two-component system, which was primarily fibril, but had a significant population of classic curvilinear protofibrils, morphologically identical to the protofibrils which formed rapidly when HFIP-processed Aβ42 peptide film was reconstituted under alkaline conditions.

Applying what this about protofibril and protofilament formation in purified monomer solutions, I explored the influence of isoform mixtures on protofibril formation. The study of amyloid aggregation in such mixed systems is an area where the literature is much lacking. This is especially pertinent as the *in vivo* environment in which these processes occur is certainly a heterogenous system.

My primary results with mixed solutions of purified monomer correlated with studies using HFIP-processed peptide films. In both cases, when total Aβ concentration was held constant, decreasing the Aβ42/Aβ40 ratio lead to a lower protofibril yield. This is concomitant with a decreasing β-sheet structure in the aggregation mixtures just prior to SEC-purification, as determined by dye-binding. When the purified protofibrils were probed for secondary structure with CD, a reduced β-sheet characteristic was noted along

with an increasing α-helical content. Interestingly, when Aβ42 was prepared at the same concentrations in the absence of Aβ40, only the secondary structural changes resulted, not the reduced protofibril yield. A closer comparison indicated that the presence of Aβ40 accentuated the reduced β-sheet and increased α-helical components.

Based on C-terminal selective ELISA results, it appeared unlikely that Aβ40 exerted its effects via high levels of direct incorporation, as only low amounts were detected in the purified protofibrils. One could posit a scenario where addition of Aβ40 or Aβ42 onto a growing nucleus occur at roughly the same rate, but then Aβ40 inhibits additional aggregation. However, that would likely require a high degree of incorporation of Aβ40 in the aggregates, which was shown not to be the case by the C-terminal-selective ELISA results. That said, it is certainly possible that trace involvement is responsible via a "capping" mechanism of some sort.

The presence of significant α-helical content in protofibrils is odd, as they are considered to possess a secondary structure enriched for the cross-β-sheet inter-molecular hydrogen bonds characteristic of fibrils. It is not unheard of, however. Some important early work by Teplow and Selkoe (Walsh et al. 1999, Kirkitadze et al. 2001) on the nucleation step and rapid protofibril formation identified a transient α-helical state before elongation. This state persisted longer in Aβ40 aggregation than Aβ42. Therefore, it is at least possible that the α-helical content increase indicates stabilization of this transient state in mixtures of Aβ42/Aβ40.

CHAPTER 5. A NOVEL ANTIBODY FOR Aβ42 PROTOFIBRIL.

5.1 Introduction.

5.1.1 The mammalian immune system

For narrative purposes this introduction begins with a description of the mammalian immune system. Numerous thorough reviews (Chaplin 2010) and textbook treatments of this subject are available. The immune system is the well-known evolutionarily conserved system of cells which protect the host organism from diverse exogenous threats to homeostasis and normal function. Threats from toxic or allergenic substances, as well as constantly evolving pathogenic microbial assault are extremely diverse. To achieve protection against such a broad range of threats requires properly functioning systems for identification of pathogens and toxins as distinct from host cells in ways that provide for elimination of threats without excessive damage to the host's tissue or its resident population of beneficial commensal microbes. However, some tissue damage is certainly involved in clearance of infected host cells. In mammals the immune system can be broadly divided into two functions: adaptive and innate immunity. These functions are performed for the most part by different cell types, however there is

significant inter-play between the responses, with part of the adaptive response involved in ramping-up the innate response.

5.1.2 Innate immunity.

Innate immunity is encoded at the germline of the host. It includes hard-wired functions such as the mucociliary system which shields the epithelia of the respiratory, genitourinary and gastrointestinal tracts. It is also responsible for detection and rapid response to a broad number of exogenous threats. This is achieved by expression of conserved receptors which can detect structural features shared by many microbes and toxins, so called pathogen anger-associated molecular patterns (PAMPs).

5.1.3 Adaptive immunity.

If the innate immune system response is a front-line, broadly applied defense, the adaptive immune system is specific and secondary. After exposure for the first time to a new toxin or pathogenic microbial product – what are called antigens, the adaptive system expresses receptor molecules tailored for highly specific recognition of distinct pathogens. These receptors are termed antibodies, and are generated via somatic rearrangement of germ-line genetic code, potentially allowing specific recognition of an astonishing number of different antigens. This potential has been adopted as an essential research tool for the biochemist or molecular biologist. Antibodies can be generated with high specificity for, essentially, whatever the researcher's molecule of interest may be. The full adaptive response to an antigen allows increased recruitment of innate and adaptive immune effectors to the site of the threat. It also *Fires the Big Guns*, so to speak, of the immune response, such as the colorfully named Natural Killer Cells, and the

colorlessly named Complement System, both of which exert powerful cytotoxic functions, including destruction of infected host cells.

5.1.4 Macrophages.

Macrophages are a component cell of the innate immune system. They are phagocytic cells which assist in removing pathogens and dead cells and debris (Franco et al. 2015). They also respond to PAMPs such as lipopolysaccharide (LPS), which are exogenous, as well as endogenous indicators of cell damage - danger associated molecular patterns (DAMPs) such as ATP and extracellular matrix proteins, and other immune cell signaling molecules. Dependent on the mixture of signals a resting macrophage receives, their activation will occur along different pathways, dubbed M1 and M2, and have different phenotypes, which appear geared for different, contrary, functions (note: this is a greatly simplified view!). The M1 activation phenotype is pro-inflammatory, while the M2 response is anti-inflammatory, and more active in phagocytosis and clearance (Franco et al. 2015). This is a simplified view, sufficient for framing the important aspects below. There are many detailed reviews of the subject available.

5.1.5 The neuroinflammatory response.

In the brain, the resident immune cell type is the microglial cell, which are similar to macrophages, and the similarity carries even to their activation states; the M1 and M2 states of microglia are pro-inflammatory and anti-inflammatory. Interestingly, Aβ can cause activation of microglial cells along the M1 pathway, as we, among others,

have shown (Terrill-Usery et al. 2014). A summary of microglial dysfunction in AD is provided in Figure 5.1A (Heneka et al. 2015).

DAMPs, including Aβ PF are recognized by the TLR4/CD14 complex, which causes translocation of NF- κB from the cytosol to the nucleus, initiating transcription of mRNA coding for pro-inflammatory signals, including TNF-α and pro-IL-1β (Figure 5.1B). Secretion of mature IL-1β requires a secondary signal to process the pro form. As we have shown previously, Aβ PF may initiate this signaling as well. A complete understanding of this second signal pathway is still elusive, and an area of active research. Indeed, the author devised a series of experiments on this subject in his dissertation proposal. It likely involves Aβ PF phagocytic uptake into the cell via a phagocytic process, followed by lysosomal damage and release of Cathepsin B from the lysosomal compartment (Halle et al. 2008). Result is assembly of the NLRP3 inflammasome complex, a multimeric complex composed of multiple subunits each of NLRP3, ASC, and pro-caspase-1. The active NLRP3 inflammasome permits the auto-catalytic cleavage of pro-caspase-1 into caspase-1. Caspase-1 in turn mediates cleavage of pro-IL-1β into the mature form for secretion. There is also evidence from *in vivo* studies of inflammation which highlights the importance of this pathway in AD pathology. APP/PS1 mice (a widely employed mouse model of AD), when crossed with knock-outs for either NLRP3 or Caspase-1 genes ($Nlrp3^{-/-}$ or $Casp1^{-/-}$), generated progeny with reduced AD pathology and cognitive defects (Schroder et al. 2010).

The presence of cytokines, particularly IL-1β, reduces phagocytosis of Aβ deposits (Koenigsknecht-Talboo et al. 2005). This may constitute a vicious cycle which maintains the neuroinflammatory response. Furthermore, increased IL-1β release may

play an active role in neurodegeneration. IL-1β appears to induce neuronal tau phosphorylation in a MAPK-p38 pathway-dependent manner. This also results in reduced synaptophysin production, which is a neuronal synaptic protein. It is interesting to note that this is one of multiple instances where tau has been implicated as a mediator of Aβ-induced pathology in AD. This link may explain the observed deleterious effects at the synapse which occur prior to outright neuronal death (Li et al. 2003)

The Aβ PF aggregate species is important for induction of AD neuroinflammatory pathology, and therefore a possible therapeutic target. The full pathway by which this occurs is not fully understood. Adding to these facts the deep experience the Nichols Lab has with generation and characterization of Aβ PFs, there was an excellent opportunity to explore the potential of an antibody generated against the PF aggregate, first as a research tool, but perhaps as the first step in a translational science project in the future. With funding received through a UM system grant, Pacific Immunology was contracted to generate a polyclonal mouse antibody against Aβ PF generated and purified by the Nichols Lab. The remainder of this chapter details a large amount of the work characterizing this antibody, named AbSL, in terms of specificity for PF over other Aβ species, and suitability for use in both immunoblot and ELISA formats. Additional work was performed to elucidate the nature of the AbSL epitope via competition assays with other Aβ-specific antibodies. The work was performed myself and two excellent undergraduate researchers, Elizabeth Ridgeway and Victoria Rogers, who's work I directed, while providing guidance in experimental technique and data analysis. A manuscript for journal submission is also currently being assembled describing these results.

Figure 5.1 Aβ and microglial pathology in AD.

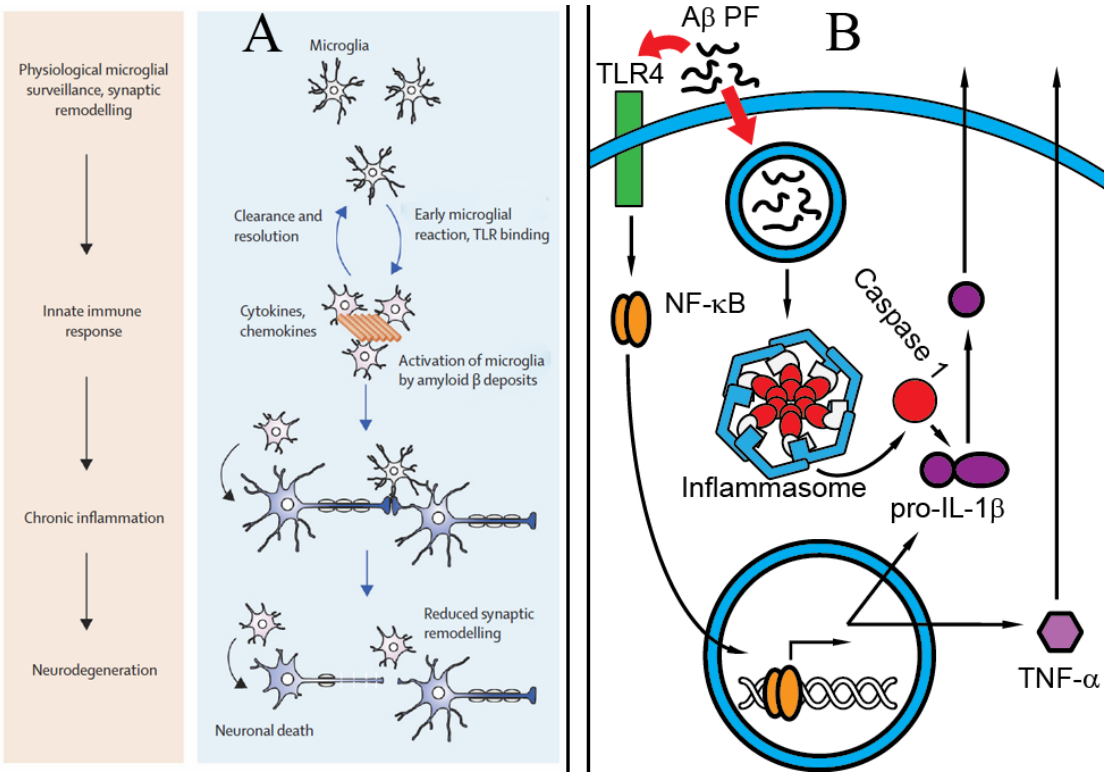

(A) Overview of microglial role in AD pathology. The early response to increased Aβ is phagocytosis and clearance. As neuroinflammation becomes chronic, microglial phagocytosis is reduced. IL-1β signaling results deleterious effects at the neuronal synapse and cytoskeletal levels, ultimately contributing to neuronal death. (B) Overview of induction of IL-1β signaling by Aβ protofibril (PF). Aβ PF activates the TLR4 receptor complex signaling pathway, resulting in NF-κB translocation into the nucleus and pro-IL-1β production. Aβ PF is also internalized into microglia, where it induces the secondary signal necessary for NLRP3 inflammasome-mediated cleavage of pro-caspase 1 into caspase-1, which in-turn cleaves pro-IL-1β, resulting in mature IL-1β which is then secreted. Panel A is from Heneka et al. 2013, and panel B is based on Terrill-Usery et al. 2014.

5.2 Results.

Aβ42 protofibrils were generated in the Nichols Lab from HFIP-processed dry peptide film (see methods), and then characterized and isolated via SEC. The purified protofibril was shipped overnight on ice to Pacific Immunology (CA) where generation of the antibody was performed. Two New Zealand White rabbits, designated PAC10079 and PAC10080 (PAC79 and PAC80), were immunized with 0.2 mg each of Aβ42 protofibrils in Freund's complete adjuvant. Pre-immunization serum was also obtained, and there were three subsequent immunizations of 0.2 mg Aβ42 protofibrils. A total of 5 immune bleeds (B1-B5) were received, along with one pre-immune bleed (PB), and a final exsanguination bleed (B6) from each rabbit.

5.2.1 Titer determinations.

My initial trials of the anti-sera in immunosorption and blotting formats were promising, so formal indirect ELISA anti-PF antibody titers were determined (Figure 5.2). Aβ protofibril was added to the wells of a 96-well-plate and incubated overnight at 4 ºC. The following day the adsorbed protofibril was probed with increasingly dilute anti-serum. The pre-immune bleed was also employed as a control. Bleeds from rabbit PAC79 remained constant after the first immunization bleed (Figure 5.2A), while bleeds from rabbit PAC80 demonstrated a continual increase in titer over the course of the immunizations (Figure 5.2B). Antibody titers for the antiserum ranged from 2,500 to >5,000. Figure 5.2C provides a schematic of the indirect ELISA configuration we utilized, which is further detailed in the methods. It was decided that the new antiserum

would be named AbSL, to honor the University of Missouri – Saint Louis campus, and, for the author, at least, because he was AbSoLutely thrilled about the project.

Figure 5.2 Indirect ELISA to determine antisera titers against Protofibril Aβ42.

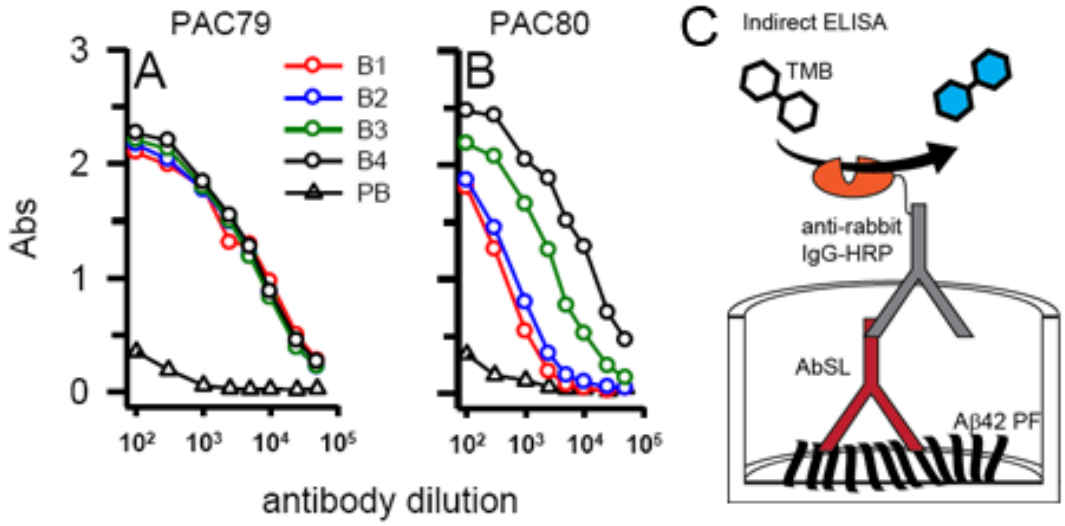

Representative titer ELISA results for bleeds from Pacific Immunology rabbits (A) PAC79 and (B) PAC80. 2 µM purified Aβ42 protofibril in aCSF buffer (pH 7.8) was diluted to 80 nM in 50 mM sodium bicarbonate (pH 9.6) coating solution. 50 µL (18 ng Aβ42) was added to each well, and incubated overnight at 4 ºC. Wells were washed once with 0.2% v/v Tween in 1X PBS (pH 7.4). Then 150 µL blocking buffer (10% w/v dry milk in wash buffer) was added to each well, and incubated for 1 h at 25 ºC followed by 3 washes. The four antibody bleeds (B1-B4) as well as the pre-bleed (PB) were prepared across a dilution range from 1/50 to 1/20,000 in antibody diluent (0.2% v/v Tween, 5% w/v dry milk in 1X PBS). Dilutions were added to triplicate wells, along with triplicate controls of antibody diluent alone, and incubated for 1 h at 25 ºC. Wells were washed four times with wash buffer, and 100 µL 1:1000 dilution of anti-rabbit IgG-HRP conjugate secondary antibody in antibody diluent was applied to each well, and incubated for 2 h at 25 ºC. Wells were washed four times with wash buffer, followed by quantification of detection with TMB substrate. Each data point in panels A and B is the mean absorbance of two sets of triplicate determinations each set generated by a different worker. (C) Cartoon describing the indirect ELISA format used in panels A and B.

5.2.2 Selective affinity of AbSL for Aβ42 protofibril conformation.

Aβ42 protofibril affinity of the anti-serum in an indirect ELISA was next compared with the its affinity towards Aβ42 monomer and fibril in the same format (Figure 5.3). A great degree of selectivity over a sizeable Aβ42 concentration range was seen for Aβ42 protofibrils over Aβ42 monomer (Figure 5.3A and 5.3B). A slightly reduced, though still highly significant, selectivity over Aβ42 fibrils was also revealed (Figure 5.3B). For comparison, a second set of experiments was performed in parallel, but in place of AbSL, Ab9 was used (Figure 5.3C). Ab9 is a general antibody for Aβ, which recognizes the N-terminal region of the peptide, without conformational specificity beyond accessibility. In this case, Ab9 showed no preference for any of the Aβ42 species, beyond slightly reduced binding to fibril, which is likely due to inaccessibility of the epitope sequence due to the denser packing found in fibrils.

Selectivity was also explored in a dot-blot format (Figure 5.4). Again, in this case AbSL demonstrated excellent specificity for Aβ42 protofibril over monomer (5.4A and 5.4B), and reduced though still obvious selectivity for Aβ42 protofibril over fibril (5.4B). Ab9 was again used as a control to ensure proper loading of Aβ42 species onto the blot membrane.

Figure 5.3 Indirect AbSL ELISA selects strongly for Aβ42 PF.

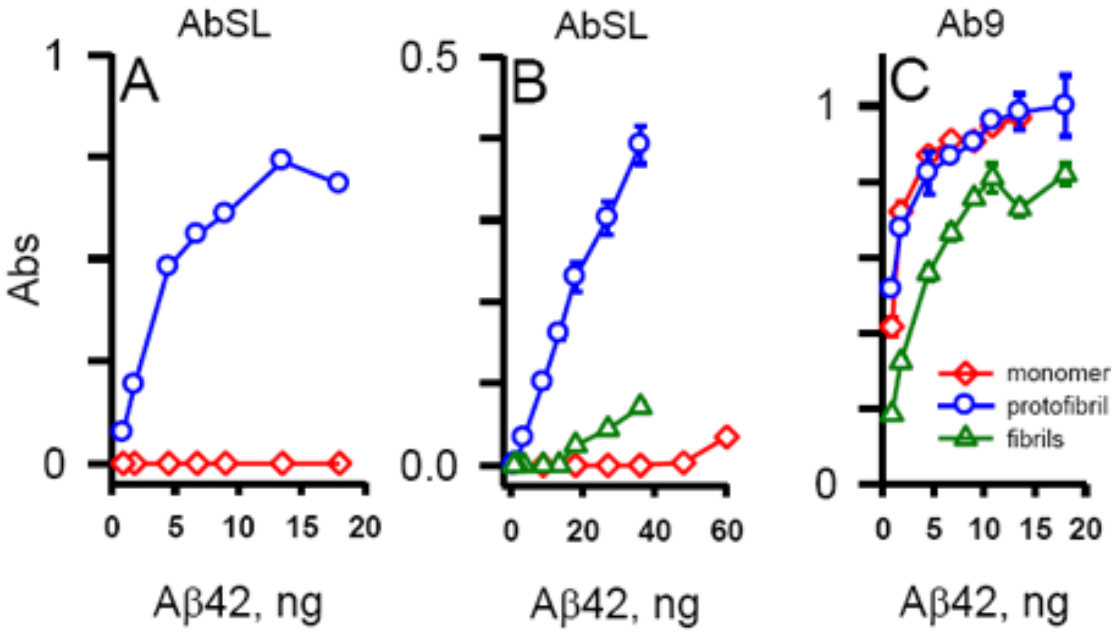

2 μM purified Aβ42 protofibril was diluted in carbonate buffer across a range of concentrations. Indirect ELISA was carried out as described in Figure 5-2 and Methods. (A) shows detection with 1:2000 dilution of AbSL at a lower Aβ42 concentration range, while (B) shows detection with 1:10000 dilution of AbSL at a higher overall range of Aβ42. (C) shows detection with 1:2000 dilution of Ab9, a non-aggregate specific anti-Aβ antibody, across the same range as panel A, for comparison. Where error bars are present (panels B and C), data points represent avg +- SEM for n = 3 ELISA determinations.

Figure 5.4 AbSL is selective for protofibril in a dot blot format.

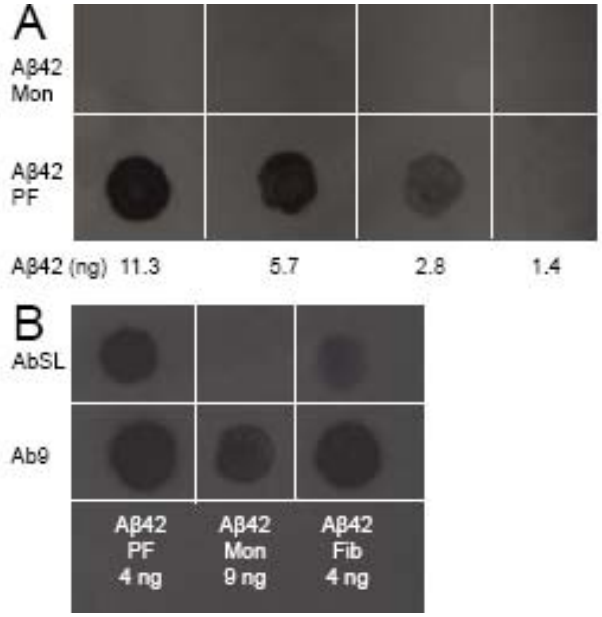

(A) Aβ42 monomer (Mon) or protofibril (PF) (SEC-purified) diluted into aCSF (pH 7.8), then 2 µL of each dilution was applied to nitrocellulose membrane (total mass Aβ42 in ng as indicated below each column), and incubated for 20 min at 25 ºC to allow adsorption into membrane matrix. Membranes were blocked with 5 mL 1X PBS (pH 7.4) with 0.01% v/v Tween 20 and 10% w/v dry milk (blocking buffer) for 1 h at 25 ºC with gentle shaking. Blocking buffer was then decanted and replaced with 5 mL 1:1000 dilution of AbSL in 1X PBS with 0.2% v/v Tween 20 and 5% w/v dry milk (antibody diluent), and the membrane was again shaken gently for 1 h at 25 ºC. Primary antibody solution was decanted, and membrane was washed with 1X PBS with 0.2% w/v Tween 20 (wash buffer) X3 for 5 min gentle shaking cycles at 25 ºC. 5 mL of 1:1000 antirabbit IgG-HrP conjugate in antibody diluent was added and the membrane was gently shaken for 1 h at 25 ºC. After another 3-wash sequence, ECL substrate (Pierce) was applied and incubated for 1 min with vigorous shaking at 25 ºC. Chemiluminescence was visualized with X-Ray film. (B) Prepared and annotated as described in panel A, with addition of fibril (Fib) (generated from SEC-purified monomer) spots. In this case 1:1000 dilution of AbSL was compared with 1:1000 dilution of Ab9, both prepared as described in panel A.

5.2.3 Selective affinity of AbSL for Aβ42 over Aβ40 protofibril.

Both Aβ42 and Aβ40 may form protofibril structures in solution, though Aβ40 requires much longer incubation times. In the past, many workers have taken advantage of the slow Aβ40 kinetics to investigate subtle events during aggregation which were difficult or impossible to probe using the more fibrillogenic Aβ42. Therefore, I asked if AbSL displayed any selectivity for protofibrils generated from Aβ42 over Aβ40 protofibrils. Using the same indirect ELISA paradigm as described above, the AbSL binding affinity for Aβ42 protofibril was compared to that for Aβ40 protofibril (Figure 5-5). Assuming a one-site saturation model, regression fitting was used to estimate equilibrium dissociation (Kd) and maximum binding sites (Bmax). The Kd for Aβ40 was approximately four-fold greater (16 ng/well vs 4 ng/well) suggesting a significant degree of selectivity for Aβ42 protofibrils.

Figure 5.5 AbSL has less affinity for Aβ40 protofibrils than Aβ42 protofibrils.

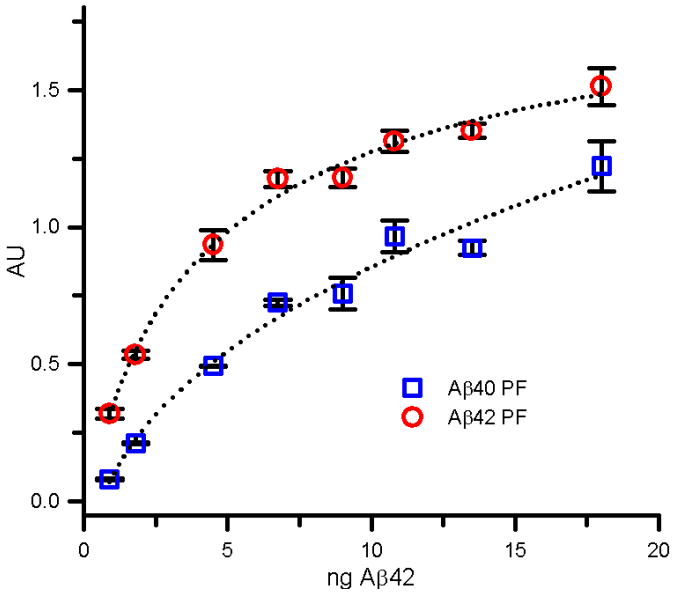

2 µM purified Aβ40 and Aβ42 protofibrils in aCSF buffer (pH 7.8) were diluted in 50 mM sodium bicarbonate (pH 9.6) coating solution, so that 50 µL would deliver 18, 13.5, 10.8, 9, 6.75, 4.5, 1.8, or 0.9 ng load per well. Wells were loaded in triplicate for each concentration for both Aβ40 and Aβ42, then incubated over night at 4 ºC. Wells were washed once with 0.2% v/v Tween in 1X PBS (pH 7.4). Then 150 µL blocking buffer (10% w/v dry milk in wash buffer) was added to each well, and incubated for 1 h at 25 ºC followed by 3 washes. The four antibody bleeds (B1-B4) as well as the pre-bleed (PB) were prepared across a dilution range from 1/50 to 1/20,000 in antibody diluent (0.2% v/v Tween, 5% w/v dry milk in 1X PBS). Dilutions were added to triplicate wells, along with triplicate controls of antibody diluent alone, and incubated for 1 h at 25 ºC. Wells were washed four times with wash buffer, and 100 µL 1:1000 dilution of anti-rabbit IgG-HRP conjugate secondary antibody in antibody diluent was applied to each well, and incubated for 2 h at 25 ºC. Wells were washed four times with wash buffer, followed by quantification of detection with TMB substrate. Data points and error bars represent avg +- SEM for n = 3 ELISA determinations.

5.2.4 Probing the AbSL epitope.

To gain information about the AbSL conformational epitope, a series of capture ELISA experiments were developed, using AbSL in conjunction with other Aβ antibodies. Figure 5.6A provides an overview of the ELISA experiments in cartoon form. The antibodies employed, their host animals, and specificities are summarized in Table 5.1, based on information from their developer, the Mayo Clinic.

The Aβ antibodies used, in addition to AbSL, were Ab2.1.3, Ab9, and HrP-conjugated Ab5 (Ab5-HrP). When AbSL was used as the primary detection antibody, antirabbit IgG-HrP (IgG-HrP) was used for secondary detection. The antibodies Ab2.1.3 and Ab5-HrP were used previously, along with Ab13.1.1 (Aβ40-selective, not used here), to quantify Aβ42/Aβ40 isoform contribution to protofibrils generated in mixed monomer solutions. To generate monoclonal Ab2.1.3, immunization was performed in mouse against a peptide consisting of the C-terminal 12 amino acid sequence of Aβ42: Aβ(35-42). After hybridoma fusion and colony amplification, the monoclonal antibody was then selected with full length Aβ42. Ab5 and Ab9 antibodies were generated in a similar fashion. The Ab5 immunogen was Aβ42 fibril with monoclonal selection with Aβ(1-16). For Ab9, Aβ(1-16) was both the immunogen and monoclonal selection screen.

In addition to the AbSL indirect ELISA, 280 nm absorbance signals were seen well above baseline for three of the configurations tested. Those were Ab2.1.3 capture with Ab5 detection (Ab2.1.3-Ab5), Ab2.1.3 capture with AbSL detection (Ab2.1.3-AbSL), and Ab9 capture with AbSL detection (Ab9-AbSL). Ab9 capture with Ab5 detection was not significantly above baseline, as expected, as both were raised against Aβ(1-16). The Ab2.1.3-Ab5 positive result was also as expected, based on their epitopes,

one being C-terminal and the other N-terminal. Ab2.1.3-AbSL and Ab9-AbSL were both positive results, however the Ab9-AbSL absorbance was attenuated, which may indicate some sequence overlap between the AbSL conformational epitope, and the Ab9 N-terminal sequence epitope.

This possible AbSL-Ab9 epitope overlap was explored further using indirect ELISA competition assays (Figure 5.7). As controls, Aβ42 was detected with Ab9, then secondary detection was performed with anti-mouse IgG-HrP, the positive control, or anti-rabbit IgG-HrP, the negative control. When Aβ42 was detected with a mixture of AbSL and Ab9, and then anti-rabbit secondary detection was performed for AbSL, the absorbance signal decreased with increasing Ab9 concentration, until a minimum plateau was reached. This indicated partial competition for epitope binding. If the entire Ab9 sequence epitope was involved in the conformational epitope of AbSL, one would expect a continued decrease in AbSL binding with increasing Ab9 concentration, until AbSL was entirely competed off the binding site.

For a final probe of the suspected AbSL-Ab9 epitope overlap, the Ab2.1.3-AbSL and Ab9-AbSL capture antibody ELISAs were repeated across a range of Aβ42 protofibril concentrations (Figure 5.8). The binding curve was reduced when Ab9 was used as capture, but superposition of the curves revealed similar shapes. This corroborated the evidence for partial overlap between AbSL and Ab9 epitopes.

Figure 5.6 ELISA-style probe of AbSL epitope sequence involvement.

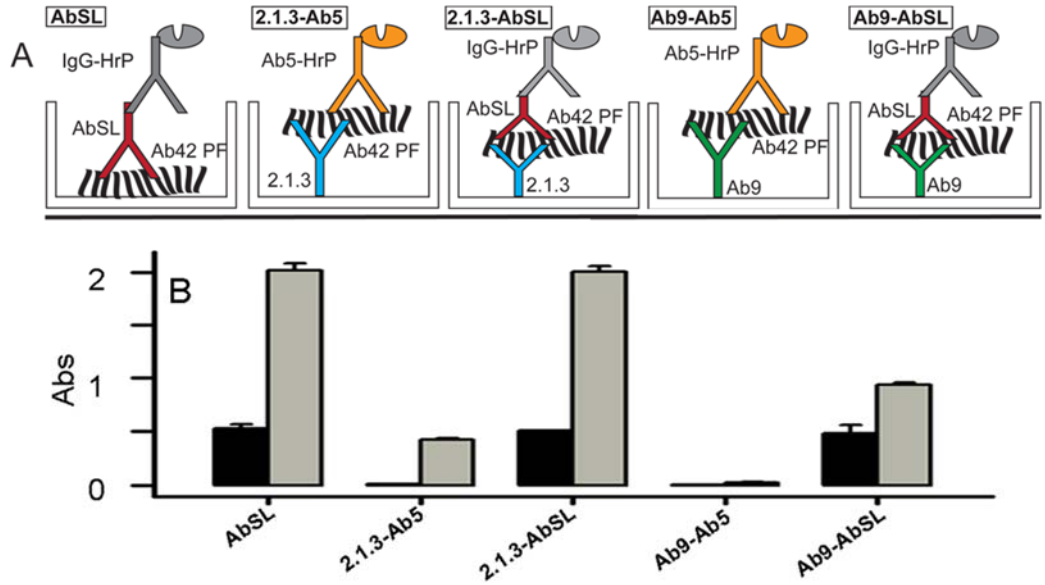

A) Immunosorbance systems examined in (B) are depicted in the cartoon. SEC-purified Aβ42 protofibril (Aβ42 PF, curving black arrays) concentration was 0.08 μM in sodium bicarbonate coating solution (pH 9.6) 50 μL was added into sample wells (18 ng Aβ42 per well). Antibodies were diluted into 1X PBS (pH 7.4). AbSL (red) dilution was 1:1000, Ab 2.1.3 (blue) was 1.7:1000, Ab9 (green)was 1:5000, Ab5-HrP (orange) was 1:2000 and antirabbit IgG-HrP (IgG-HrP, gray) was 1:1000. The antibody loading volumes were all 100 μL per well. (B) First, Aβ42 PF samples were added to [AbSL] wells and incubated overnight at 25 ºC. The next day, all remaining assay steps were performed in the same 96-well-plate, as described in the methods. Quantification was colourimetric via HrP-catalyzed oxidation of TMB substrate. 100 μL 1 M H_2SO_4 was added to quench reaction. Absorbance was measured at 450 nm on the platereader along with 630 nm absorbance, which was subtracted to adjust for optical differences between the wells themselves. Background controls (Black bars) were wells where the Aβ42 PF sample was replaced with coating solution alone. Each control data point is the mean of n = 2 replicates ± SEM. Sample data is mean of n = 4 replicates ± SEM.

Table 5.1 Summary of antibodies used in Figure 5.6.

Antibody	Host	Immunization	Monoclonal screen
AbSL	Rabbit	Aβ42 protofibril	n/a; anti-serum
Ab9	Mouse	Aβ(1-16)	Aβ(1-16)
Ab5-HrP	Mouse	Fibrillar Aβ42	Aβ(1-16)
Ab2.1.3	Mouse	Aβ(35-42)	Aβ42
IgG-HrP	Goat	Rabbit IgG	n/a; polyclonal

Figure 5.7 AbSL vs. Ab9 cis-competition ELISA.

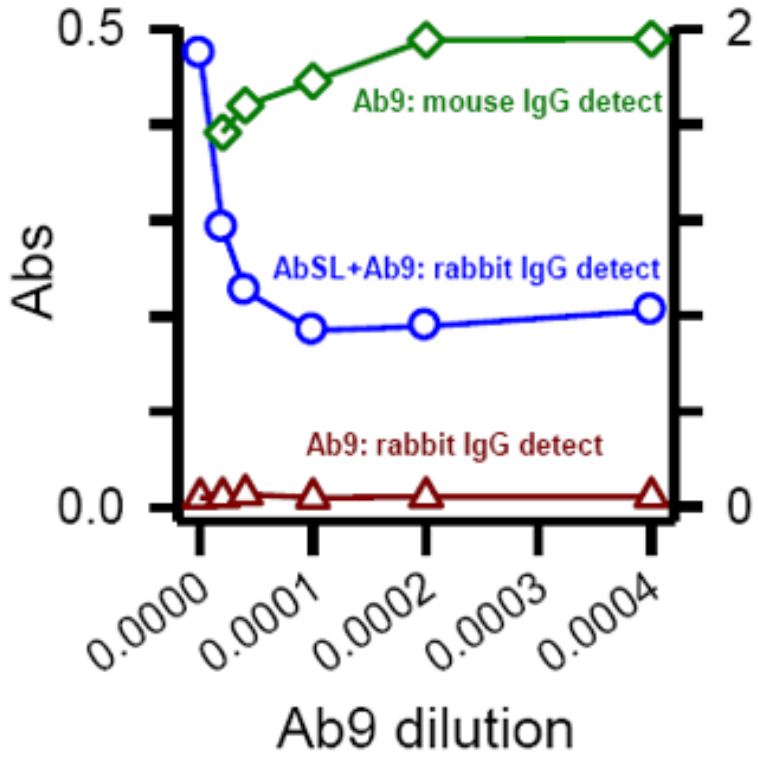

Aβ42 protofibrils were adsorbed overnight into wells of a 96-well immunoplate. Indirect ELISA was performed as described in the methods. Primary detection was performed with either Ab9 alone (1:2,500-1:50,000 dilutions) or Ab9 (same dilutions) mixed with AbSL, as indicated. AbSL was fixed at 1:1000 dilution. Secondary detection was performed with anti-rabbit IgG-HrP or anti-mouse IgG-HrP as indicated. Ab9 with anti-rabbit IgG-HrP secondary detection was performed as a negative control, as Ab9 was raised in mouse. The axes are both measures of absorbance, so that all conditions are visible.

Figure 5.8 AbSL vs. Ab2.1.3 trans-competition capture ELISA.

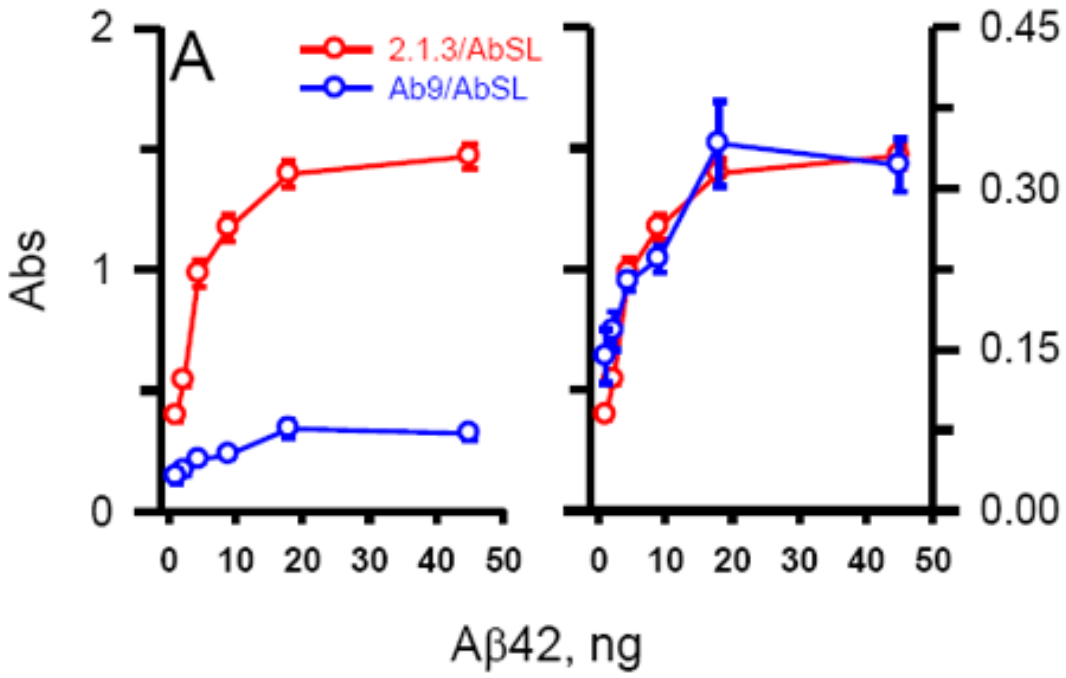

Capture antibodies of Ab2.1.3 or Ab9 were plated overnight in 96-well immunoplate wells, followed by addition of the indicated amounts of Aβ42 protofibril. Then detection was performed on both conditions with AbSL primary detection and anti-rabbit IgG-HrP secondary detection. The right panel shows the same data as the left panel, plotted on different y-axis scales to overlay the absorbances measured under each condition, and highlight the similarity of the curves.

5.3 Discussion.

I prepared Aβ42 protofibrils which were used to inoculate a pair of rabbits for generation of anti-serum. I characterized the anti-serum, which contained a high titer of antibody which recognized Aβ42 protofibrils.

I further evaluated the anti-serum for specific binding to the Aβ42 protofibril conformational epitope. I found it to be highly selective compared to both either monomer or fibril Aβ42 in both indirect ELISA and dot-blot formats. I also revealed a high degree of selectivity for Aβ42 protofibrils, over protofibrils formed from the other common Aβ isoform, Aβ40.

Finally, I probed the Aβ42 protofibril epitope itself in a series of ELISA formats, both capture and indirect. I found solid evidence which pointed to no involvement of the C-terminal region comprised of amino acids 25-42. On the other hand, the competition experiments using N-terminal sequence specific antibody Ab9 suggested a partial overlap between the conformational epitope of AbSL and the N-terminal 1-16 amino acid sequence of Aβ.

Additional work will include affinity purification of the anti-serum into a polyclonal antibody with improved affinity for Aβ42 protofibril, as well as characterization. This could be followed by generation of a monoclonal version using the same Aβ42 protofibril immunogen, if results are promising. Beyond that, the sky is the limit. A recent paper (Wang et al. 2016) showed administration of novel anti-Aβ oligomer 11A5 mixed with N-terminal Aβ antibody 6E10 improved cognitive deficits in

a mouse model of AD. Furthermore, a different antibody treatment for AD, aducanumab, is currently showing great promise in human clinical trials. The success of aducanumab especially demonstrates the potential of antibody-based therapies for amyloid diseases. The monoclonal antibody mAb158, raised in mouse, is selective for Aβ protofibril (Englund et al. 2007). A humanized version of mAb158, BAN2401, is another new example of an antibody-based potential therapy for AD (Logovinsky et al. 2016).

While this is certainly beneficial as a research tool, given the apparent importance of the chronic neuroinflammatory pathology to the overall progression of AD, I believe that AbSL may hold promise as a potential therapeutic, as demonstrated by the current interest in BAN2401. The neuroinflammatory axis of AD pathology appears to involve not only Aβ induced effects, but also the tau protein as well (Li et al. 2003). Likely there are other pathways by which AD neurodegeneration proceeds, but neuroinflammation is certainly a major component, making my work here a significant step in the right direction in the fight against AD.

REFERENCES

Alonso, A. C., T. Zaidi, I. Grundke-Iqbal and K. Iqbal (1994). "Role of abnormally phosphorylated tau in the breakdown of microtubules in Alzheimer disease." Proc Natl Acad Sci U S A **91**(12): 5562-5566.

Alonso Adel, C., B. Li, I. Grundke-Iqbal and K. Iqbal (2006). "Polymerization of hyperphosphorylated tau into filaments eliminates its inhibitory activity." Proc Natl Acad Sci U S A **103**(23): 8864-8869.

Alzheimer, A., R. A. Stelzmann, H. N. Schnitzlein and F. R. Murtagh (1995). "An English translation of Alzheimer's 1907 paper, "Uber eine eigenartige Erkankung der Hirnrinde"." Clin Anat **8**(6): 429-431.

Arosio, P., T. P. Knowles and S. Linse (2015). "On the lag phase in amyloid fibril formation." Phys Chem Chem Phys **17**(12): 7606-7618.

Axelsen, P. H., H. Komatsu and I. V. J. Murray (2011). "Oxidative Stress and Cell Membranes in the Pathogenesis of Alzheimer's Disease." Physiology **26**(1): 54-69.

Bartolini, M., C. Bertucci, M. L. Bolognesi, A. Cavalli, C. Melchiorre and V. Andrisano (2007). "Insight into the kinetic of amyloid β (1-42) peptide self-aggregation: Elucidation of inhibitors' mechanism of action." ChemBioChem **8**(17): 2152-2161.

Bentahir, M., O. Nyabi, J. Verhamme, A. Tolia, K. Horré, J. Wiltfang, H. Esselmann and B. De Strooper (2006). "Presenilin clinical mutations can affect γ-secretase activity by different mechanisms." Journal of Neurochemistry **96**(3): 732-742.

Berridge, M. J., M. D. Bootman and P. Lipp (1998). "Calcium--a life and death signal." Nature **395**(6703): 645-648.

Beyreuther, K. and C. L. Masters (1991). "Amyloid precursor protein (APP) and beta A4 amyloid in the etiology of Alzheimer's disease: precursor-product relationships in the derangement of neuronal function." Brain Pathol **1**(4): 241-251.

Billingsley, M. L. and R. L. Kincaid (1997). "Regulated phosphorylation and dephosphorylation of tau protein: effects on microtubule interaction, intracellular trafficking and neurodegeneration." Biochem J **323 (Pt 3)**: 577-591.

Braak, H. and E. Braak (1991). "Demonstration of amyloid deposits and neurofibrillary changes in whole brain sections." Brain Pathol **1**(3): 213-216.

Buee, L., T. Bussiere, V. Buee-Scherrer, A. Delacourte and P. R. Hof (2000). "Tau protein isoforms, phosphorylation and role in neurodegenerative disorders." Brain Res Brain Res Rev **33**(1): 95-130.

Buee, L. and A. Delacourte (1999). "Comparative biochemistry of tau in progressive supranuclear palsy, corticobasal degeneration, FTDP-17 and Pick's disease." Brain Pathol **9**(4): 681-693.

Burns, R. G. (1991). "Alpha-, beta-, and gamma-tubulins: sequence comparisons and structural constraints." Cell Motil Cytoskeleton **20**(3): 181-189.

Butner, K. A. and M. W. Kirschner (1991). "Tau protein binds to microtubules through a flexible array of distributed weak sites." J Cell Biol **115**(3): 717-730.

Chaplin, D. D. (2010). "Overview of the Immune Response." The Journal of allergy and clinical immunology **125**(2 Suppl 2): S3-23.

Chromy, B. A., R. J. Nowak, M. P. Lambert, K. L. Viola, L. Chang, P. T. Velasco, B. W. Jones, S. J. Fernandez, P. N. Lacor, P. Horowitz, C. E. Finch, G. A. Krafft and W. L. Klein (2003). "Self-Assembly of Aβ1-42 into Globular Neurotoxins." Biochemistry **42**(44): 12749-12760.

Clavaguera, F., T. Bolmont, R. A. Crowther, D. Abramowski, S. Frank, A. Probst, G. Fraser, A. K. Stalder, M. Beibel, M. Staufenbiel, M. Jucker, M. Goedert and M. Tolnay (2009). "Transmission and spreading of tauopathy in transgenic mouse brain." Nat Cell Biol **11**(7): 909-913.

Cleland, W. W. (1964). "Dithiothreitol, a New Protective Reagent for Sh Groups." Biochemistry **3**: 480-482.

Combs, B., C. Hamel and N. M. Kanaan (2016). "Pathological conformations involving the amino terminus of tau occur early in Alzheimer's disease and are differentially detected by monoclonal antibodies." Neurobiol Dis **94**: 18-31.

Cowan, C. M. and A. Mudher (2013). "Are tau aggregates toxic or protective in tauopathies?" Front Neurol **4**: 114.

Cox, K., B. Combs, B. Abdelmesih, G. Morfini, S. T. Brady and N. M. Kanaan (2016). "Analysis of isoform-specific tau aggregates suggests a common toxic mechanism involving similar pathological conformations and axonal transport inhibition." Neurobiol Aging **47**: 113-126.

De Strooper, B., R. Vassar and T. Golde (2010). "The secretases: enzymes with therapeutic potential in Alzheimer disease." Nat Rev Neurol **6**(2): 99-107.

Demuro, A., E. Mina, R. Kayed, S. C. Milton, I. Parker and C. G. Glabe (2005). "Calcium dysregulation and membrane disruption as a ubiquitous neurotoxic mechanism of soluble amyloid oligomers." J Biol Chem **280**(17): 17294-17300.

Deng, Y., L. Tarassishin, V. Kallhoff, E. Peethumnongsin, L. Wu, Y.-M. Li and H. Zheng (2006). "Deletion of Presenilin 1 Hydrophilic Loop Sequence Leads to Impaired γ-Secretase Activity and Exacerbated Amyloid Pathology." The Journal of Neuroscience **26**(14): 3845-3854.

Desai, A. and T. J. Mitchison (1997). "Microtubule polymerization dynamics." Annu Rev Cell Dev Biol **13**: 83-117.

Dobson, C. M. (1999). "Protein misfolding, evolution and disease." Trends Biochem Sci **24**(9): 329-332.

Drubin, D. G. and M. W. Kirschner (1986). "Tau protein function in living cells." J Cell Biol **103**(6 Pt 2): 2739-2746.

Englund, H., D. Sehlin, A. S. Johansson, L. N. Nilsson, P. Gellerfors, S. Paulie, L. Lannfelt and F. E. Pettersson (2007). "Sensitive ELISA detection of amyloid-beta protofibrils in biological samples." J Neurochem **103**(1): 334-345.

Fanara, P., K. H. Husted, K. Selle, P. Y. Wong, J. Banerjee, R. Brandt and M. K. Hellerstein (2010). "Changes in microtubule turnover accompany synaptic plasticity and memory formation in response to contextual fear conditioning in mice." Neuroscience **168**(1): 167-178.

Feany, M. B., L. A. Mattiace and D. W. Dickson (1996). "Neuropathologic overlap of progressive supranuclear palsy, Pick's disease and corticobasal degeneration." J Neuropathol Exp Neurol **55**(1): 53-67.

Fernandez-Nogales, M., J. R. Cabrera, M. Santos-Galindo, J. J. Hoozemans, I. Ferrer, A. J. Rozemuller, F. Hernandez, J. Avila and J. J. Lucas (2014). "Huntington's disease is a four-repeat tauopathy with tau nuclear rods." Nat Med **20**(8): 881-885.

Flach, K., I. Hilbrich, A. Schiffmann, U. Gartner, M. Kruger, M. Leonhardt, H. Waschipky, L. Wick, T. Arendt and M. Holzer (2012). "Tau oligomers impair artificial membrane integrity and cellular viability." J Biol Chem **287**(52): 43223-43233.

Franco, R. and D. Fernández-Suárez (2015). "Alternatively activated microglia and macrophages in the central nervous system." Progress in Neurobiology **131**: 65-86.

Frost, B., R. L. Jacks and M. I. Diamond (2009). "Propagation of tau misfolding from the outside to the inside of a cell." J Biol Chem **284**(19): 12845-12852.

Galpern, W. R. and A. E. Lang (2006). "Interface between tauopathies and synucleinopathies: a tale of two proteins." Ann Neurol **59**(3): 449-458.

Giuffrida, M. L., F. Caraci, B. Pignataro, S. Cataldo, P. De Bona, V. Bruno, G. Molinaro, G. Pappalardo, A. Messina, A. Palmigiano, D. Garozzo, F. Nicoletti, E. Rizzarelli and A. Copani (2009). "Beta-amyloid monomers are neuroprotective." J Neurosci **29**(34): 10582-10587.

Goedert, M., B. Falcon, F. Clavaguera and M. Tolnay (2014). "Prion-like mechanisms in the pathogenesis of tauopathies and synucleinopathies." Curr Neurol Neurosci Rep **14**(11): 495.

Goedert, M., M. G. Spillantini, M. C. Potier, J. Ulrich and R. A. Crowther (1989). "Cloning and sequencing of the cDNA encoding an isoform of microtubule-associated protein tau containing four tandem repeats: differential expression of tau protein mRNAs in human brain." EMBO J **8**(2): 393-399.

Gravina, S. A., L. Ho, C. B. Eckman, K. E. Long, L. Otvos Jr, L. H. Younkin, N. Suzuki and S. G. Younkin (1995). "Amyloid β protein (Aβ) in Alzheimer's disease brain: Biochemical and immunocytochemical analysis with antibodies specific for forms ending at Aβ40 or Aβ42(43)." Journal of Biological Chemistry **270**(13): 7013-7016.

Grundke-Iqbal, I., K. Iqbal, M. Quinlan, Y. C. Tung, M. S. Zaidi and H. M. Wisniewski (1986). "Microtubule-associated protein tau. A component of Alzheimer paired helical filaments." J Biol Chem **261**(13): 6084-6089.

Gu, Y., F. Oyama and Y. Ihara (1996). "Tau is widely expressed in rat tissues." J Neurochem **67**(3): 1235-1244.

Guerrero-Munoz, M. J., J. Gerson and D. L. Castillo-Carranza (2015). "Tau Oligomers: The Toxic Player at Synapses in Alzheimer's Disease." Front Cell Neurosci **9**: 464.

Guo, J. L. and V. M. Lee (2011). "Seeding of normal Tau by pathological Tau conformers drives pathogenesis of Alzheimer-like tangles." J Biol Chem **286**(17): 15317-15331.

Halle, A., V. Hornung, G. C. Petzold, C. R. Stewart, B. G. Monks, T. Reinheckel, K. A. Fitzgerald, E. Latz, K. J. Moore and D. T. Golenbock (2008). "The NALP3 inflammasome is involved in the innate immune response to amyloid-beta." Nat Immunol **9**(8): 857-865.

Hansson, O., H. Zetterberg, E. Vanmechelen, H. Vanderstichele, U. Andreasson, E. Londos, A. Wallin, L. Minthon and K. Blennow (2010). "Evaluation of plasma Aβ40 and Aβ42 as predictors of conversion to Alzheimer's disease in patients with mild cognitive impairment." Neurobiology of Aging **31**(3): 357-367.

Hardy, J. (1997). "Amyloid, the presenilins and Alzheimer's disease." Trends Neurosci **20**(4): 154-159.

Hardy, J. and D. Allsop (1991). "Amyloid deposition as the central event in the aetiology of Alzheimer's disease." Trends Pharmacol Sci **12**(10): 383-388.

Hardy, J. A. and G. A. Higgins (1992). "Alzheimer's disease: the amyloid cascade hypothesis." Science **256**(5054): 184-185.

Harper, J. D., S. S. Wong, C. M. Lieber and P. T. Lansbury Jr (1999). "Assembly of Aβ amyloid protofibrils: An in vitro model for a possible early event in Alzheimer's disease." Biochemistry **38**(28): 8972-8980.

Head, E., D. Powell, B. T. Gold and F. A. Schmitt (2012). "Alzheimer's Disease in Down Syndrome." Eur J Neurodegener Dis **1**(3): 353-364.

Heneka, M. T., M. J. Carson, J. E. Khoury, G. E. Landreth, F. Brosseron, D. L. Feinstein, A. H. Jacobs, T. Wyss-Coray, J. Vitorica, R. M. Ransohoff, K. Herrup, S. A. Frautschy, B. Finsen, G. C. Brown, A. Verkhratsky, K. Yamanaka, J. Koistinaho, E. Latz, A. Halle, G. C. Petzold, T. Town, D. Morgan, M. L. Shinohara, V. H. Perry, C. Holmes, N. G. Bazan, D. J. Brooks, S. Hunot, B. Joseph, N. Deigendesch, O. Garaschuk, E. Boddeke, C. A. Dinarello, J. C. Breitner, G. M. Cole, D. T. Golenbock and M. P. Kummer (2015). "Neuroinflammation in Alzheimer's disease." The Lancet Neurology **14**(4): 388-405.

Henkins, K. M., S. Sokolow, C. A. Miller, H. V. Vinters, W. W. Poon, L. B. Cornwell, T. Saing and K. H. Gylys (2012). "Extensive p-Tau Pathology and SDS-Stable p-Tau Oligomers in Alzheimer's Cortical Synapses." Brain Pathology **22**(6): 826-833.

Hirokawa, N. and R. Takemura (2005). "Molecular motors and mechanisms of directional transport in neurons." Nat Rev Neurosci **6**(3): 201-214.

Holmes, B. B., S. L. DeVos, N. Kfoury, M. Li, R. Jacks, K. Yanamandra, M. O. Ouidja, F. M. Brodsky, J. Marasa, D. P. Bagchi, P. T. Kotzbauer, T. M. Miller, D. Papy-Garcia and M. I. Diamond (2013). "Heparan sulfate proteoglycans mediate internalization and propagation of specific proteopathic seeds." Proc Natl Acad Sci U S A **110**(33): E3138-3147.

Hu, X., X. Li, M. Zhao, A. Gottesdiener, W. Luo and S. Paul (2014). "Tau pathogenesis is promoted by Abeta1-42 but not Abeta1-40." Mol Neurodegener **9**: 52.

Jack, C. R., Jr., D. S. Knopman, W. J. Jagust, R. C. Petersen, M. W. Weiner, P. S. Aisen, L. M. Shaw, P. Vemuri, H. J. Wiste, S. D. Weigand, T. G. Lesnick, V. S. Pankratz, M. C. Donohue and J. Q. Trojanowski (2013). "Tracking pathophysiological processes in Alzheimer's disease: an updated hypothetical model of dynamic biomarkers." Lancet Neurol **12**(2): 207-216.

Jan, A., O. Gokce, R. Luthi-Carter and H. A. Lashuel (2008). "The ratio of monomeric to aggregated forms of Abeta40 and Abeta42 is an important determinant of amyloid-beta aggregation, fibrillogenesis, and toxicity." J Biol Chem **283**(42): 28176-28189.

Jarrett, J. T., E. P. Berger and P. T. Lansbury (1993). "The carboxy terminus of the .beta. amyloid protein is critical for the seeding of amyloid formation: Implications for the pathogenesis of Alzheimer's disease." Biochemistry **32**(18): 4693-4697.

Jin, L. W., K. A. Claborn, M. Kurimoto, M. A. Geday, I. Maezawa, F. Sohraby, M. Estrada, W. Kaminksy and B. Kahr (2003). "Imaging linear birefringence and dichroism in cerebral amyloid pathologies." Proc Natl Acad Sci U S A **100**(26): 15294-15298.

Jin, M., N. Shepardson, T. Yang, G. Chen, D. Walsh and D. J. Selkoe (2011). "Soluble amyloid beta-protein dimers isolated from Alzheimer cortex directly induce Tau hyperphosphorylation and neuritic degeneration." Proc Natl Acad Sci U S A **108**(14): 5819-5824.

Kanaan, N. M., G. A. Morfini, N. E. LaPointe, G. F. Pigino, K. R. Patterson, Y. Song, A. Andreadis, Y. Fu, S. T. Brady and L. I. Binder (2011). "Pathogenic forms of tau inhibit kinesin-dependent axonal transport through a mechanism involving activation of axonal phosphotransferases." J Neurosci **31**(27): 9858-9868.

Kang, J., H. G. Lemaire, A. Unterbeck, J. M. Salbaum, C. L. Masters, K. H. Grzeschik, G. Multhaup, K. Beyreuther and B. Muller-Hill (1987). "The precursor of Alzheimer's disease amyloid A4 protein resembles a cell-surface receptor." Nature **325**(6106): 733-736.

Karran, E. and B. De Strooper (2016). "The amyloid cascade hypothesis: are we poised for success or failure?" J Neurochem.

Kayed, R., Y. Sokolov, B. Edmonds, T. M. McIntire, S. C. Milton, J. E. Hall and C. G. Glabe (2004). "Permeabilization of lipid bilayers is a common conformation-dependent activity of soluble amyloid oligomers in protein misfolding diseases." J Biol Chem **279**(45): 46363-46366.

Kelly, J. W. (2000). "Mechanisms of amyloidogenesis." Nat Struct Biol **7**(10): 824-826.

Kempf, M., A. Clement, A. Faissner, G. Lee and R. Brandt (1996). "Tau binds to the distal axon early in development of polarity in a microtubule- and microfilament-dependent manner." J Neurosci **16**(18): 5583-5592.

Khatoon, S., I. Grundke-Iqbal and K. Iqbal (1992). "Brain levels of microtubule-associated protein tau are elevated in Alzheimer's disease: a radioimmuno-slot-blot assay for nanograms of the protein." J Neurochem **59**(2): 750-753.

Kim, D., S. Lim, M. M. Haque, N. Ryoo, H. S. Hong, H. Rhim, D. E. Lee, Y. T. Chang, J. S. Lee, E. Cheong, D. J. Kim and Y. K. Kim (2015). "Identification of disulfide cross-linked tau dimer responsible for tau propagation." Sci Rep **5**: 15231.

Kim, J., L. Onstead, S. Randle, R. Price, L. Smithson, C. Zwizinski, D. W. Dickson, T. Golde and E. McGowan (2007). "Aβ40 Inhibits Amyloid Deposition In Vivo." The Journal of Neuroscience **27**(3): 627-633.

King, M. E., H. M. Kan, P. W. Baas, A. Erisir, C. G. Glabe and G. S. Bloom (2006). "Tau-dependent microtubule disassembly initiated by prefibrillar beta-amyloid." J Cell Biol **175**(4): 541-546.

Kirkitadze, M. D., M. M. Condron and D. B. Teplow (2001). "Identification and characterization of key kinetic intermediates in amyloid β-protein fibrillogenesis." Journal of Molecular Biology **312**(5): 1103-1119.

Koenigsknecht-Talboo, J. and G. E. Landreth (2005). "Microglial phagocytosis induced by fibrillar beta-amyloid and IgGs are differentially regulated by proinflammatory cytokines." J Neurosci **25**(36): 8240-8249.

Kolarova, M., F. Garcia-Sierra, A. Bartos, J. Ricny and D. Ripova (2012). "Structure and pathology of tau protein in Alzheimer disease." Int J Alzheimers Dis **2012**: 731526.

Kopke, E., Y. C. Tung, S. Shaikh, A. C. Alonso, K. Iqbal and I. Grundke-Iqbal (1993). "Microtubule-associated protein tau. Abnormal phosphorylation of a non-paired helical filament pool in Alzheimer disease." J Biol Chem **268**(32): 24374-24384.

Kuperstein, I., K. Broersen, I. Benilova, J. Rozenski, W. Jonckheere, M. Debulpaep, A. Vandersteen, I. Segers-Nolten, K. Van Der Werf, V. Subramaniam, D. Braeken, G. Callewaert, C. Bartic, R. D'Hooge, I. C. Martins, F. Rousseau, J. Schymkowitz and B. De Strooper (2010). "Neurotoxicity of Alzheimer's disease Aβ peptides is induced by small

changes in the Aβ₄₂ to Aβ₄₀ ratio." The EMBO Journal **29**(19): 3408-3420.

Lambert, M. P., A. K. Barlow, B. A. Chromy, C. Edwards, R. Freed, M. Liosatos, T. E. Morgan, I. Rozovsky, B. Trommer, K. L. Viola, P. Wals, C. Zhang, C. E. Finch, G. A. Krafft and W. L. Klein (1998). "Diffusible, nonfibrillar ligands derived from Aβ1–42 are potent central nervous system neurotoxins." Proceedings of the National Academy of Sciences **95**(11): 6448-6453.

Lasagna-Reeves, C. A., D. L. Castillo-Carranza, M. J. Guerrero-Muoz, G. R. Jackson and R. Kayed (2010). "Preparation and characterization of neurotoxic tau oligomers." Biochemistry **49**(47): 10039-10041.

Lasagna-Reeves, C. A., D. L. Castillo-Carranza, U. Sengupta, A. L. Clos, G. R. Jackson and R. Kayed (2011). "Tau oligomers impair memory and induce synaptic and mitochondrial dysfunction in wild-type mice." Mol Neurodegener **6**: 39.

Lasagna-Reeves, C. A., D. L. Castillo-Carranza, U. Sengupta, M. J. Guerrero-Munoz, T. Kiritoshi, V. Neugebauer, G. R. Jackson and R. Kayed (2012). "Alzheimer brain-derived tau oligomers propagate pathology from endogenous tau." Sci Rep **2**: 700.

Lasagna-Reeves, C. A., D. L. Castillo-Carranza, U. Sengupta, J. Sarmiento, J. Troncoso, G. R. Jackson and R. Kayed (2012). "Identification of oligomers at early stages of tau aggregation in Alzheimer's disease." FASEB J **26**(5): 1946-1959.

Lee, G., R. L. Neve and K. S. Kosik (1989). "The microtubule binding domain of tau protein." Neuron **2**(6): 1615-1624.

Lee, G., S. T. Newman, D. L. Gard, H. Band and G. Panchamoorthy (1998). "Tau interacts with src-family non-receptor tyrosine kinases." J Cell Sci **111 (Pt 21)**: 3167-3177.

Lei, P., S. Ayton, S. Moon, Q. Zhang, I. Volitakis, D. I. Finkelstein and A. I. Bush (2014). "Motor and cognitive deficits in aged tau knockout mice in two background strains." Mol Neurodegener **9**: 29.

Lesne, S., M. T. Koh, L. Kotilinek, R. Kayed, C. G. Glabe, A. Yang, M. Gallagher and K. H. Ashe (2006). "A specific amyloid-beta protein assembly in the brain impairs memory." Nature **440**(7082): 352-357.

Li, Y., L. Liu, S. W. Barger and W. S. Griffin (2003). "Interleukin-1 mediates pathological effects of microglia on tau phosphorylation and on synaptophysin synthesis in cortical neurons through a p38-MAPK pathway." J Neurosci **23**(5): 1605-1611.

Lindwall, G. and R. D. Cole (1984). "Phosphorylation affects the ability of tau protein to promote microtubule assembly." J Biol Chem **259**(8): 5301-5305.

Liu, L., V. Drouet, J. W. Wu, M. P. Witter, S. A. Small, C. Clelland and K. Duff (2012). "Trans-synaptic spread of tau pathology in vivo." PLoS One **7**(2): e31302.

Liu, R. Q., Q. H. Zhou, S. R. Ji, Q. Zhou, D. Feng, Y. Wu and S. F. Sui (2010). "Membrane localization of beta-amyloid 1-42 in lysosomes: a possible mechanism for lysosome labilization." J Biol Chem **285**(26): 19986-19996.

Logovinsky, V., A. Satlin, R. Lai, C. Swanson, J. Kaplow, G. Osswald, H. Basun and L. Lannfelt (2016). "Safety and tolerability of BAN2401--a clinical study in Alzheimer's disease with a protofibril selective Abeta antibody." Alzheimers Res Ther **8**(1): 14.

Makrides, V., T. E. Shen, R. Bhatia, B. L. Smith, J. Thimm, R. Lal and S. C. Feinstein (2003). "Microtubule-dependent Oligomerization of Tau: IMPLICATIONS FOR PHYSIOLOGICAL TAU FUNCTION AND TAUOPATHIES." Journal of Biological Chemistry **278**(35): 33298-33304.

Margittai, M. and R. Langen (2004). "Template-assisted filament growth by parallel stacking of tau." Proc Natl Acad Sci U S A **101**(28): 10278-10283.

Margittai, M. and R. Langen (2006). "Side chain-dependent stacking modulates tau filament structure." J Biol Chem **281**(49): 37820-37827.

Masters, C. L. and D. J. Selkoe (2012). "Biochemistry of amyloid beta-protein and amyloid deposits in Alzheimer disease." Cold Spring Harb Perspect Med **2**(6): a006262.

Michel, C. H., S. Kumar, D. Pinotsi, A. Tunnacliffe, P. St George-Hyslop, E. Mandelkow, E. M. Mandelkow, C. F. Kaminski and G. S. Kaminski Schierle (2014). "Extracellular monomeric tau protein is sufficient to initiate the spread of tau protein pathology." J Biol Chem **289**(2): 956-967.

Mirbaha, H., B. B. Holmes, D. W. Sanders, J. Bieschke and M. I. Diamond (2015). "Tau Trimers Are the Minimal Propagation Unit Spontaneously Internalized to Seed Intracellular Aggregation." J Biol Chem **290**(24): 14893-14903.

Mizuno, T. (2012). "The biphasic role of microglia in Alzheimer's disease." Int J Alzheimers Dis **2012**: 737846.

Morris, M., S. Maeda, K. Vossel and L. Mucke (2011). "The many faces of tau." Neuron **70**(3): 410-426.

Mukrasch, M. D., S. Bibow, J. Korukottu, S. Jeganathan, J. Biernat, C. Griesinger, E. Mandelkow and M. Zweckstetter (2009). "Structural polymorphism of 441-residue tau at single residue resolution." PLoS Biol **7**(2): e34.

Nichols, M. R., B. A. Colvin, E. A. Hood, G. S. Paranjape, D. C. Osborn and S. E. Terrill-Usery (2015). "Biophysical comparison of soluble amyloid-beta(1-42) protofibrils, oligomers, and protofilaments." Biochemistry **54**(13): 2193-2204.

Nichols, M. R., M. A. Moss, D. K. Reed, W. L. Lin, R. Mukhopadhyay, J. H. Hoh and T. L. Rosenberry (2002). "Growth of beta-amyloid(1-40) protofibrils by monomer elongation and lateral association. Characterization of distinct products by light scattering and atomic force microscopy." Biochemistry **41**(19): 6115-6127.

O'Brien, R. J. and P. C. Wong (2011). "Amyloid precursor protein processing and Alzheimer's disease." Annu Rev Neurosci **34**: 185-204.

O'Nuallain, B., A. D. Williams, P. Westermark and R. Wetzel (2004). "Seeding specificity in amyloid growth induced by heterologous fibrils." J Biol Chem **279**(17): 17490-17499.

Ogendal, L. (2013). "Light Scattering Demystified, Theory and Pratice."

Paranjape, G. S., L. K. Gouwens, D. C. Osborn and M. R. Nichols (2012). "Isolated amyloid-beta(1-42) protofibrils, but not isolated fibrils, are robust stimulators of microglia." ACS Chem Neurosci **3**(4): 302-311.

Paranjape, G. S., S. E. Terrill, L. K. Gouwens, B. M. Ruck and M. R. Nichols (2013). "Amyloid-beta(1-42) protofibrils formed in modified artificial cerebrospinal fluid bind and activate microglia." J Neuroimmune Pharmacol **8**(1): 312-322.

Patterson, K. R., C. Remmers, Y. Fu, S. Brooker, N. M. Kanaan, L. Vana, S. Ward, J. F. Reyes, K. Philibert, M. J. Glucksman and L. I. Binder (2011). "Characterization of prefibrillar Tau oligomers in vitro and in Alzheimer disease." J Biol Chem **286**(26): 23063-23076.

Pauwels, K., T. L. Williams, K. L. Morris, W. Jonckheere, A. Vandersteen, G. Kelly, J. Schymkowitz, F. Rousseau, A. Pastore, L. C. Serpell and K. Broersen (2012). "Structural Basis for Increased Toxicity of Pathological Aβ42:Aβ40 Ratios in Alzheimer Disease." Journal of Biological Chemistry **287**(8): 5650-5660.

Pierce protein assay handbook. "Thermo Scientific Pierce protein assay technical handbook." from https://tools.thermofisher.com/content/sfs/brochures/1602063-Protein-Assay-Handbook.pdf.

Pierrot, N., P. Ghisdal, A. S. Caumont and J. N. Octave (2004). "Intraneuronal amyloid-beta1-42 production triggered by sustained increase of cytosolic calcium concentration induces neuronal death." J Neurochem **88**(5): 1140-1150.

Polanco, J. C. and J. Gotz (2015). "No full admission for tau to the exclusive prion club yet." Embo j **34**(24): 2990-2992.

Prasher, V. P., M. J. Farrer, A. M. Kessling, E. M. Fisher, R. J. West, P. C. Barber and A. C. Butler (1998). "Molecular mapping of Alzheimer-type dementia in Down's syndrome." Ann Neurol **43**(3): 380-383.

Qiang, L., W. Yu, A. Andreadis, M. Luo and P. W. Baas (2006). "Tau protects microtubules in the axon from severing by katanin." J Neurosci **26**(12): 3120-3129.

Relini, A., S. Torrassa, R. Rolandi, A. Gliozzi, C. Rosano, C. Canale, M. Bolognesi, G. Plakoutsi, M. Bucciantini, F. Chiti and M. Stefani (2004). "Monitoring the process of HypF fibrillization and liposome permeabilization by protofibrils." J Mol Biol **338**(5): 943-957.

Rumble, B., R. Retallack, C. Hilbich, G. Simms, G. Multhaup, R. Martins, A. Hockey, P. Montgomery, K. Beyreuther and C. L. Masters (1989). "Amyloid A4 protein and its

precursor in Down's syndrome and Alzheimer's disease." N Engl J Med **320**(22): 1446-1452.

Sahara, N., S. Maeda, M. Murayama, T. Suzuki, N. Dohmae, S. H. Yen and A. Takashima (2007). "Assembly of two distinct dimers and higher-order oligomers from full-length tau." Eur J Neurosci **25**(10): 3020-3029.

Saman, S., W. Kim, M. Raya, Y. Visnick, S. Miro, S. Saman, B. Jackson, A. C. McKee, V. E. Alvarez, N. C. Lee and G. F. Hall (2012). "Exosome-associated tau is secreted in tauopathy models and is selectively phosphorylated in cerebrospinal fluid in early Alzheimer disease." J Biol Chem **287**(6): 3842-3849.

Santacruz, K., J. Lewis, T. Spires, J. Paulson, L. Kotilinek, M. Ingelsson, A. Guimaraes, M. DeTure, M. Ramsden, E. McGowan, C. Forster, M. Yue, J. Orne, C. Janus, A. Mariash, M. Kuskowski, B. Hyman, M. Hutton and K. H. Ashe (2005). "Tau suppression in a neurodegenerative mouse model improves memory function." Science **309**(5733): 476-481.

Scheuner, D., C. Eckman, M. Jensen, X. Song, M. Citron, N. Suzuki, T. D. Bird, J. Hardy, M. Hutton, W. Kukull, E. Larson, E. Levy-Lahad, M. Viitanen, E. Peskind, P. Poorkaj, G. Schellenberg, R. Tanzi, W. Wasco, L. Lannfelt, D. Selkoe and S. Younkin (1996). "Secreted amyloid beta-protein similar to that in the senile plaques of Alzheimer's disease is increased in vivo by the presenilin 1 and 2 and APP mutations linked to familial Alzheimer's disease." Nat Med **2**(8): 864-870.

Schroder, K. and J. Tschopp (2010). "The inflammasomes." Cell **140**(6): 821-832.

Selkoe, D. J. (1991). "The molecular pathology of Alzheimer's disease." Neuron **6**(4): 487-498.

Selkoe, D. J. (2000). "The genetics and molecular pathology of Alzheimer's disease: roles of amyloid and the presenilins." Neurol Clin **18**(4): 903-922.

Selkoe, D. J. (2001). "Alzheimer's disease: genes, proteins, and therapy." Physiol Rev **81**: 741-766.

Selkoe, D. J. (2004). "Cell biology of protein misfolding: The examples of Alzheimer's and Parkinson's diseases." Nat Cell Biol **6**(11): 1054-1061.

Spillantini, M. G. and M. Goedert (2000). "Tau mutations in familial frontotemporal dementia." Brain **123 (Pt 5)**: 857-859.

Stine, W. B., Jr., K. N. Dahlgren, G. A. Krafft and M. J. LaDu (2003). "In vitro characterization of conditions for amyloid-beta peptide oligomerization and fibrillogenesis." J Biol Chem **278**(13): 11612-11622.

Stoscheck, C. M. (1990). "Quantitation of protein." Methods Enzymol **182**: 50-68.

Sydow, A., A. Van der Jeugd, F. Zheng, T. Ahmed, D. Balschun, O. Petrova, D. Drexler, L. Zhou, G. Rune, E. Mandelkow, R. D'Hooge, C. Alzheimer and E. M. Mandelkow

(2011). "Tau-induced defects in synaptic plasticity, learning, and memory are reversible in transgenic mice after switching off the toxic Tau mutant." J Neurosci **31**(7): 2511-2525.

Teplow, D. B. (2006). "Preparation of amyloid beta-protein for structural and functional studies." Methods Enzymol **413**: 20-33.

Tepper, K., J. Biernat, S. Kumar, S. Wegmann, T. Timm, S. Hubschmann, L. Redecke, E. M. Mandelkow, D. J. Muller and E. Mandelkow (2014). "Oligomer formation of tau protein hyperphosphorylated in cells." J Biol Chem **289**(49): 34389-34407.

Terrill-Usery, S. E., B. A. Colvin, R. E. Davenport and M. R. Nichols (2016). "Abeta40 has a subtle effect on Abeta42 protofibril formation, but to a lesser degree than Abeta42 concentration, in Abeta42/Abeta40 mixtures." Arch Biochem Biophys **597**: 1-11.

Terrill-Usery, S. E., M. J. Mohan and M. R. Nichols (2014). "Amyloid-beta(1-42) protofibrils stimulate a quantum of secreted IL-1beta despite significant intracellular IL-1beta accumulation in microglia." Biochim Biophys Acta **1842**(11): 2276-2285.

Titford, M. (2010). "Rudolf Virchow: Cellular Pathologist." Laboratory Medicine **41**(5): 311.

Van der Jeugd, A., K. Hochgrafe, T. Ahmed, J. M. Decker, A. Sydow, A. Hofmann, D. Wu, L. Messing, D. Balschun, R. D'Hooge and E. M. Mandelkow (2012). "Cognitive defects are reversible in inducible mice expressing pro-aggregant full-length human Tau." Acta Neuropathol **123**(6): 787-805.

Vella, L. J., R. A. Sharples, V. A. Lawson, C. L. Masters, R. Cappai and A. F. Hill (2007). "Packaging of prions into exosomes is associated with a novel pathway of PrP processing." J Pathol **211**(5): 582-590.

von Bergen, M., P. Friedhoff, J. Biernat, J. Heberle, E. M. Mandelkow and E. Mandelkow (2000). "Assembly of tau protein into Alzheimer paired helical filaments depends on a local sequence motif ((306)VQIVYK(311)) forming beta structure." Proc Natl Acad Sci U S A **97**(10): 5129-5134.

Walsh, D. M., D. M. Hartley, Y. Kusumoto, Y. Fezoui, M. M. Condron, A. Lomakin, G. B. Benedek, D. J. Selkoe and D. B. Teplow (1999). "Amyloid β-protein fibrillogenesis. Structure and biological activity of protofibrillar intermediates." Journal of Biological Chemistry **274**(36): 25945-25952.

Walsh, D. M., A. Lomakin, G. B. Benedek, M. M. Condron and D. B. Teplow (1997). "Amyloid β-protein fibrillogenesis: Detection of a protofibrillar intermediate." Journal of Biological Chemistry **272**(35): 22364-22372.

Wang, J., N. Li, J. Ma, Z. Gu, L. Yu, X. Fu, X. Liu and J. Wang (2016). "Effects of an amyloid-beta 1-42 oligomers antibody screened from a phage display library in APP/PS1 transgenic mice." Brain research **1635**: 169-179.

Wang, J., S. W. Tse and A. Andreadis (2007). "Tau exon 6 is regulated by an intricate interplay of trans factors and cis elements, including multiple branch points." J Neurochem **100**(2): 437-445.

Wang, Y. and E. Mandelkow (2016). "Tau in physiology and pathology." Nat Rev Neurosci **17**(1): 5-21.

Weidemann, A., G. Konig, D. Bunke, P. Fischer, J. M. Salbaum, C. L. Masters and K. Beyreuther (1989). "Identification, biogenesis, and localization of precursors of Alzheimer's disease A4 amyloid protein." Cell **57**(1): 115-126.

Weingarten, M. D., A. H. Lockwood, S. Y. Hwo and M. W. Kirschner (1975). "A protein factor essential for microtubule assembly." Proc Natl Acad Sci U S A **72**(5): 1858-1862.

Weisenberg, R. C., G. G. Borisy and E. W. Taylor (1968). "The colchicine-binding protein of mammalian brain and its relation to microtubules." Biochemistry **7**(12): 4466-4479.

Wille, H., G. Drewes, J. Biernat, E. M. Mandelkow and E. Mandelkow (1992). "Alzheimer-like paired helical filaments and antiparallel dimers formed from microtubule-associated protein tau in vitro." The Journal of Cell Biology **118**(3): 573.

Wischik, C. M., M. Novak, P. C. Edwards, A. Klug, W. Tichelaar and R. A. Crowther (1988). "Structural characterization of the core of the paired helical filament of Alzheimer disease." Proc Natl Acad Sci U S A **85**(13): 4884-4888.

Wisniewski, K. E., H. M. Wisniewski and G. Y. Wen (1985). "Occurrence of neuropathological changes and dementia of Alzheimer's disease in Down's syndrome." Ann Neurol **17**(3): 278-282.

Wu, J. W., L. Breydo, J. M. Isas, J. Lee, Y. G. Kuznetsov, R. Langen and C. Glabe (2010). "Fibrillar oligomers nucleate the oligomerization of monomeric amyloid beta but do not seed fibril formation." J Biol Chem **285**(9): 6071-6079.

Wu, J. W., M. Herman, L. Liu, S. Simoes, C. M. Acker, H. Figueroa, J. I. Steinberg, M. Margittai, R. Kayed, C. Zurzolo, G. Di Paolo and K. E. Duff (2013). "Small misfolded Tau species are internalized via bulk endocytosis and anterogradely and retrogradely transported in neurons." J Biol Chem **288**(3): 1856-1870.

Wyatt, P. J. (1993). "Light scattering and the absolute characterization of macromolecules." Analytica Chimica Acta **272**(1): 1-40.

Yan, Y. and C. Wang (2007). "Aβ40 Protects Non-toxic Aβ42 Monomer from Aggregation." Journal of Molecular Biology **369**(4): 909-916.

Zhukareva, V., D. Mann, S. Pickering-Brown, K. Uryu, T. Shuck, K. Shah, M. Grossman, B. L. Miller, C. M. Hulette, S. C. Feinstein, J. Q. Trojanowski and V. M. Lee (2002). "Sporadic Pick's disease: a tauopathy characterized by a spectrum of pathological tau isoforms in gray and white matter." Ann Neurol **51**(6): 730-739.

Zlokovic, B. V. (2013). "Cerebrovascular effects of apolipoprotein E: implications for Alzheimer disease." JAMA Neurol **70**(4): 440-444.

Benjamin Alexander Colvin was born 5 May, 1982 to Grant Matthew Colvin, M.S., M.S.W, and Juanita Clementina Polito-Colvin, M.D. in Saint Louis, MO. At Saint Louis Priory High School, he achieved National Merit Scholar Honorable Mention, and a Bright Flight Scholarship. He attended University of Missouri – Columbia, where he joined the Beta Beta chapter of Delta Sigma Phi. He graduated in 2005 with a B.S. in Biology and a Minor in Chemistry. After completing his undergraduate degree, he was hired as a contract employee by GlaxoSmithKline – Saint Louis as a Quality Control Chemist. He was quickly hired full time and his responsibilities expanded from raw material and finished product testing to include method development and process improvement roles. Having developed a strong interest in Analytical Chemistry during his time with GSK, Ben decided to pursue a Chemistry graduate degree. After two semesters at UMSL fulfilling prerequisite coursework, Ben applied to and was accepted into the Chemistry Department as a full-time Ph.D. student. The Nichols Lab was an excellent fit for Ben's Biology background, and his industry experiences with Analytical Chemistry. His hobbies include darts, table-top gaming, and graphic design.